

# Novel Light Emitting Mechanisms Originating from Graphene Plasmons Near and Far from Equilibrium

Thesis by  
Laura Kim

In Partial Fulfillment of the Requirements for the  
Degree of  
Doctor of Philosophy

The logo for the California Institute of Technology, featuring the word "Caltech" in a bold, orange, sans-serif font.

CALIFORNIA INSTITUTE OF TECHNOLOGY  
Pasadena, California

2019  
Defended May 21, 2019

© 2019

Laura Kim

ORCID: 0000-0002-9745-3668

All rights reserved

*dedicated to my Lord and Savior Jesus Christ*

## ACKNOWLEDGEMENTS

First and foremost, I would like to thank my advisor, Professor Harry Atwater. I cannot thank him enough for his endless support and opportunities he has given me. His enthusiasm for science and compassion for his students inspire me each and every day. He has presented the right amount of freedom and challenges along my academic journey, and has shaped me into the researcher I am today. It has been an honor to be in his research group and part of his amazing team.

I would also like to thank Professors William Johnson, Keith Schwab, and Stevan Nadj-Perge for serving on my thesis committee. I truly appreciate their time and expertise. Next, I would like to thank all of the collaborators and co-authors of the work presented in this thesis: Professor Victor Brar, Dr. Seyoon Kim, Professor Min Seok Jang, Dr. Pankaj Jha, Dr. Michelle Sherrott, Dr. Kelly Mauser, Josue Lopez, and Professor Mansoo Choi. I was very fortunate to be part of the first generation of the 2D group at Caltech. I am especially thankful for Victor, who has been a helpful, caring mentor with endless ideas since day one of my graduate school tenure. He has taught me so much in many aspects of conducting research. Also, I am very grateful for an opportunity to work with Dr. Seyoon Kim. I have learned so much from his meticulousness, which makes him a trustworthy collaborator and extremely skillful researcher. I also want to thank my officemates: Dr. Kelly Mauser, Cora Went, and Areum Kim. It was such a pleasant experience to share an office with them. I will miss spending time with them and all of our late night conversations.

I want to thank my biggest supporter, my husband, Dennis Kim. Despite sleep deprivation, he never failed to treat me and Audrey with so much love. Despite all of his professional commitments, he never failed to put our family as a top priority. Building an academic career while raising a family was not an easy task. I grew so much respect for him as we walked through this journey together. My husband, defined by his resilience, ambition, work ethic, and loving heart, is truly one of a kind. Our little princess, Audrey, we love you to the moon and back.

Finally, I want to express my deepest gratitude for my family. I have been endlessly supported by my mom and dad in Korea. Their unconditional love and support kept me going even during the times of hardship and disappointment. I also want to thank my in-law family for the way they welcomed me into the family and treated me as their own daughter and sister. Lastly, I am so happy that I got to run experiments and do crossfit together with my big brother, who always seemed like a dinosaur to me, since his time at Caltech as a postdoctoral researcher.

## ABSTRACT

Graphene supports surface plasmons bound to an atomically thin layer of carbon, characterized by tunable propagation characteristics and distinctly strong spatial confinement of the electromagnetic energy. Such collective excitations in graphene enable the strong interactions of massless Dirac fermions with light. In this work, I explore fundamental properties and applications of graphene plasmons both near and far from equilibrium. I discuss the ability of graphene plasmons to interact with its local environment in various forms of mid-infrared, optically active excitations, demonstrated by tunable graphene plasmon dispersions and an emergence of a new mode via addition of a monoatomic dielectric layer. Furthermore, the viability of graphene for optics-based applications and large-scale integration is epitomized by the experimental demonstration of perfect tunable absorption in a large-area chemically grown graphene by using a noble-metal-graphene metasurfaces. Using these properties of graphene plasmons, electronically tunable thermal radiation is demonstrated. Finally, I present theoretical predictions and experimental validations of nonequilibrium graphene plasmon excitations via ultrafast optical excitation, originating from a previously unobserved decay channel: hot plasmons generated from optically excited carriers. These studies reveal novel infrared light emitting processes, both spontaneous and stimulated, and provide a platform for achieving ultrafast, ultrabright mid-infrared light sources.

## PUBLISHED CONTENT AND CONTRIBUTIONS

Laura Kim\*, Seyoon Kim\*, Pankaj K. Jha, Victor W. Brar, and Harry A. Atwater, "Mid-Infrared Radiative Emission from Bright Hot Plasmons in Graphene," *under review* (2019).

Contribution: conception of the project, data collection, data analysis, inversion and gain calculations, emissivity calculations, sample preparation, writing of the manuscript, and revision.

Seyoon Kim\*, Min S. Jang\*, Victor W. Brar\*, Kelly W. Mauser, Laura Kim, and Harry A. Atwater, "Electronically Tunable Perfect Absorption in Graphene," *Nano Letters* **18**, 971-979 (2019).

<https://doi.org/10.1021/acs.nanolett.7b04393>

Contribution: data analysis, manuscript drafting, and revision.

Victor W. Brar, Michelle C. Sherrott, Min S. Jang, Seyoon Kim, Laura Kim, Mansoo Choi, and Harry A. Atwater, "Electronic Modulation of Infrared Radiation in Graphene Plasmonic Resonators," *Nature Communications* **6**, 7032 (2015).

<https://doi.org/.1038/ncomms8032>

Contribution: data collection and analysis.

Min S. Jang\*, Victor W. Brar\*, Michelle C. Sherrott, Josue J. Lopez, Laura Kim, Seyoon Kim, Mansoo Choi, and Harry A. Atwater, "Tunable Large Resonant Absorption in a Mid-Infrared Graphene Salisbury Screen," *Physical Review B* **90**, 165409 (2014).

<https://doi.org/10.1103/PhysRevB.90.165409>

Contribution: data analysis.

Victor W. Brar\*, Min S. Jang\*, Michelle C. Sherrott, Josue, J. Lopez, Laura Kim, Mansoo Choi, and Harry A. Atwater, "Hybrid Surface-Phonon-Plasmon Polariton Modes in Graphene/Monolayer h-BN Heterostructures," *Nano Letters* **14**, 3876-3880 (2014).

<https://doi.org/10.1021/nl501096s>

Contribution: data analysis.

## TABLE OF CONTENTS

Acknowledgements . . . . .	iv
Abstract . . . . .	vi
Published Content and Contributions . . . . .	vii
Table of Contents . . . . .	viii
List of Illustrations . . . . .	ix
Chapter I: Introduction . . . . .	1
1.1 Graphene . . . . .	1
1.2 Graphene plasmons . . . . .	2
1.3 Scope of this thesis . . . . .	12
Chapter II: Active Control of Graphene Plasmons . . . . .	16
2.1 Tunable large absorption in graphene . . . . .	16
2.2 Perfect absorption in graphene . . . . .	22
2.3 Tunable graphene plasmon dispersion relation and emergence of hybrid surface-phonon-plasmon polariton modes . . . . .	27
2.4 Tunable Planckian Thermal Emission . . . . .	34
Chapter III: Non-equilibrium Graphene Plasmons and Gain . . . . .	47
3.1 Carrier dynamics in graphene upon ultrafast optical excitation . . . . .	47
3.2 Non-equilibrium plasmon dispersion relation calculations . . . . .	49
3.3 Graphene Fermi level and time dependence . . . . .	55
3.4 Collision loss dependence . . . . .	59
3.5 Effects of underlying substrate . . . . .	61
3.6 The ratio of stimulated to spontaneous plasmon emission rates . . . . .	64
Chapter IV: Observation of Graphene Plasmon-Coupled Non-Planckian Radiation . . . . .	71
4.1 Experimental Setup . . . . .	71
4.2 Mid-infrared emission phenomena under pulsed laser excitation . . . . .	76
4.3 Non-Planckian radiation contribution: plasmon emission . . . . .	84
4.4 Plasmon-coupled far-field radiation . . . . .	88
4.5 Roles of gold nanodisks . . . . .	94
4.6 Concluding Remark . . . . .	105
Chapter V: Conclusion . . . . .	108
5.1 Super-Planckian radiation . . . . .	108
5.2 Bright spontaneous emission sources . . . . .	109
5.3 Coherent graphene plasmon amplification . . . . .	111

## LIST OF ILLUSTRATIONS

<i>Number</i>	<i>Page</i>
1.1 (a) Schematic of monolayer graphene (b) Full electronic band structure of graphene (c) Linear electronic band structure expanded near Dirac points. . . . .	3
1.2 Wave localization (solid) and propagation length normalized by plasmon wavelength (dotted) for surface plasmons at silver-silicon interface. . . . .	7
1.3 Wave localization of graphene plasmons with varying graphene Fermi levels. . . . .	7
1.4 Normalized propagation length of graphene plasmons with varying graphene Fermi levels. . . . .	8
1.5 Schematic of a device configuration which allows transport measurement in graphene. The resistance between the source and the drain is measured as varying the gate voltage ( $V_G$ ) between the graphene and the back electrode. . . . .	11
1.6 Resistance changes of the graphene sheet measured with varying gate voltages. . . . .	11

- 2.1 (a) Schematic device structure of graphene Salisbury screen. The inset illustrates the device with the optical waves at the resonance condition. (b) dc resistance of graphene as a function of the gate voltage. The gate voltage at which graphene resistance is maximized corresponds to charge neutral point (CNP) of graphene. The inset is an AFM image of 40 nm nanoresonators. 18
- 2.2 (a) The total absorption in the device for undoped (red dashed) and hole doped (blue solid) 40 nm nanoresonators. (b) The change in absorption with respect to the absorption at the charge neutral point (CNP) in 40 nm graphene nanoresonators at various doping levels. The solid black curve represents the absorption difference of bare (unpatterned) graphene. (c) Width dependence of the absorption difference with the carrier concentration of  $1.42 \times 10^{13} \text{ cm}^{-2}$ . The resonator width varies from 20 to 60 nm. The dashed curve shows the theoretical intensity of the surface parallel electric field at the  $\text{SiN}_x$  surface when graphene is absent. . . . . 20

2.3	Schematic of (a-c) type A, B, and C structures, respectively. In parts a-c, panels at the back side present the out-of-plane electric field distributions, and $E_z$ distributions in graphene are overlapped on graphene plasmonic ribbons (GPRs). The images of GPRs in panels b and c are the virtual GPRs created by metallic strips, which operate as mirrors. (d-f) Corresponding scanning electron microscope (SEM) images (false color). The dark and bright regions correspond to GPRs and exposed $\text{SiO}_2$ areas, respectively. The GPRs have 150-nm-wide bridges to ensure electrical connections, and the length of the GPR strip is 3 $\mu\text{m}$ . . . . .	24
2.4	(a) Absorption in type 0, A, B, and C at $1356 \text{ cm}^{-1}$ as a function of graphene hole mobility ( $\mu_h$ ). (b) Tunable absorption in each structure as a function of graphene Fermi level ( $E_F$ ) for $\mu_h = 315 \text{ cm}^2 \text{ V}^{-1} \text{ s}^{-1}$ . . . . .	26
2.5	(a) Absorption and (b) modulation efficiency as a function of graphene Fermi level ( $E_F$ ) at the frequency for maximum absorption in each structure. . . . .	26

- 2.6 (a) Schematic of device measured and modeled in this work. Graphene nanoresonators are fabricated on a monolayer h-BN sheet on a SiO<sub>2</sub>(285 nm)/Si wafer. Gold contact pads are used to contact the graphene sheet, and the Si wafer is used to apply an in situ backgate voltage ( $V_G$ ). Zoom-in shows cartoon of graphene plasmon coupling to h-BN optical phonon. (b) Optical image of unpatterned area of device where both the graphene and h-BN monolayers have been mechanically removed. (c) Scanning electron microscope image of the 80 nm graphene nanoresonators (light regions). . . . . 29
- 2.7 (Left axis) Normalized transmission spectra of graphene nanoresonators with widths varying from 30 to 300 nm, as well as transmission through the unpatterned graphene/h-BN sheet. Spectra are measured at carrier densities of  $1.0 \times 10^{13} \text{ cm}^{-2}$  and normalized relative to zero carrier density. For 80 nm ribbons, the four different observable optical modes are labeled with the symbols used to indicate experimental data points in Fig. 2.8. (Right axis, bottom spectrum) Infrared transmission of the bare monolayer h-BN on SiO<sub>2</sub> normalized relative to transmission through the SiO<sub>2</sub>(285 nm)/Si wafer. The dotted vertical line indicates this peak position as a reference for the other spectra. . . . . 30

- 2.8 Calculated change in transmission for graphene/monolayer hBN/SiO<sub>2</sub> nanoresonators of varying width at a carrier density of  $1.0 \times 10^{13} \text{ cm}^{-2}$ , normalized relative to zero carrier density. Experimental data is plotted as symbols indicating optical modes assigned in Fig 2.7. The error bars represent uncertainty in the resonator width that is obtained from AFM measurements. For small k-vectors (large resonators), this uncertainty is smaller than the symbol size. The dashed line indicates the theoretical dispersion for bare graphene plasmons, while the dash-dot line indicates the dispersion for graphene/SiO<sub>2</sub>. The three horizontal dotted lines indicate the optical phonon energies of h-BN and SiO<sub>2</sub>. . . . . 32
- 2.9 Calculated transmission spectra for 80-nm-wide graphene resonator/top SiO<sub>2</sub>/80-nm-wide monolayer h-BN/bottom SiO<sub>2</sub> as the top SiO<sub>2</sub> layer thickness is varied from 0 to 80 nm in 10 nm increments. Spectra are for a carrier density of  $1.0 \times 10^{13} \text{ cm}^{-2}$  and normalized relative to zero carrier density. . . . . 33

- 2.10 (a) Schematic of the experimental apparatus. The  $70\ \mu\text{m} \times 70\ \mu\text{m}$  graphene nanoresonator arrays are placed on a  $1\text{-}\mu\text{m}$ -thick  $\text{SiN}_x$  membrane with a  $200\text{-nm}$ -thick gold backreflector. A gate bias is applied through the  $\text{SiN}_x$  membrane between the underlying Si frame and graphene sheet. The temperature-controlled stage contains a feedback controlled, heated silver block that holds a  $2\text{-mm}$ -thick copper sample carrier with a  $100\text{-}\mu\text{m}$ -thick sapphire layer used for electrical isolation. The temperature is monitored with a thermocouple in the block, and the stage is held at a vacuum of  $1\ \text{mtorr}$ . A  $1\text{-mm}$ -thick potassium bromide (KBr) window is used to pass thermal radiation out of the stage, which is collected with a Cassegrain objective and passed into an FTIR with an MCT detector. (b) A representative SEM image of  $30\text{-nm}$ -wide graphene nanoresonators on a  $1\text{-}\mu\text{m}$ -thick  $\text{SiN}_x$  membrane. (c) Source-drain resistance versus gate voltage curve of the device. The peak in the resistance occurs at the charge neutral point (CNP) of graphene. . . . . 35

2.11	(a) Carrier density dependence of change in emissivity with respect to the CNP for 40-nm-wide graphene nanoresonators at 250°C. (b) Width dependence of change in emissivity for 20-, 30-, 40-, 50-, 60-nm-wide nanoresonators at 250°C and for a carrier density of $1.2 \times 10^{13} \text{ cm}^{-2}$ . The black line indicates the emissivity changes of bare, unpatterned graphene at the same carrier density and temperature. (c) Polarization dependence of the emissivity change for 40 nm graphene nanoresonators at 250 °C for a carrier density of $1.2 \times 10^{13} \text{ cm}^{-2}$ . . . . .	39
2.12	Temporal waveform of applied voltage signal (black line) and detector signal of emission from 50 nm ribbons at 250°C (green line). . . . .	41
3.1	Carrier relaxation processes in graphene under ultrafast optical excitation: (i) Sharply peaked distribution of photoexcited carriers upon optical pumping. (ii) Carriers with a non-Fermi-like distribution undergoing carrier-carrier scattering on a 10-fs time scale. (iii) Carriers in a quasi-equilibrium state. (iv) Carriers that have been thermalized under interband processes, but are still hotter than the lattice. (v) Complete equilibrium between the carriers and the lattice. . . . .	48
3.2	Gate-dependent temperature profiles of graphene for a given laser fluence of $1.12 \text{ J m}^{-2}$ . . . . .	55

3.3	Non-equilibrium plasmon dispersions for graphene on top of SiN <sub>x</sub> for a given laser fluence of 1.12 J m <sup>-2</sup> (the pulse width was assumed to be 100 fs). (a) The real part and (b) imaginary part of plasmon complex frequency dispersion for different gate-controlled initial graphene Fermi levels at time when the quasi-equilibrium has just been established. . . . .	57
3.4	Non-equilibrium plasmon dispersions for graphene on top of SiN <sub>x</sub> . (a) The real part and (b) imaginary part of plasmon complex frequency for a given initial graphene Fermi level of 0.34 eV as time progresses since the quasi-equilibrium has established. The laser fluence of 1.12 J m <sup>-2</sup> , and the pulse width of 100 fs are assumed. . . . .	58
3.5	The effects of collision loss time, $\tau$ . (a) The real and (b) imaginary part of plasmon dispersion relation at the time the system has reached a quasi-equilibrium for a given gate-controlled graphene Fermi level of 0.34 eV. The laser fluence of 1.12 J m <sup>-2</sup> and the pulse width of 100 fs were assumed. . . . .	60
3.6	Plasmon emission spectra with varying collision time, $\tau$ , calculated based on the solved graphene plasmon relations shown in Fig. 3.5. The gate-controlled graphene Fermi level was fixed at 0.34 eV. . . . .	61
3.7	Real and imaginary parts of the relative permittivity of SiN <sub>x</sub> . . .	62

3.8	(a) Gate-dependent plasmon dispersion relation defined on a complex-k plane for a given carrier temperature of 2,000 K and collision loss time of $\tau = 50$ fs. (b) Plasmon loss quantified by the ratio of imaginary and real parts of graphene plasmon wavevector, $k_{GP}$ . . . . .	63
3.9	Three fundamental processes that contribute to the total number of plasmons in the system: spontaneous emission, stimulated emission, and absorption of plasmons. A and B are the spontaneous emission and stimulated emission/absorption Einstein coefficients, respectively. $N_p$ is the plasmon density, and $N_e$ and $N_g$ are the carrier densities in the excited and ground states, respectively. $\gamma_{coll}$ is the collision rate. . . . .	66
3.10	(a) The ratio of stimulated to spontaneous plasmon emission rates as a function of time at $\lambda = 6 \mu\text{m}$ for a given initial graphene Fermi level of 0.34 eV. The laser fluence of $1.12 \text{ J m}^{-2}$ and the pulse width of 100 fs are assumed. $t_0$ represents the time at which the system has just reached quasi-equilibrium. (b) The time-averaged ratio for a given initial graphene Fermi level of 0.34 eV and $\gamma_{coll}^{-1} = 20$ fs as a function of wavelength when the ratio is integrated up to $t - t_0 = 250$ fs, 500 fs, 1 ps, 2 ps, and 3 ps. . . . .	67
4.1	Far-field infrared emission measurement setup. . . . .	72
4.2	Graphene-Fermi-level-dependent absorptivity (emissivity) of the graphene/SiN <sub>x</sub> /ITO device. (a) measured and (b) calculated. . . . .	75

4.3	Graphene-Fermi-level-dependent absorptivity (emissivity) contribution from each layer at ambient temperature. . . . .	75
4.4	Graphene-Fermi-level-dependent emission in a planar graphene under pulsed laser excitation with a constant fluence of $1.12 \text{ J m}^{-2}$ (solid color lines), compared with measured thermal emission spectrum at $95 \text{ }^\circ\text{C}$ (dotted black line). . . . .	76
4.5	Planckian thermal emission under isothermal (solid color lines) and varying temperature (dotted color lines) conditions. . . . .	79
4.6	Measured emission spectra from ITO-SiN <sub>x</sub> -ITO for various gate voltages under pulsed laser excitation with a constant laser fluence of $1.12 \text{ J m}^{-2}$ . . . . .	81
4.7	Measured gate voltage-dependent emission spectra under continuous wave (CW) laser excitation with a constant fluence of $1.12 \text{ J m}^{-2}$ (solid color lines), compared with measured thermal emission spectrum at $95 \text{ }^\circ\text{C}$ (dotted black line). . . . .	83
4.8	For a fixed laser fluence of $1.12 \text{ J m}^{-2}$ , plasmon decay rates for different gate-controlled graphene Fermi levels at $t_0$ , the time at which carriers have just thermalized and the carrier temperature is at its maximum. $\gamma_p > 0$ denotes net plasmon generation, and $\gamma_p < 0$ denotes net plasmon loss. . . . .	85
4.9	For a given gate-controlled graphene Fermi level of $0.34 \text{ eV}$ and laser fluence of $1.12 \text{ J m}^{-2}$ , the temporal evolution of the plasmon decay rates. Time denoted in the legend indicates the time that has passed since $t_0$ . . . . .	85

4.10	Time-integrated spontaneous plasmon emission spectra for different gate-controlled graphene Fermi levels under a laser fluence of $1.12 \text{ J m}^{-2}$ . . . . .	87
4.11	Time-integrated spontaneous plasmon emission spectra for a given gate-controlled graphene Fermi level of 0.34 eV under different laser fluences. . . . .	87
4.12	(a) AFM measurement of a $\text{SiN}_x$ surface, showing root mean square roughness of 0.4 nm. (b) Schematic for calculating radiation efficiencies of graphene plasmons propagating on a planar graphene surface which conforms to the roughness of the underlying $\text{SiN}_x$ . (c) Experimentally determined out-coupling efficiencies. (d) Calculated radiation efficiencies. . . . .	90
4.13	Gate-dependent measured emission spectra (solid color lines) under pulsed laser excitation compared with the out-coupled, calculated spontaneous plasmon emission spectra (dotted color lines). In both cases, the relevant laser fluence is $1.12 \text{ J m}^{-2}$ . . . . .	92
4.14	Laser-fluence-dependent measured emission spectra under pulsed laser excitation (solid color lines), compared with the calculated, out-coupled spontaneous plasmon emission spectra (dotted color lines). In both cases, the relevant gate-controlled graphene Fermi level is 0.34 eV. . . . .	93

4.15	Electric intensity distribution under the planar wave excitation at the laser wavelength of 850 nm. Side view electric intensity distributions of Graphene/SiN <sub>x</sub> /ITO structure with the (a) resonant and (b) non-resonant NDs. Top view electric intensity distributions for the (c) resonant and (d) non-resonant NDs. . . . .	95
4.16	Optical cross-sections of the resonant and non-resonant NDs.	96
4.17	Gate-dependent measured absorptivity (or emissivity) of the graphene/SiN <sub>x</sub> /ITO structure with and without NDs at ambient temperature. (a) Planar graphene. (b) Non-resonant NDs on graphene. (c) Resonant NDs on graphene. (d) For a fixed graphene Fermi level at 0.34 eV, the measured emissivities with and without the NDs. . . . .	97
4.18	(a) Total absorptions of the graphene/SiN <sub>x</sub> /ITO device with and without the NDs. (b) Absorptions in graphene with and without the NDs. . . . .	97
4.19	Expected gate-dependent thermal emission spectra under isothermal conditions of given temperatures of 70 °C, 115 °C, and 150 °C. The spectra were calculated by multiplying the measured gate-dependent absorptivity of the device by Planck's spectrum of a corresponding temperature. . . . .	99
4.20	Gate-dependent emission spectra from planar and ND-decorated graphene samples under CW laser excitation with a laser fluence of 0.75 J m <sup>-2</sup> (color solid lines). Measured thermal emission spectra from the device for given temperatures of 70 °C, 95 °C, and 100 °C (black dotted lines). . . . .	99

- 4.21 Gate-dependent emission spectra from planar and ND-decorated graphene samples under pulsed laser excitation with a constant laser fluence of  $0.75 \text{ J m}^{-2}$  (color solid lines). In the resonant ND data, the dotted lines for 0.24 eV and 0.34 eV correspond to the original measurements, and the solid lines are fitted to compensate the offset, which appeared due to experimental imperfections. Measured thermal emission spectra from the device for given temperatures of 70 °C, 115 °C, and 150 °C (black dotted lines). . . . . 101
- 4.22 Emission contributions that deviate from the corresponding thermal emission background under pulsed laser excitation with a constant laser fluence of  $0.75 \text{ J m}^{-2}$  from planar graphene and ND-decorated graphene samples at a given gate-controlled graphene Fermi level of 0.34 eV. . . . . 102
- 4.23 Field enhancement factor around the NDs due to the plasmonic resonance. . . . . 102

4.24	Calculated radiation efficiency of graphene plasmons with and without NDs with varying distance from the edge of a ND. The dotted lines represent the plasmon radiation efficiencies without considering the field. The solid lines represent the plasmon radiation efficiencies considering the effects of the near-field enhancement due to the plasmonic resonance of NDs. The yellow dotted line represents the radiation efficiency of a single graphene plasmon launched on a planar graphene surface. All calculations were performed at the wavelength of 6 $\mu\text{m}$ , and the graphene Fermi level was assumed to be 0.34 eV. . . . .	104
5.1	Spectral flux of cumulative spontaneous plasmon emission from planar graphene at various laser fluences for a given graphene Fermi level of 0.34 eV compared with the spectral flux of black-body radiation at 500 K, 1,000 K, and 2,000 K, assuming unity out-coupling efficiency of plasmons. . . . .	110

*Chapter 1*

## INTRODUCTION

**1.1 Graphene**

Graphene is a two-dimensional material consisting of carbon atoms in a honeycomb lattice as shown in Fig. 1.1(a). Since its discovery [14], it has attracted significant attention from the scientific community due to its extraordinary electronic, mechanical, and thermal properties [1, 2, 7]. Many of the studied properties arise from its electronic structure, which shows the relativistic nature of charge carriers in graphene. The electronic properties of graphene combined with its monoatomic thickness makes graphene an exceptional plasmonic material. The collective excitations of the 2D electron gas bound to an atomically thin layer of carbon exhibit extreme spatial confinement, low loss, and large tunability [4, 9, 12, 16, 18]. In this chapter, we introduce basic concepts of the electronic, optical, and plasmonic properties of graphene, which serve as background for the detailed discussions in the following chapters.

**Linear Electronic Dispersion**

As shown in Fig. 1.1(a), the carbon atoms in a hexagonal lattice of graphene are covalently bonded through the in-plane  $\sigma$  bonds formed by the hybridized  $sp^2$  orbitals. The remaining electron in a carbon atom occupies the  $p_z$  orbital that is perpendicular to graphene sheet, forming a half-filled  $\pi$  band. The  $\pi$  band is responsible for the low-energy electronic band structure, which gives rise to many of the interesting physical phenomena. The lattice structure of

graphene can be explained with a basis of two carbon atoms per primitive unit cell with the two lattice vectors:  $\mathbf{a}_1 = \frac{a}{2}(3, \sqrt{3})$  and  $\mathbf{a}_2 = \frac{a}{2}(3, -\sqrt{3})$ , where  $a$  is the carbon-carbon distance given by 1.42 Å. Using the tight binding model, the electronic band structure near Dirac points ( $\mathbf{K}$  and  $\mathbf{K}'$ ) is given by Eq. 1.1 [16, 21]. Here we neglect electrons hopping to next nearest neighbors.

$$E_{\pm}(\mathbf{k}) = \pm t \sqrt{3 + 2\cos(\sqrt{3}k_y a) + 4\cos\left(\frac{\sqrt{3}}{2}k_y a\right)\cos\left(\frac{3}{2}k_x a\right)} \quad (1.1)$$

where  $t$  is a nearest neighbor hopping energy ( $\sim 2.8$  eV), and  $a$  is the carbon-carbon distance. Eq. 1.1 reveals that the electronic dispersion is symmetric around zero energy, displaying particle-hole symmetry. When the full electronic band structure is expanded near a Dirac point ( $\mathbf{K}$  or  $\mathbf{K}'$ ) with respect to the relative momentum vector,  $\mathbf{q} = \mathbf{k} - \mathbf{K}$ , with  $|\mathbf{q}| \ll |\mathbf{K}|$ , a linear dispersion is obtained given by Eq. 1.2 (also shown in Fig. 1.1(c)).

$$E_{\pm}(\mathbf{q}) \approx \hbar v_F |\mathbf{q}| \quad (1.2)$$

where  $v_F$  is the Fermi velocity in graphene ( $\approx 1 \times 10^6$  m/s). This linear dispersion has an important implication. The low-energy excitations in graphene are massless, chiral Dirac fermions, which exhibit many of the unusual properties of quantum electrodynamics (QED), but with an approximately 300 times smaller speed [10, 11, 16].

## 1.2 Graphene plasmons

Plasmonics has become a key ingredient towards realization of nanophotonics due to the ability of surface plasmons to confine and control light at scales

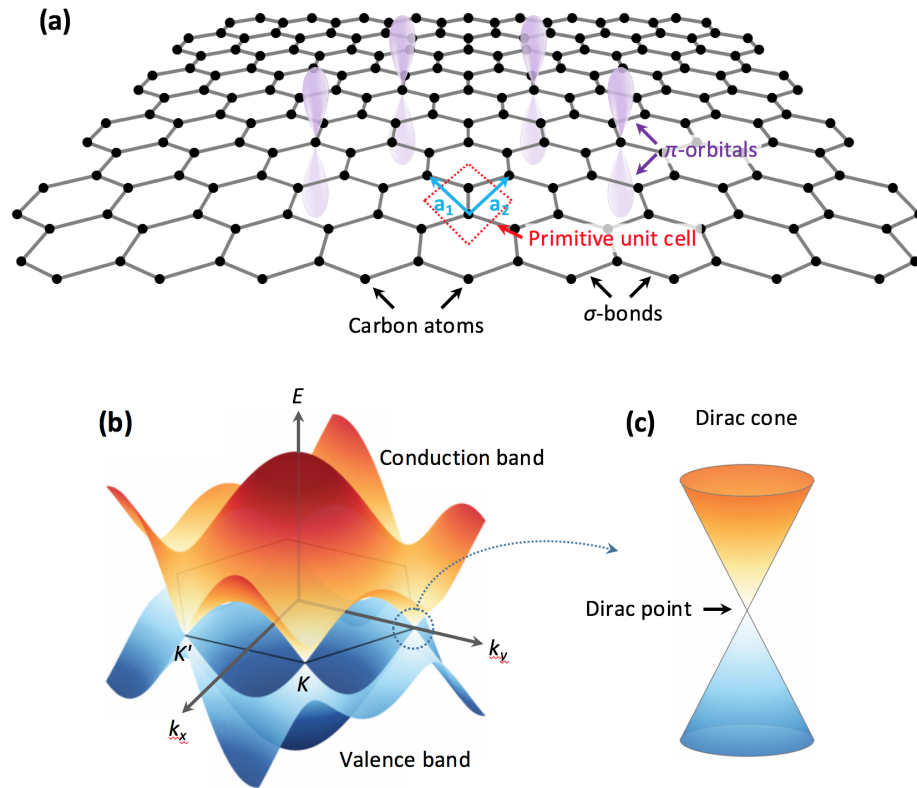


Figure 1.1: (a) Schematic of monolayer graphene (b) Full electronic band structure of graphene (c) Linear electronic band structure expanded near Dirac points.

substantially smaller than the free space wavelength. Graphene has shown to be an exceptional plasmonic material, as its atomic thinness enables low losses and significantly large wave confinement of plasmons compared to those exhibited in noble metals [9].

### Dispersion relation

Graphene plasmon dispersion relation can be obtained by solving the Maxwell's equations with the boundary conditions given by Eq. 1.3 and Eq. 1.4. The boundary conditions display a discontinuity in the magnetic field due to a sheet

current,  $\sigma E_z$ , flowing in the graphene sheet.

$$E_z(x \rightarrow 0^+) = E_z(x \rightarrow 0^-) \quad (1.3)$$

$$H_y(x \rightarrow 0^+) - H_y(x \rightarrow 0^-) = \sigma E_z(x = 0) \quad (1.4)$$

We consider TM modes of graphene plasmons propagating along graphene surface at  $x = 0$ . The plasmon dispersion relation for graphene,  $k_p(\omega)$ , sandwiched between two dielectric layers with relative permittivities of  $\epsilon_1$  and  $\epsilon_2$  can be written as Eq. 1.5.

$$\frac{\epsilon_1}{\sqrt{k_p^2 - \epsilon_1(\omega^2/c^2)}} + \frac{\epsilon_2}{\sqrt{k_p^2 - \epsilon_2(\omega^2/c^2)}} = -j \frac{\sigma}{\omega \epsilon_0} \quad (1.5)$$

In a quasi-static regime ( $k_p \gg \omega/c$ ), the dispersion relation can be further approximated as Eq. 1.6.

$$k_p \approx \frac{j\omega\epsilon_0(\epsilon_1 + \epsilon_2)}{\sigma} \quad (1.6)$$

To model the sheet conductivity of graphene, a semi-classical Drude-like expression is adopted [5, 6]. In the local limit of random phase approximation (i.e., in-plane, parallel wavevector  $k_{\parallel} \rightarrow 0$ ), the frequency-dependent surface conductivity of graphene,  $\sigma(\omega)$ , can be represented as a sum of intraband and interband contributions of particle-hole excitations as given by Eq. 1.7.

$$\begin{aligned} \sigma(\omega) &= \sigma_{\text{intra}}(\omega) + \sigma_{\text{inter}}(\omega) \\ &= \frac{e^2\omega}{i\pi} \left[ \int_{-\infty}^{\infty} dE \frac{|E|}{(\hbar\omega)^2} \cdot \frac{df_d(E)}{dE} - \int_0^{\infty} dE \frac{f_d(-E) - f_d(E)}{(\hbar\omega)^2 - 4E^2} \right] \end{aligned} \quad (1.7)$$

where  $f_d(E) = \frac{1}{1+\exp\left(\frac{E-\mu}{k_B T}\right)}$  is the Fermi-Dirac distribution function. Considering scattering losses, we can make the following transformation to the frequency:  $\omega \rightarrow \omega + i\tau^{-1}$ , where  $\tau$  is the scattering loss time. At low frequencies, losses are dominated by electron-impurity scattering process, and the relevant relaxation time can be expressed as  $\tau_{\text{impurity}} = \frac{\xi E_F}{e v_F^2}$ , where  $\xi$  is the carrier mobility,  $E_F$  is the Fermi energy, and  $v_F$  is the Fermi velocity. For  $\omega$  above the optical phonon energy ( $\sim 0.2\text{eV}$ ), electron-phonon scattering becomes a significant loss channel.  $\sigma_{\text{inter}}$  and  $\sigma_{\text{intra}}$  can be simplified to Eq. 1.8 and Eq. 1.9, respectively.

$$\sigma_{\text{inter}} = \sigma_0 G\left(\frac{\hbar\omega}{2}\right) + \frac{4i\hbar\omega\sigma_0}{\pi} \int_0^\infty dE \frac{G(E) - G\left(\frac{\hbar\omega}{2}\right)}{(\hbar\omega)^2 - (2E)^2} \quad (1.8)$$

where  $G(E) = \frac{\sinh\left(\frac{E}{k_B T}\right)}{\cosh\left(\frac{E}{k_B T}\right) + \cosh\left(\frac{\mu}{k_B T}\right)}$ , and  $\sigma_0 = e^2/(4\hbar)$  is the universal conductivity.

$$\sigma_{\text{intra}} = \frac{i}{\pi} \frac{D}{\omega + i\tau^{-1}} \quad (1.9)$$

where  $D = \frac{8\sigma_0 k_B T}{\hbar} \ln\left[2\cosh\left(\frac{\mu}{2k_B T}\right)\right]$  is the Drude weight, which is a function of chemical potential,  $\mu$ , and carrier temperature,  $T$ . Eq. 1.6 implies  $k_p \propto \omega/\sigma$ . For sufficiently high doping (when the sheet conductivity is dominated by the intraband contribution), graphene plasmon dispersion shows a quadratic dependence of  $k_p$  on  $\omega$  (i.e.,  $k_p \propto \omega^2$ ), which is characteristic of 2D electron gases [19]. This contrasts with low-energy surface plasmon polariton (SPP) dispersion on bulk metals ( $\omega \propto k_p$ ).

Graphene plasmons are characterized by large wave confinement and low loss. Surface plasmons for graphene on a silicon substrate are compared with the

surface plasmon excitations arising at the interface of a bulk silver and silicon. The SPP dispersion at a bulk silver-silicon interface was solved using  $\omega = ck_p \sqrt{\frac{\epsilon_m + \epsilon_d}{\epsilon_m \epsilon_d}}$ , where  $\epsilon_m$  and  $\epsilon_d$  are the relative permittivities of silver and silicon, respectively [15, 17]. The wave confinement of associated surface plasmons (SPs) is quantified as  $k_p/k_0$ , and the normalized propagation length, which represents how many SP wavelengths can travel before it loses most of its energy, is quantified as  $L_p/\lambda_p$ , where  $L_p$  is given by  $1/2\text{Im}(k_p)$ . The wave confinement and propagation length associated with the bulk silver-silicon SPPs are shown in Fig. 1.2. The corresponding wave confinement and propagation length of graphene plasmons are calculated assuming graphene carrier mobility of  $10^4 \text{ cm}^2 \text{ V}^{-1} \text{ s}^{-1}$  and temperature of 300K, and the results are shown in Fig. 1.3 and 1.4, respectively. Graphene plasmons exhibit significantly higher wave confinement and lower loss than surface plasmons excited at the surface of noble metals. In addition, the calculations suggest that graphene plasmons are highly tunable with graphene Fermi levels. Unlike bulk metals, graphene Fermi levels (or carrier density) can be easily varied via electrostatic gating, much like in field effect transistors (FET). Due to its two-dimensionality and linear electronic band structure, there exists a unique way to modulate graphene plasmons as discussed in the next section.

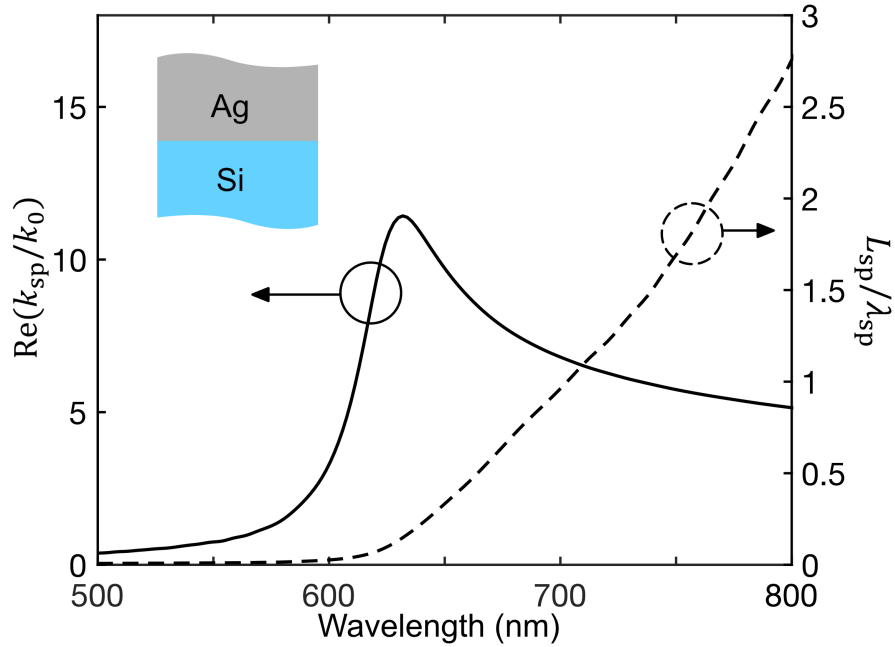


Figure 1.2: Wave localization (solid) and propagation length normalized by plasmon wavelength (dotted) for surface plasmons at silver-silicon interface.

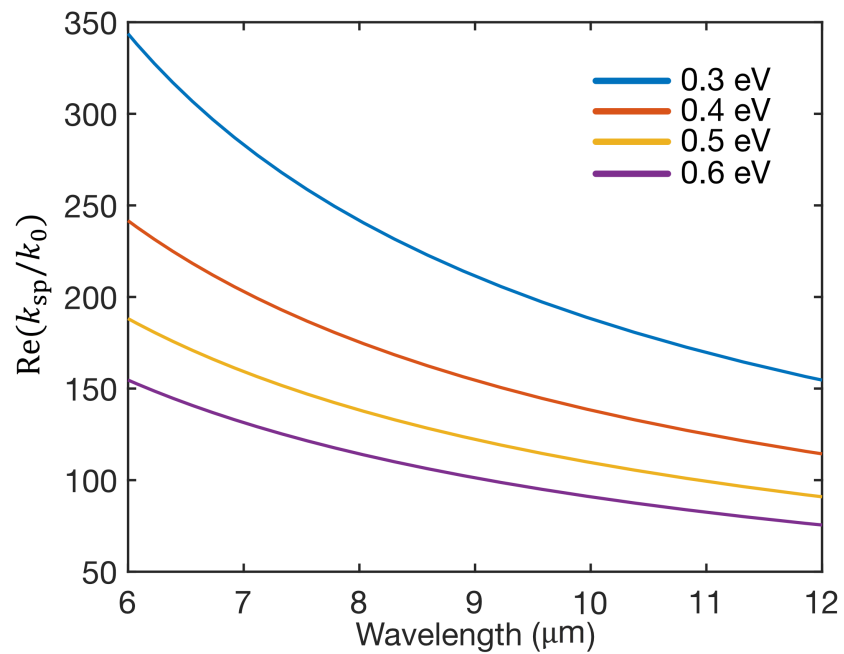


Figure 1.3: Wave localization of graphene plasmons with varying graphene Fermi levels.

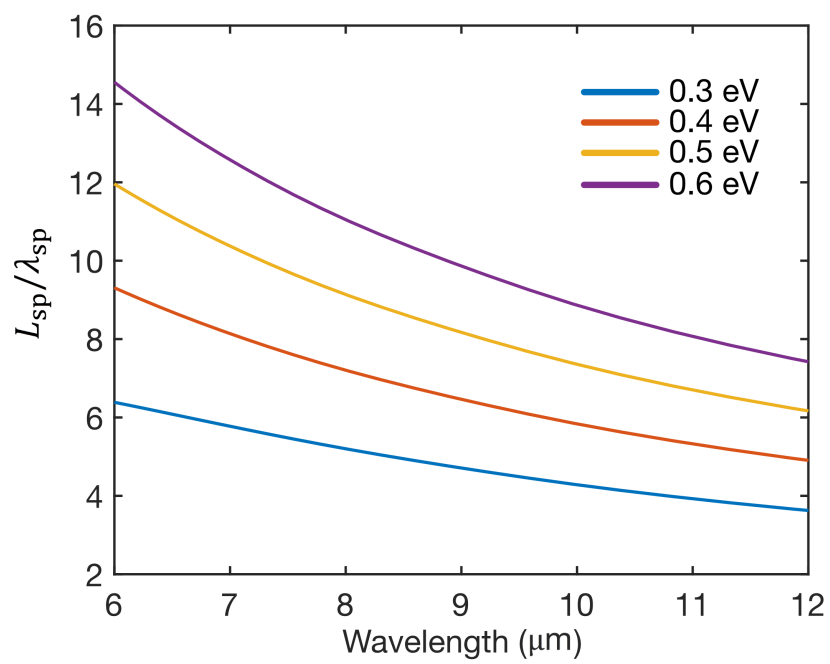


Figure 1.4: Normalized propagation length of graphene plasmons with varying graphene Fermi levels.

## Drude Weight

As suggested by Eq. 1.9, the plasmonic responses of graphene are dominated by the intraband Drude weight [20]. Drude weight quantifies the oscillator strength of free carrier absorption. Here, a general form of Drude weight is derived assuming general quasiparticle dispersion,  $E = A|k|^\alpha$ , and the density of states,  $\text{DOS}(E) = N \int \frac{d^d k}{(2\pi)^d} \delta(E - E(k)) = \gamma E^{\frac{d}{\alpha}-1}$ , where  $N$  is the degeneracy and  $d$  is the dimension of the system [8].

$$D = \frac{\alpha^2 A^{2/\alpha}}{\hbar^2} \frac{e^2 \pi}{d} \left(1 + \frac{d-2}{\alpha}\right) \int dE f_d(E) (\gamma E^{(d-2)/\alpha}) \quad (1.10)$$

where  $f_d(E)$  is the Fermi-Dirac distribution function. For a bulk material ( $d = 3$ ) with a parabolic dispersion ( $\alpha = 2$ ), the integrand of Eq. 1.10 becomes  $f_d(E)$  times the density of states, resulting in a temperature-independent Drude weight (i.e.,  $D_{\text{bulk, parabolic}} = D(n)$ ). In case of graphene ( $d = 2$  and  $\alpha = 1$ ), we obtain the Drude weight that is a function of both chemical potential and temperature as shown in Eq. 1.11.

$$D_{\text{graphene}} = \frac{8\sigma_0 k_B T}{\hbar} \ln \left[ 2 \cosh \left( \frac{\mu}{2k_B T} \right) \right] \quad (1.11)$$

In the zero-temperature limit, Eq. 1.11 reduces to  $D_{\text{graphene}} = \left(\frac{e^2}{\hbar^2}\right) \mu \propto \sqrt{|n|}$ , where  $n$  is the carrier density of graphene. This leads to  $\omega_p \propto n^{1/4}$  for a sufficiently doped graphene device operating at a moderate temperature.

Due to the atomic thinness, graphene carrier density (thus its plasmon dispersions) can be easily varied via electrostatic gating [3], and Fig. 1.5 shows a typical device configuration, which allows us to vary carrier densities in graphene

via applying gate voltages and monitor changes in resistance of the graphene sheet. The resistance between the source and the drain is measured as varying the gate voltage ( $V_G$ ) between the graphene and the back electrode as shown in Fig. 1.6. By sweeping gate voltages, graphene can change its characteristics from gapless semiconducting to metallic as graphene carrier densities are modulated. The resistance is maximized at the charge neutral point (CNP), at which the graphene Fermi level is positioned at the Dirac point. Typically, the CNP is not located at zero gate due to background doping from impurities in graphene as well as the substrate. In most of the cases, such impurities mentioned above induce hole doping in graphene.

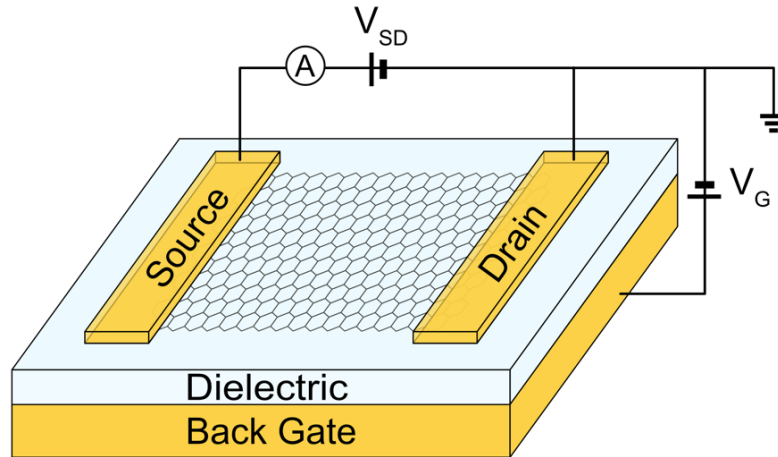


Figure 1.5: Schematic of a device configuration which allows transport measurement in graphene. The resistance between the source and the drain is measured as varying the gate voltage ( $V_G$ ) between the graphene and the back electrode.

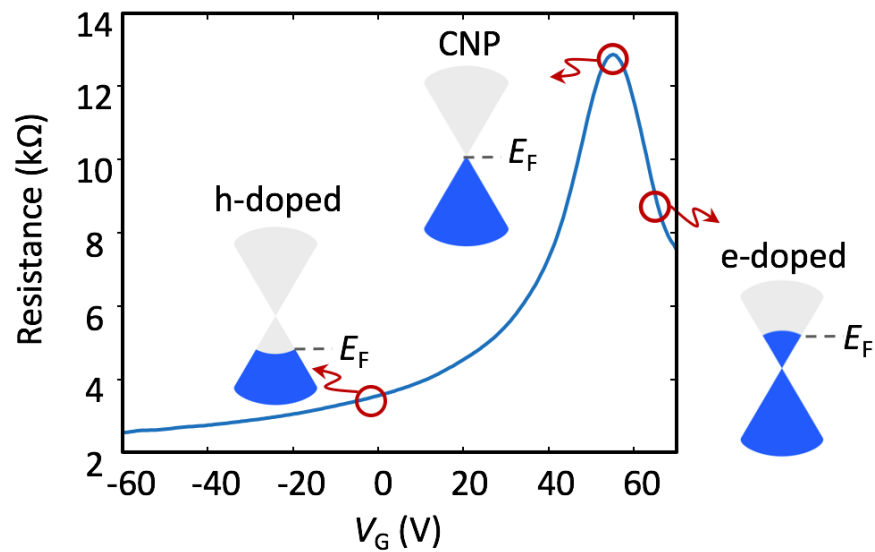


Figure 1.6: Resistance changes of the graphene sheet measured with varying gate voltages.

In the high electron temperature limit (i.e.,  $k_B T \ll \mu$ ),  $D$  asymptotes to a linearly increasing function of electron temperature (i.e.,  $D \rightarrow \frac{8\sigma_0 \ln(2)}{\hbar} k_B T \propto T$ ). In this regime, an increase in electron temperature enhances plasmonic responses of graphene. As discussed above, this is distinct from a Drude weight of a bulk material with a parabolic dispersion, which is independent of carrier temperature. Ultrafast optical excitation can induce temperatures of electrons that are much hotter than that of lattice, and it allows access to this regime [13, 20]. The high-temperature regime leads to  $\omega_{SP} \propto T_{\text{electron}}^{1/2}$ . The sensitivity of the Drude weight to electron temperature enables ultrafast optical control of plasmons in graphene at femtosecond time scales. Wagner et al. (2014) have shown that optical-pump-induced plasmon excitations resemble plasmonic responses originating from electrostatic gating [20]. Furthermore, Ni et al. (2016) have observed an emergence of plasmon excitations in a graphene sample, which displays no plasmonic responses under equilibrium condition, upon ultrafast optical excitation [13]. The observed phenomenon was explained with an increase in the Drude weight and was consistent with the solved dispersion relation of graphene plasmons at an elevated electron temperature [13].

### 1.3 Scope of this thesis

In this thesis, we explore fundamental properties and applications of graphene plasmons and light interactions both near and far from equilibrium. In Chapter 2, we discuss our work on understanding the characteristics of the confined plasmonics modes of graphene nanoresonators near equilibrium. We present examples of graphene plasmons serving as a sensitive local probe by coupling to various optically active excitations in the mid-infrared spectrum. The high

confinement of graphene plasmons allows them to strongly couple to optical phonons in an atomically thin layer, such as hexagonal boron nitride. The confined plasmonic modes in graphene can also strongly interact with thermally induced motions of quasiparticles and act as antennae to couple out local thermal energy, demonstrated by electronically tunable thermal radiation. Engineering device architectures consisting of graphene plasmonic resonators coupled with an external cavity and metallic plasmonic structures allows us to achieve perfect absorption in a monoatomic graphene sheet. Graphene-light interactions are no longer limited by the carrier mobility of graphene, making a significant progress in realizing scalable graphene plasmonic devices. In Chapters 3 and 4, we present theoretical prediction and experimental demonstration of ultrafast optical excitation of bright mid-infrared plasmonic excitation. We observe Fermi-level-dependent mid-infrared emission in graphene originating from a previously unobserved decay channel: hot plasmons generated from optically excited carriers. Under our experimental conditions, plasmon gain exists on the sub-100fs time scale during which stimulated plasmon emission dominates spontaneous plasmon emission. These observations set a framework for achieving ultrafast and ultrabright mid-infrared light sources and suggest an intriguing future possibility of achieving coherent graphene plasmon amplification. Finally, in Chapter 5, we present future opportunities for graphene plasmons as novel infrared light sources.

## References

- [1] Alexander A. Balandin et al. "Superior thermal conductivity of single-layer graphene". In: *Nano Lett.* 8.3 (2008), pp. 902–907. DOI: 10.1021/nl10731872. arXiv: 0802.1367v1.
- [2] K. I. Bolotin et al. "Ultrahigh electron mobility in suspended graphene". In: *Solid State Commun.* 146.9-10 (2008), pp. 351–355. DOI: 10.1016/j.ssc.2008.02.024.
- [3] Victor W. Brar et al. "Highly Confined Tunable Mid-Infrared Plasmonics in Graphene Nanoresonators". In: *Nano Letters* 13.6 (2013). PMID: 23621616, pp. 2541–2547. DOI: 10.1021/nl400601c. eprint: <https://doi.org/10.1021/nl400601c>.
- [4] Jianing Chen et al. "Optical nano-imaging of gate-tunable graphene plasmons". In: *Nature* 487.7405 (2012), p. 77.
- [5] L A Falkovsky. "Optical properties of graphene". In: *J. Phys. Conf. Ser.* 129.3 (Oct. 2008), p. 012004. DOI: 10.1088/1742-6596/129/1/012004.
- [6] L. A. Falkovsky and A. A. Varlamov. "Space-time dispersion of graphene conductivity". In: *Eur. Phys. J. B* 56.4 (2007), pp. 281–284. DOI: 10.1140/epjb/e2007-00142-3.
- [7] I. W. Frank et al. "Mechanical properties of suspended graphene sheets". In: *J. Vac. Sci. Technol. B Microelectron. Nanom. Struct.* 25.6 (2007), p. 2558. DOI: 10.1116/1.2789446.
- [8] A. J. Frenzel et al. "Semiconducting-to-metallic photoconductivity crossover and temperature-dependent drude weight in graphene". In: *Phys. Rev. Lett.* 113.5 (2014), pp. 1–6. DOI: 10.1103/PhysRevLett.113.056602.
- [9] Marinko Jablan, Hrvoje Buljan, and Marin Soljačić. "Plasmonics in graphene at infrared frequencies". In: *Phys. Rev. B - Condens. Matter Mater. Phys.* 80.24 (2009), pp. 1–7. DOI: 10.1103/PhysRevB.80.245435.
- [10] M. I. Katsnelson and K. S. Novoselov. "Graphene: New bridge between condensed matter physics and quantum electrodynamics". In: *Solid State Commun.* 143.1-2 (2007), pp. 3–13. DOI: 10.1016/j.ssc.2007.02.043.
- [11] M. I. Katsnelson, K. S. Novoselov, and A. K. Geim. "Chiral tunnelling and the Klein paradox in graphene". In: *Nat. Phys.* 2.9 (Sept. 2006), pp. 620–625. DOI: 10.1038/nphys384. arXiv: 0604323 [cond-mat].
- [12] Frank HL Koppens, Darrick E Chang, and F Javier Garcia de Abajo. "Graphene plasmonics: a platform for strong light-matter interactions". In: *Nano letters* 11.8 (2011), pp. 3370–3377.

- [13] G. X. Ni et al. "Ultrafast optical switching of infrared plasmon polaritons in high-mobility graphene". In: *Nat. Photonics* 10.4 (2016), pp. 244–247. DOI: 10.1038/nphoton.2016.45.
- [14] K. S. Novoselov et al. "Electric field in atomically thin carbon films". In: *Science* 306.5696 (2004), pp. 666–669. DOI: 10.1126/science.1102896.
- [15] Edward Palik. *Handbook of Optical Constants of Solids*. 1st ed. Vol. 3. Academic Press, Mar. 1998.
- [16] N. M.R. Peres, F. Guinea, and A. H. Castro Neto. "Electronic properties of two-dimensional carbon". In: *Ann. Phys. (N. Y)*. 321.7 (2006), pp. 1559–1567. DOI: 10.1016/j.aop.2006.04.006.
- [17] Bahaa E.A. Saleh and Malvin Carl Teich. *Fundamentals of photonics*. 2nd ed. John Wiley & Sons, 2007.
- [18] S Das Sarma et al. "Electronic transport in two-dimensional graphene". In: *Reviews of modern physics* 83.2 (2011), p. 407.
- [19] Frank Stern. "Polarizability of a two-dimensional electron gas". In: *Phys. Rev. Lett.* 18.14 (Apr. 1967), pp. 546–548. DOI: 10.1103/PhysRevLett.18.546.
- [20] Martin Wagner et al. "Ultrafast and nanoscale plasmonic phenomena in exfoliated graphene revealed by infrared pump-probe nanoscopy". In: *Nano Lett.* 14.2 (2014), pp. 894–900. DOI: 10.1021/nl4042577.
- [21] P R Wallace. "The Band Theory of Graphite". In: *Phys. Rev.* 71.9 (May 1947), pp. 622–634. DOI: 10.1103/PhysRev.71.622.

*Chapter 2*

## ACTIVE CONTROL OF GRAPHENE PLASMONS

In this chapter, we discuss the properties of tunable plasmonic modes of graphene nanoresonators near equilibrium conditions across the infrared spectrum. The tunability of graphene plasmons is achieved via electrostatic gating. We use an infrared microscopy to study the roles of graphene plasmons in dynamic control of light absorption, emission, and coupling to various mid-infrared optically active excitations in the near-field environment.

**2.1 Tunable large absorption in graphene**

Graphene exhibits a number of interesting optical phenomena, including a novel photothermoelectric effect [17, 51], strong nonlinear behavior [23, 24], and the potential for ultrafast photodetection [50]. The absolute magnitude of these effects is, however, limited by the degree of light absorption in monolayer graphene, which is typically 2.3%. The graphene-light interaction can be strongly enhanced by using novel light scattering and absorption geometries. Such electromagnetic designs include coupling graphene to resonant metal structures [8, 21, 29, 54–56] or optical cavities where the electromagnetic fields are enhanced [16, 18, 34], or draping graphene over optical waveguides to effectively increase the overall optical path length along the graphene [33, 40]. These methods rely on enhancing interband absorption processes. By doping and patterning graphene, plasmonic modes in graphene can also be explored to achieve strong resonant absorption in the terahertz to mid-infrared regime [3,

11, 28, 52, 53]. It has been theoretically predicted that perfect absorption in graphene can be achieved using tunable graphene nanoresonators coupled to an external cavity, whose structure resembles the original Salisbury screen design [2, 44]. Such a design offers an efficient manner of coupling micron-scale free space light into nanoscale plasmonic modes in graphene. In this work, we construct a device based on the Salisbury screen principle discussed above by placing tunable graphene nanoresonators a fixed distance away from a metallic reflector. A schematic of our device is shown in Fig. 2.1(a). A CVD-grown monolayer graphene was placed on a 1- $\mu\text{m}$ -thick  $\text{SiN}_x$  member with a 200-nm-thick gold layer, which served as both a reflector and a back-gate electrode. Graphene nanoresonators with varying widths ranging from 20 nm to 60 nm were patterned using electron beam lithography. An atomic force microscopy (AFM) image of the resulting graphene nanoresonators is shown in the inset of Fig. 2.1(b). The reflection measurements were done with a Fourier transform infrared (FTIR) microscope with the incoming light polarized perpendicular to the resonators in order to maximize the excitation of the resonant plasmon modes [3, 52]. The graphene carrier density was varied by applying gate voltages across the  $\text{SiN}_x$ , and the resulting changes in graphene resistance are shown in Fig. 2.1(b).

The total absorption from 40 nm graphene nanoresonators is shown in Fig. 2.2(a), revealing a large increase in absorption at  $1400\text{ cm}^{-1}$  and a decrease in absorption near  $3500\text{ cm}^{-1}$  with increasing graphene carrier density. In order to differentiate absorption contributions from graphene from those from the environment (i.e.,  $\text{SiN}_x$  and gold back reflector), the measured absorption was normalized by subtracting absorption from undoped graphene nanores-

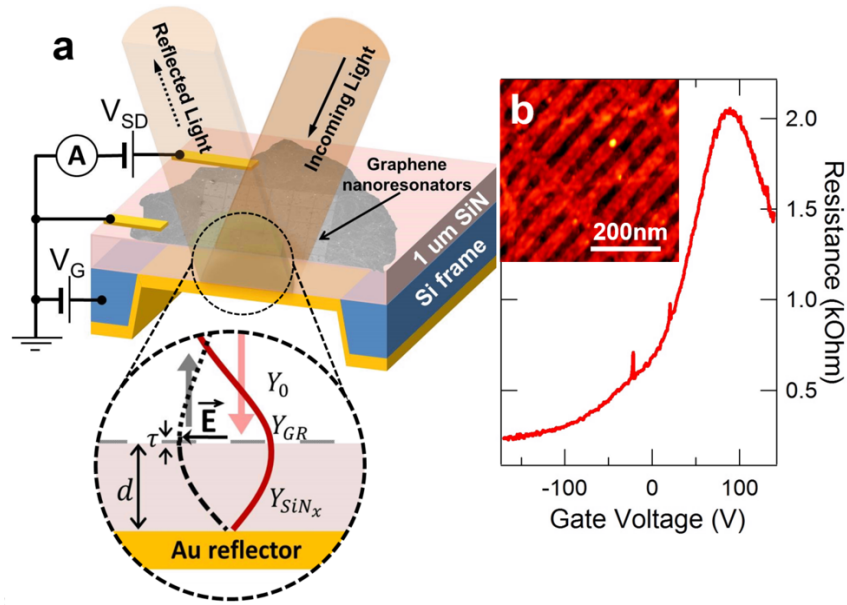


Figure 2.1: (a) Schematic device structure of graphene Salisbury screen. The inset illustrates the device with the optical waves at the resonance condition. (b) dc resistance of graphene as a function of the gate voltage. The gate voltage at which graphene resistance is maximized corresponds to charge neutral point (CNP) of graphene. The inset is an AFM image of 40 nm nano resonators.

onators as shown in Fig. 2.2(b). The normalization removes the carrier-density-independent absorption peak seen below  $1200\text{ cm}^{-1}$ , which is due to the broad optical phonon absorption in the  $\text{SiN}_x$  layer. The absorption feature at  $1400\text{ cm}^{-1}$  shows a dramatic dependence on graphene carrier densities, with absorption into the graphene nano resonators varying from near 0% to 24.5% as the carrier density is raised to  $1.42 \times 10^{13}\text{ cm}^{-2}$ . The absorption feature at  $3500\text{ cm}^{-1}$  exhibits an opposite trend with graphene-related absorption decreasing with higher carrier density. This feature is due to interband graphene absorption, where electronic transitions are Pauli-blocked by state filling at higher carrier densities [47]. The graphene absorption with varying widths of nano resonators was investigated at a fixed graphene carrier density. Figure 2.2(c) shows that the lower energy, plasmonic absorption peak has a strong

frequency and intensity dependence on resonator width, with the maximum absorption occurring in the 40 nm nanoresonators. Figures 2.2(b) and (c) reveal that the intensity of the graphene plasmonic absorption always occurs at  $1400 \text{ cm}^{-1}$ . This observation can be understood by considering the role of the Salisbury screen structure. At  $1400 \text{ cm}^{-1}$ , the optical path length of the  $\text{SiN}_x$  is  $\lambda/4n$ , and the gold reflector creates a standing wave between the incident and reflected light that maximizes the electric field on the  $\text{SiN}_x$  surface. As a consequence, when the graphene nanoresonators are tuned to absorb at  $1400 \text{ cm}^{-1}$ , at which a double resonance condition is met, and the dissipation of the incoming radiation is greatly enhanced. Similarly, the absorption feature at  $3500 \text{ cm}^{-1}$  is due to the second-order interference condition, under which the  $\text{SiN}_x$  optical path length becomes  $3\lambda/4n$ , maximizing the interband absorption. In order to illustrate the role of the interference effect, the electric field intensity on the  $\text{SiN}_x$  surface when graphene is absent is plotted as a dashed curve in Fig. 2.2(c). The spectral dependence of the observed plasmonic absorption displays a similar trend to that seen in the calculated field intensity.

The underlying mechanism for a large resonant absorption observed in this device structure can be understood as satisfying impedance matching conditions. The impedance of the metasurface consisting of graphene nanoresonator arrays is modified in such a way that it mimics a load whose admittance is close to the free-space wave admittance  $Y_0 = \sqrt{\epsilon_0/\mu_0}$ , and allows for the incident light to be coupled efficiently into the graphene sheet [12]. For normally incident light, absorption in graphene located a quarter wavelength away from the back reflector is given by  $A = 1 - |(Y_0 - Y)/(Y_0 + Y)|^2$  [12]. This relation suggests that the absorption in graphene approaches unity as the relative admittance,  $Y/Y_0$ , ap-

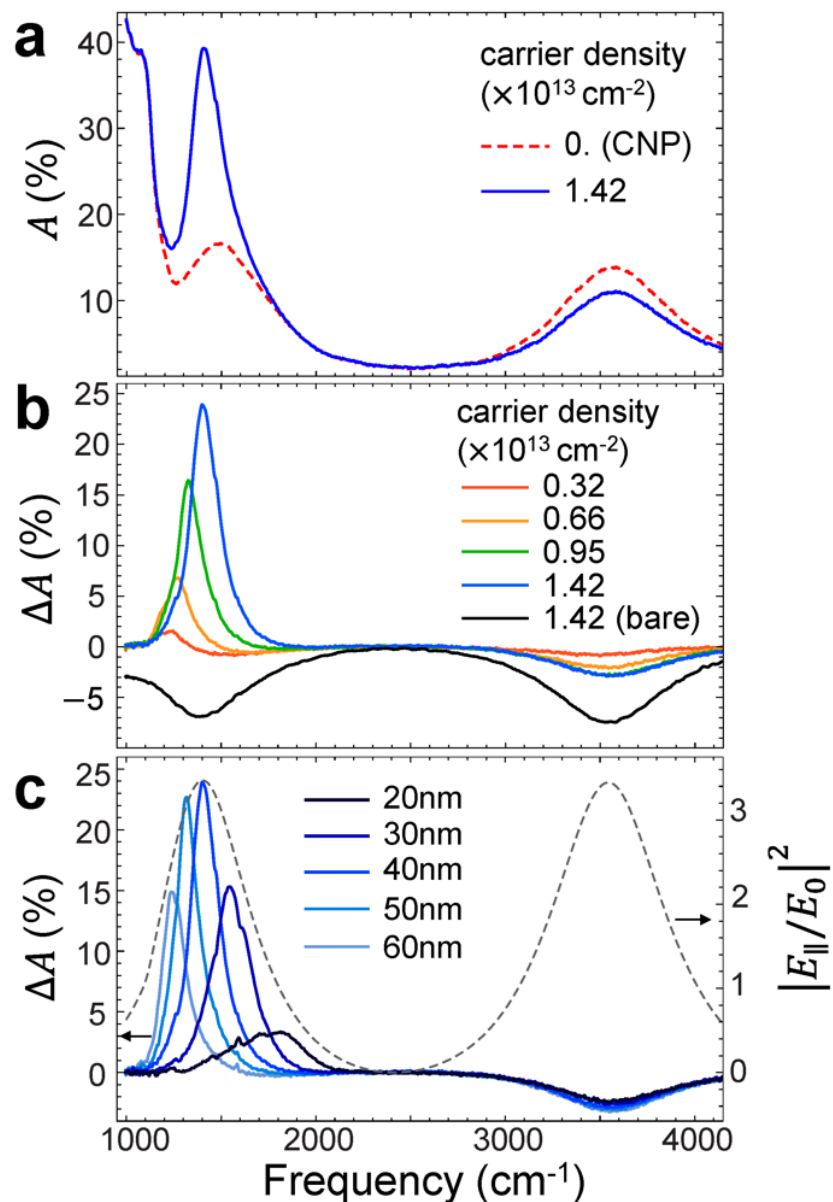


Figure 2.2: (a) The total absorption in the device for undoped (red dashed) and hold doped (blue solid) 40 nm nanoresonators. (b) The change in absorption with respect to the absorption at the charge neutral point (CNP) in 40 nm graphene nanoresonators at various doping levels. The solid black curve represents the absorption difference of bare (unpatterned) graphene. (c) Width dependence of the absorption difference with the carrier concentration of  $1.42 \times 10^{13} \text{ cm}^{-2}$ . The resonator width varies from 20 to 60 nm. The dashed curve shows the theoretical intensity of the surface parallel electric field at the SiN<sub>x</sub> surface when graphene is absent.

proaches 1. The admittance of an unpatterned, planar graphene is equivalent to its sheet conductivity. For photon energies higher than the interband transition energies, the admittance is given by  $Y = \sigma \approx e^2/4\hbar = \pi\alpha Y_0 \approx 0.023Y_0$ , where  $\alpha$  is the fine structure constant. The surface admittance can be dramatically increased when graphene is patterned into optical resonators. On resonance, strong charge oscillations in graphene nanoresonators maximize the dipole moment of the resonators [44]. Recognizing that the absorption cross-section of a dipole is  $\sigma_{\text{Abs}} = (\omega/c)\text{Im}[a(\omega)/\epsilon_0]$ , the surface admittance is given by  $Y = (\sigma_{\text{Abs}}/S)Y_0$  on resonance, where  $a(\omega)$  is the polarizability of an individual resonator, and  $S$  is the area of the unit cell. This relation suggests that unity absorption is possible when the absorption cross-section of the graphene nanoresonator array is large enough to cover the entire surface. For our device at its highest doping level, the resulting surface admittance yields  $0.13Y_0$ , which is an order of magnitude higher than that in unpatterned, planar graphene. The observed resonant absorption can be further increased by improving carrier mobility of graphene. Because the resonator absorption cross-section increases as the graphene becomes less lossy, the resonant surface admittance increases with increasing mobility. This strong optical response allows for graphene to be an attractive platform for optoelectronic applications such as light modulators, detectors, and selective thermal emitters.

## 2.2 Perfect absorption in graphene

A major obstacle for realizing perfect absorption in graphene has been the low carrier mobility in processed graphene samples due to PMMA residues [39] and/or trapped impurities [5] as compared with the high carrier mobilities achievable in pristine, unpatterned graphene sheets [38, 49]. In patterned graphene, edge defects further degrade effective graphene carrier mobilities [10, 15, 45, 46].

In this work, we experimentally demonstrate tunable near-unity absorption in CVD-grown graphene, which exhibits relatively low carrier mobility, covering less than 10% of the surface area by carefully tailoring the graphene plasmonic nanostructure to induce critical coupling to free space (i.e., matching of the admittance of graphene resonators to free space). Such condition is met by utilizing low-permittivity substrates and noble metal plasmonic structures. Lower-permittivity substrates allow better wavevector matching between free-space photons and graphene plasmons. In addition, noble metal plasmonic metallic antennas serve as sub-wavelength-scale intermediaries ( $\sim \lambda_0/10$ , where  $\lambda_0$  is the free-space wavelength) to further enhance radiative coupling to deep sub-wavelength-scale GPRs ( $< \lambda_0/70$ ).

We explore three different device structures and compare their performances (i.e., absorption in graphene) against the previously discussed Salisbury screen structure. All of the studies in this work are oriented towards maximizing absorption in graphene at  $1356 \text{ cm}^{-1}$ , and we consider the graphene carrier mobility as a key metric required to achieve perfect absorption. Figure 2.3 shows three designs for perfect absorption structures.  $\text{SiO}_2$  layers are incorporated int

the type A-C structures beneath the GPRs, while the previously explored Salisbury screen structure consists of only a  $\text{SiN}_x$  layer (which is referred as Type 0). All structures utilize a membrane with a back reflector as a substrate to create the Salisbury screen effect [12, 27, 44]. The type A structure depicted in Figure 2.3(a) consists of periodically arrayed 100-nm-wide gap/100-nm-wide GPRs on the 150-nm-thick  $\text{SiO}_2$ /1- $\mu\text{m}$ -thick  $\text{SiN}_x$ /Au substrate. The type A structure is identical to the original Salisbury screen structure (type 0), except for the thin  $\text{SiO}_2$  layer. By incorporating a thin layer of the low-permittivity layer, a large wavevector mismatch between free-space photons and graphene plasmons can be alleviated [6, 13, 19]. Thus, the type A structure exhibits perfect absorption for a graphene hole mobility of  $\mu_h = 2271 \text{ cm}^2 \text{ V}^{-1} \text{ s}^{-1}$ , while  $\mu_h = 3174 \text{ cm}^2 \text{ V}^{-1} \text{ s}^{-1}$  is required for the type 0 (Fig. 2.4(a)).

We can further alleviate momentum mismatch constraints by incorporating noble metal plasmonic structures. The type B and C structures on the 150-nm-thick  $\text{SiO}_2$ /500-nm-thick  $\text{SiN}_x$ /Au substrates have GPRs located inside subwavelength metallic slits. In the type B structure, a 100-nm-wide GPR is located in the center of a 200-nm-wide metallic slit. In the type C structure, a 50-nm-wide GPR is located off to one side of the 100-nm-wide metallic slit. The widths of the metallic strips in the type B and C structures are 910 and 615 nm, respectively. The metallic slits in the types B and C can concentrate light by exhibiting field enhancement factors of 147 and 226, respectively. For reference, in a original Salisbury screen design, the field strength is enhanced by a factor 4. The narrower metallic slits in the type C result in a larger field enhancement by more efficiently confining radiation. The graphene hole mobilities required to achieve perfect absorption are 613 and 315  $\text{cm}^2 \text{ V}^{-1}$

$s^{-1}$  for the type B and C, respectively (Fig. 2.4(a)). A carrier mobility of approximately  $500 \text{ cm}^2 \text{ V}^{-1} \text{ s}^{-1}$  is easily achievable in a CVD-grown large area graphene. Thus, perfect absorption is no longer limited by low graphene carrier mobility.

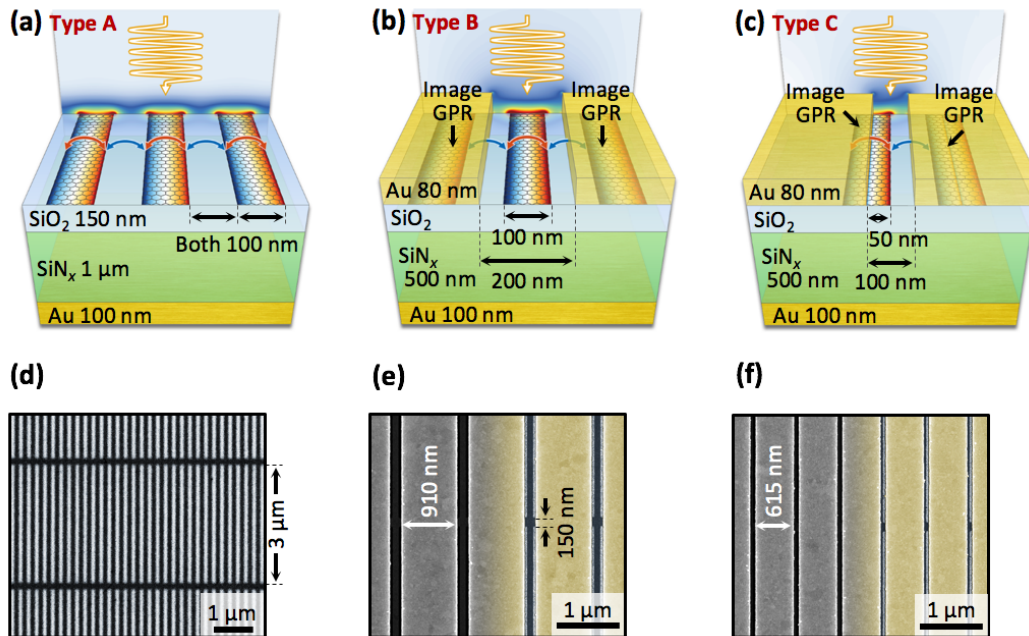


Figure 2.3: Schematic of (a-c) type A, B, and C structures, respectively. In parts a-c, panels at the back side present the out-of-plane electric field distributions, and  $E_z$  distributions in graphene are overlapped on graphene plasmonic ribbons (GPRs). The images of GPRs in panels b and c are the virtual GPRs created by metallic strips, which operate as mirrors. (d-f) Corresponding scanning electron microscope (SEM) images (false color). The dark and bright regions correspond to GPRs and exposed SiO<sub>2</sub> areas, respectively. The GPRs have 150-nm-wide bridges to ensure electrical connections, and the length of the GPR strip is 3  $\mu\text{m}$ .

Finally, we experimentally demonstrate electronically tunable near-unity resonant absorption via the reflection measurements in a Fourier transform infrared (FTIR) microscope with a polarizer. As shown in Fig. 2.4(c), the metallic plasmonic structures and the substrate contribute little to the total absorption. Thus, the absorption of a structure can be obtained by  $1 - R$ , where  $R$  is the reflectance of a corresponding structure. The modulation efficiencies in reflection were calculated by  $\eta_R = 1 - R/R_{\max}$ , where  $R_{\max}$  is the reflectance when the absorption is minimized at a given graphene Fermi level. The experimentally measured spectra are shown in Fig. 2.5. In type A, the resonant absorption is increased from 14.0% to 52.4%, demonstrating an on/off modulation efficiency of 44.6% at  $1400 \text{ cm}^{-1}$ . In type B, the resonant absorption is increased from 24.8% to 96.9%, demonstrating an on/off modulation efficiency of 95.9% at  $1389 \text{ cm}^{-1}$ . In type C, the resonant absorption is increased from 29.6% to 94.8%, demonstrating an on/off modulation efficiency of 92.6% at  $1407 \text{ cm}^{-1}$ . These experimental results indicate perfect absorption can be achieved in an atomically thin layer of material, which covers less than 10% of the surface.

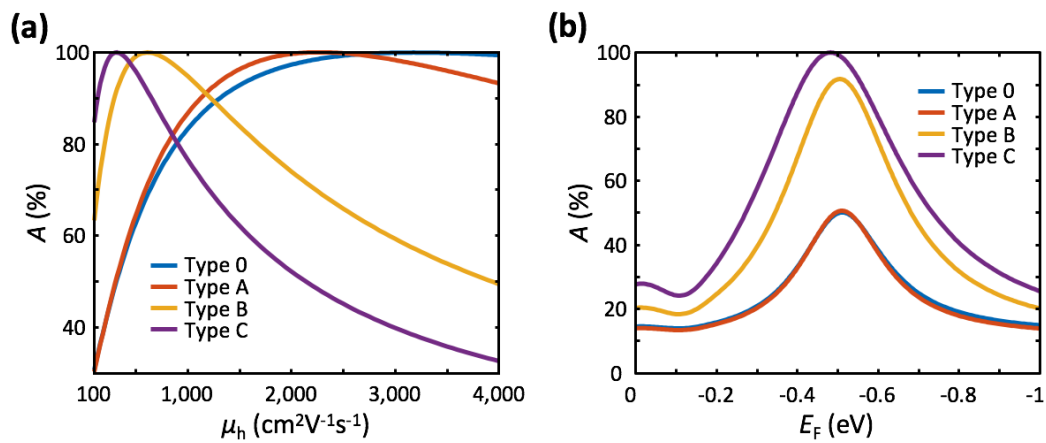


Figure 2.4: (a) Absorption in type 0, A, B, and C at  $1356\text{ cm}^{-1}$  as a function of graphene hole mobility ( $\mu_h$ ). (b) Tunable absorption in each structure as a function of graphene Fermi level ( $E_F$ ) for  $\mu_h = 315\text{ cm}^2\text{ V}^{-1}\text{ s}^{-1}$ .

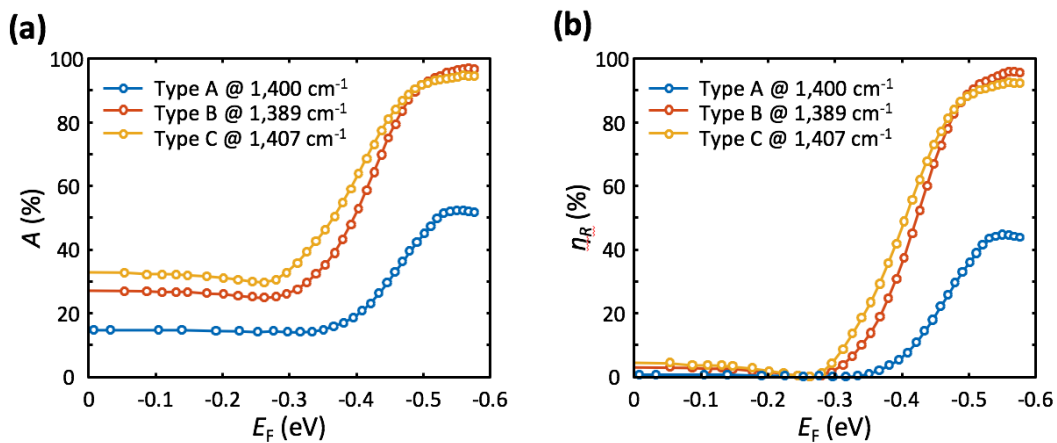


Figure 2.5: (a) Absorption and (b) modulation efficiency as a function of graphene Fermi level ( $E_F$ ) at the frequency for maximum absorption in each structure.

### 2.3 Tunable graphene plasmon dispersion relation and emergence of hybrid surface-phonon-plasmon polariton modes

The ability of graphene plasmons to focus electric field into smaller volumes allows graphene plasmons to couple strongly to optical excitations in its local environment, such as molecular vibrations [35], phonons [25], or excitons [7, 42, 43], than normal metal plasmons. The mode volume associated with the plasmonic modes in graphene nanoresonators has been experimentally demonstrated to be approximately  $10^7$  times smaller than free space. In comparison, surface plasmons supported by normal metals typically display mode volumes are than  $10^3$  times smaller than free space with similar damping. In this work, we experimentally show that graphene plasmons strongly couple to optical phonons of a monolayer hexagonal boron nitride (h-BN) sheet, and as a result, report an emergence of new hybrid modes referred to as surface-phonon-plasmon-polaritons (SPPPs). This phenomenon has been explored in surface plasmons of conventional noble metals coupled to underlying molecular vibrations or dyes [1, 7, 22, 36, 37, 43]; in these studies, a thick ( $>20\text{nm}$ ) layer of optically active material was required. On the other hand, the high confinement associated graphene plasmons allows strong and sensitive interaction with a small volume of optical phonons in an atomically thin material.

A schematic of the device is shown in Fig. 2.6. A CVD-grown monolayer h-BN sheet was transferred to a 285-nm-thick  $\text{SiO}_2/\text{Si}$  wafer, and a CVD-grown graphene sheet was subsequently transferred onto the h-BN. Nanoresonators were patterned into the graphene surface to form electronically continuous bar array patterns with widths ranging from 30 to 300 nm. We performed Fourier transform infrared spectroscopy (FTIR) transmission measurements

with light polarized perpendicular to the width of the nanoresonators to probe the frequency-wavevector dispersion relations of the electromagnetically coupled graphene plasmon/h-BN phonon modes. The transmission spectra from the graphene nanoresonators are shown in Fig. 2.7. The measured transmission spectra were normalized relative to spectra taken with zero carrier density. The narrow peak seen in the bare h-BN spectrum near  $1370\text{ cm}^{-1}$  has been assigned in previous studies as an in-plane optical phonon of the h-BN [20]. Two sets of modes below and above  $1200\text{ cm}^{-1}$  were observed. The two modes below  $1200\text{ cm}^{-1}$  were previously observed in graphene/SiO<sub>2</sub> structures, and have been assigned to SPPP modes associated with two SiO<sub>2</sub> modes [3, 52]. The two modes above  $1200\text{ cm}^{-1}$  display anticrossing behavior near the  $1370\text{ cm}^{-1}$ , optical phonon energy of the h-BN due to the coupling of graphene plasmon mode and h-BN phonon mode.

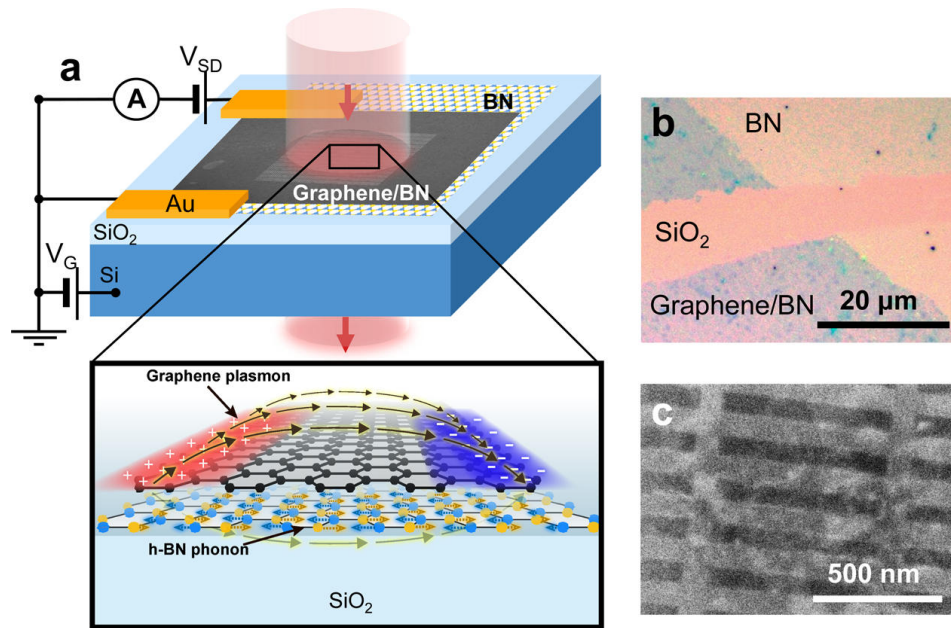


Figure 2.6: (a) Schematic of device measured and modeled in this work. Graphene nanoresonators are fabricated on a monolayer h-BN sheet on a SiO<sub>2</sub>(285 nm)/Si wafer. Gold contact pads are used to contact the graphene sheet, and the Si wafer is used to apply an in situ backgate voltage ( $V_G$ ). Zoom-in shows cartoon of graphene plasmon coupling to h-BN optical phonon. (b) Optical image of unpatterned area of device where both the graphene and h-BN monolayers have been mechanically removed. (c) Scanning electron microscope image of the 80 nm graphene nanoresonators (light regions).

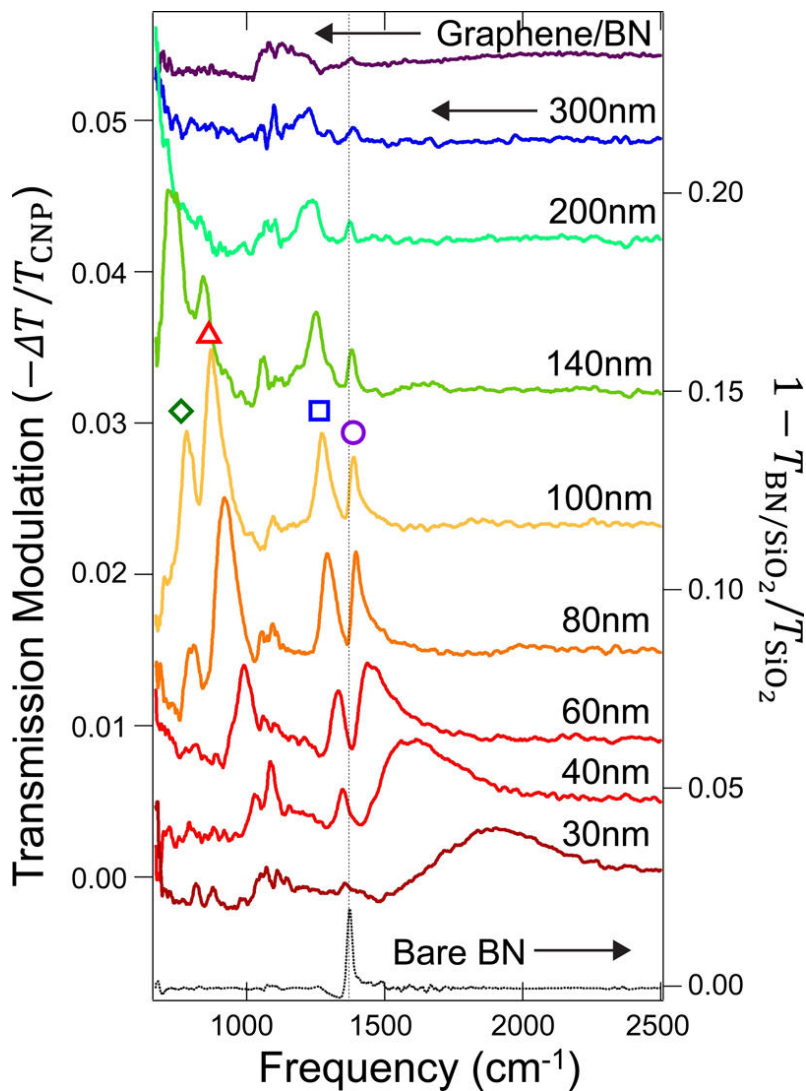


Figure 2.7: (Left axis) Normalized transmission spectra of graphene nanoresonators with widths varying from 30 to 300 nm, as well as transmission through the unpatterned graphene/h-BN sheet. Spectra are measured at carrier densities of  $1.0 \times 10^{13} \text{ cm}^{-2}$  and normalized relative to zero carrier density. For 80 nm ribbons, the four different observable optical modes are labeled with the symbols used to indicate experimental data points in Fig. 2.8. (Right axis, bottom spectrum) Infrared transmission of the bare monolayer h-BN on  $\text{SiO}_2$  normalized relative to transmission through the  $\text{SiO}_2(285 \text{ nm})/\text{Si}$  wafer. The dotted vertical line indicates this peak position as a reference for the other spectra.

For a comparison with the experimental results, the transmission spectra of graphene nanoresonators for various widths were calculated using a finite el-

ement method within a local random phase approximation [9]. The in-plane dielectric function of monolayer h-BN is described using a Lorentz oscillator model with parameters fitted from transmission measurement of the bare h-BN on SiO<sub>2</sub> [20], and its thickness is modeled to be 0.34 nm, which is the interlayer spacing of bulk h-BN. The first-order plasmon resonance with the width,  $W$ , was calculated using  $k_p = (\pi - \phi)/W$ , where  $\phi$  is the plasmon phase shift upon reflection at the nanoresonator edges. According to simulations in Ref. [3],  $\phi$  is found to be approximately  $0.35\pi$ . The graphene-carrier-density-dependent transmission is plotted in Fig. 2.8 for varying wavevector and energy. The dispersion of the graphene/h-BN/SiO<sub>2</sub> nanoresonator optical modes can be observed in Fig. 2.8 as the maxima in the transmission modulation,  $-\Delta T/T_{\text{CNP}}$ . The features observed in the calculations are in good agreement with the experimentally measured features with modes appearing above and below the h-BN optical phonon energy that display a clear anti-crossing behavior. The relative intensities associated with these two modes change with widths of the graphene nanoresonators. In addition, a pronounced minimum in absorption near the h-BN phonon energy was seen for 60, 80, and 100 nm nanoresonators, whose bare-graphene plasmon resonance energies overlap with that of the h-BN phonon mode. When the graphene plasmon mode is brought into resonance with the h-BN phonon, the polarizations of the two modes cancel each other out, creating a transparency window where no absorption occurs in the plasmonic modes. A classical strong coupling regime is characterized by a splitting between the two hybridized modes larger than the sum of the two line widths of individual modes and also its spectral intensity approaching zero.

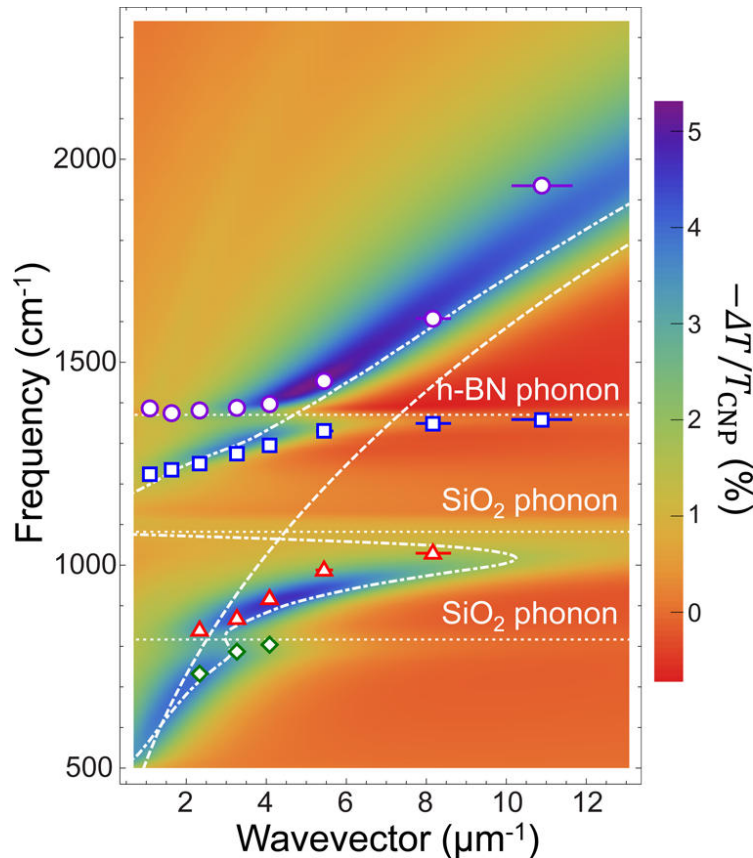


Figure 2.8: Calculated change in transmission for graphene/monolayer hiBN/SiO<sub>2</sub> nanoresonators of varying width at a carrier density of  $1.0 \times 10^{13} \text{ cm}^{-2}$ , normalized relative to zero carrier density. Experimental data is plotted as symbols indicating optical modes assigned in Fig 2.7. The error bars represent uncertainty in the resonator width that is obtained from AFM measurements. For small  $k$ -vectors (large resonators), this uncertainty is smaller than the symbol size. The dashed line indicates the theoretical dispersion for bare graphene plasmons, while the dash-dot line indicates the dispersion for graphene/SiO<sub>2</sub>. The three horizontal dotted lines indicate the optical phonon energies of h-BN and SiO<sub>2</sub>.

As shown in Fig. 2.9, the coupling strength varies with the spacing between graphene ribbons and the h-BN layer. The splitting between two hybrid SPPP modes and the depth of the transparency window rapidly decrease as the interlayer distance increases. Due to the large mode confinement of graphene plasmons, the range of interaction is restricted to tens of nanometers from the graphene sheet. The small volume of the h-BN sheet indicates that a very

small number of optical excitations with large oscillator strengths are sufficient to achieve strong coupling to graphene plasmons, as long as the excitations are in the immediate vicinity of the graphene sheet. This work indicates that graphene nanoresonators can serve as extremely sensitive probes of their local environments, and also opens the door for further investigations employing excitations of single or a few quanta interacting with the graphene plasmons.

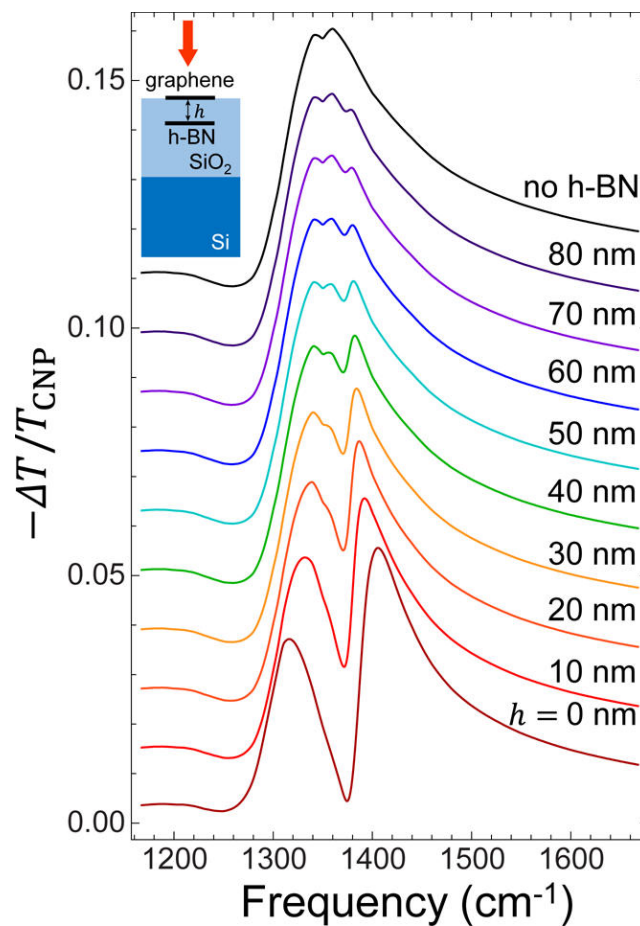


Figure 2.9: Calculated transmission spectra for 80-nm-wide graphene resonator/top  $\text{SiO}_2$ /80-nm-wide monolayer h-BN/bottom  $\text{SiO}_2$  as the top  $\text{SiO}_2$  layer thickness is varied from 0 to 80 nm in 10 nm increments. Spectra are for a carrier density of  $1.0 \times 10^{13} \text{ cm}^{-2}$  and normalized relative to zero carrier density.

## 2.4 Tunable Planckian Thermal Emission

Graphene plasmonic modes have shown to create strong absorption pathways in mid-infrared when the graphene is patterned to form plasmonic Fabry-Perot resonances. Furthermore, they display extremely large mode confinement, which allows them to efficiently couple to local excitations to create new optical modes [3, 4, 31, 52]. As the graphene sheet is heated up, all of these different infrared absorption pathways become thermal emission sources, as Kirchoff's law ensures that thermal emissivity is equal to absorptivity under thermal equilibrium. The graphene plasmons are particularly interesting as thermal emitters because their small mode volumes allow for large Purcell factors that can enhance the emission rate of emitters within the plasmon mode volume [30]. Thus, electronic control of the graphene plasmonic modes could potentially control thermal radiation at timescales much faster than the spontaneous emission rate for conventional light emitting diodes and classical blackbody emission sources. Thermal emission is typically considered as broadband and slow light emitting process.

In this work, we demonstrate that the dynamic tuning of blackbody emission through electronic control of graphene plasmonic resonators. The graphene nanoresonators act as antennas to effectively out-couple thermal energy within the resonator mode volume, and change effective surface emissivities with varying carrier densities and widths of nanoresonators, giving rise to dynamically tunable narrow spectral emission peaks in the mid-infrared. A schematic of the measurement apparatus and device geometry are shown in Fig. 2.10. The device geometry is identical to the original Salisbury screen geometry discussed in the previous section, which was used as a gate-tunable absorber in the mid-

infrared spectral range [27, 44]. In the previous reflection measurements, the polarized absorption in the graphene nanoresonators could be tuned from 0% to up to 24.5% for large carrier densities. In this work, the device displayed up to 3% total absorption when probed using our apparatus. This smaller number reflects the use of non-polarized light, the higher numerical aperture objective of the apparatus, the effect of the window of the vacuum stage, and the lower carrier densities used due to the onset of Poole-Frenkel tunnelling in the  $\text{SiN}_x$  at higher temperatures and high gate biases [27].

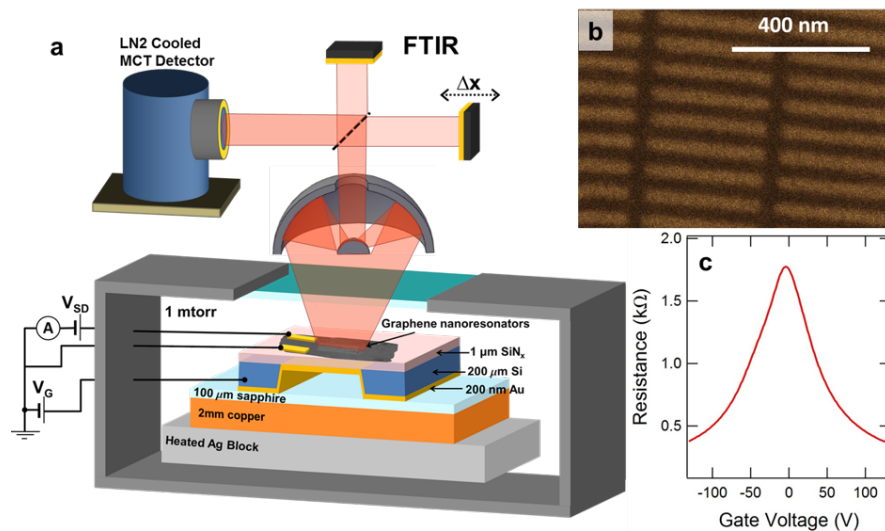


Figure 2.10: (a) Schematic of the experimental apparatus. The  $70\ \mu\text{m} \times 70\ \mu\text{m}$  graphene nanoresonator arrays are placed on a  $1\text{-}\mu\text{m}$ -thick  $\text{SiN}_x$  membrane with a  $200\text{-nm}$ -thick gold backreflector. A gate bias is applied through the  $\text{SiN}_x$  membrane between the underlying Si frame and graphene sheet. The temperature-controlled stage contains a feedback controlled, heated silver block that holds a  $2\text{-mm}$ -thick copper sample carrier with a  $100\text{-}\mu\text{m}$ -thick sapphire layer used for electrical isolation. The temperature is monitored with a thermocouple in the block, and the stage is held at a vacuum of 1 mtorr. A  $1\text{-mm}$ -thick potassium bromide (KBr) window is used to pass thermal radiation out of the stage, which is collected with a Cassegrain objective and passed into an FTIR with an MCT detector. (b) A representative SEM image of  $30\text{-nm}$ -wide graphene nanoresonators on a  $1\text{-}\mu\text{m}$ -thick  $\text{SiN}_x$  membrane. (c) Source-drain resistance versus gate voltage curve of the device. The peak in the resistance occurs at the charge neutral point (CNP) of graphene.

In Fig. 2.11, the change in emissivity is obtained assuming unity emissivity at all frequencies for the black soot reference and normalizing the measured emission spectra accordingly. We investigate gate-tunable emissivity features as the nanoresonator doping and width is varied, as well as their polarization dependence. These results indicate that the intensity, width and energetic position of the thermal radiation feature near  $1,360 \text{ cm}^{-1}$  are widely tunable, and that this feature is strongly polarized. The energy of this feature increases as the nanoresonator width is decreased and as the carrier density is increased. These observations are consistent with previously reported absorption measurements performed on identical samples that showed a narrow absorption feature near  $1,360 \text{ cm}^{-1}$  [27]. Thus, we attribute the prominent spectral feature at  $1,360 \text{ cm}^{-1}$  to a Fabry-Perot plasmonic resonance from the patterned graphene. Specifically, the graphene plasmon resonant frequency should vary as  $\omega_p \propto n^{1/4}W^{-1/2}$ , where  $n$  is the graphene carrier density, and  $W$  is the resonator width. This behavior is in accord with the emission spectra, in which we observe a blue shift of the plasmonic resonance at increased doping and decreased graphene nanoresonator width. The intensity of the higher-energy peak increases with graphene carrier density, an effect that results from the increased polarizability of the resonant plasmonic modes. Finally, this feature is strongly polarization dependent, as we would expect for laterally confined graphene plasmonic resonant modes, and vanishes quickly as we rotate the polarization of the probing radiation from  $90^\circ$  to  $0^\circ$  relative to the nanoresonator axis.

The microscopic processes which give rise to thermally excited plasmons in the nanoresonators are expected to correspond to the plasmonic loss processes

as emission is a reciprocal process of absorption in thermal equilibrium. The plasmonic loss processes are attributed to the factors that limit the electron mobility of the graphene, such as defect scattering, impurity scattering, and inelastic electron–electron and electron–phonon interactions [3, 26, 27, 41, 52]. In addition, plasmons have been shown to decay via loss channels associated with the edges of graphene nanostructures and by coupling to substrate phonons [3, 52]. The resonant enhancement of emission from plasmon generating processes is in competition with the blocking of interband transitions that act as thermal emitters in the undoped graphene, but are forbidden due to Pauli blocking when the sheet is doped [32, 48]. While interband transitions should occur across a wide range of frequencies, for patterned graphene areas, we find that doping the graphene allows for the resonant plasmonic modes to create an emission enhancement that outweighs the decrease in emission due to Pauli blocking. Thus, we get a net increase in emission near  $1,360 \text{ cm}^{-1}$ . The plasmonic resonators also interact with vibrations in the  $\text{SiN}_x$  substrate. When the  $\text{SiN}_x$  is heated, the plasmonic modes act as antennae to enhance the spontaneous thermal radiation from the nearby  $\text{SiN}_x$ . The spontaneous emission radiative rate is enhanced by the graphene nanoresonators, which modify the photonic mode density. The rate enhancement is correlated to the strong polarizability of the graphene at its plasmonic resonance that enhances the outcoupling of thermal radiation from the  $\text{SiN}_x$ . In particular, the radiative rate is expected to be most strongly amplified within the mode volume of the resonant graphene plasmon, which for 40 nm resonators at  $1.2 \times 10^{13} \text{ cm}^{-2}$  roughly corresponds to the area within 10 nm of the resonator. Therefore, we assign the net increase of thermal emission near  $1,360 \text{ cm}^{-1}$  to a combination

of thermal excitations in the graphene as well as thermal phonons in the  $\text{SiN}_x$  that is out-coupled through the confined plasmonic modes in the graphene nanoresonators. In contrast to the emissivity features seen in the high-energy peak, the lower-energy emissivity modulation feature near  $730 \text{ cm}^{-1}$  shows an extremely weak polarization dependence and no noticeable dependence on graphene nanoresonator width. As the carrier density is increased, there is a small, non-monotonic increase in intensity for this feature, but it shows no spectral shift. Finally, unlike the higher-energy peak, the lower-energy peak is also observed in the bare, unpatterned graphene, where it appears as a slightly narrower feature. The low-energy feature is related to an optically active phonon in the  $\text{SiN}_x$  substrate. This phonon mode is strongly absorbing (emitting) and is typically located near  $850 \text{ cm}^{-1}$ . The large divergence in the  $\text{SiN}_x$  permittivity due to this phonon, however, creates an additional  $\lambda/4n_{\text{SiN}_x}$  condition in the structure that leads to a destructive interference effect, resulting in an absorption (emission) maximum at  $730 \text{ cm}^{-1}$ . When graphene is placed on top of the  $\text{SiN}_x$ , the intraband and interband transitions in the graphene act to modify the surface impedance of the device. The result is that increasing the doping in the graphene leads to a stronger destructive interference effect, which manifests as larger emission from the  $\text{SiN}_x$  layer. The graphene plasmons can couple to the  $\text{SiN}_x$  phonons to create new surface phonon plasmon polariton modes [3, 4, 14, 52]. Since the observed low-energy emissivity features show no polarization dependence, an increase in direct emission from the  $\text{SiN}_x$  layer likely plays the dominant role in creating the feature at  $730 \text{ cm}^{-1}$ .

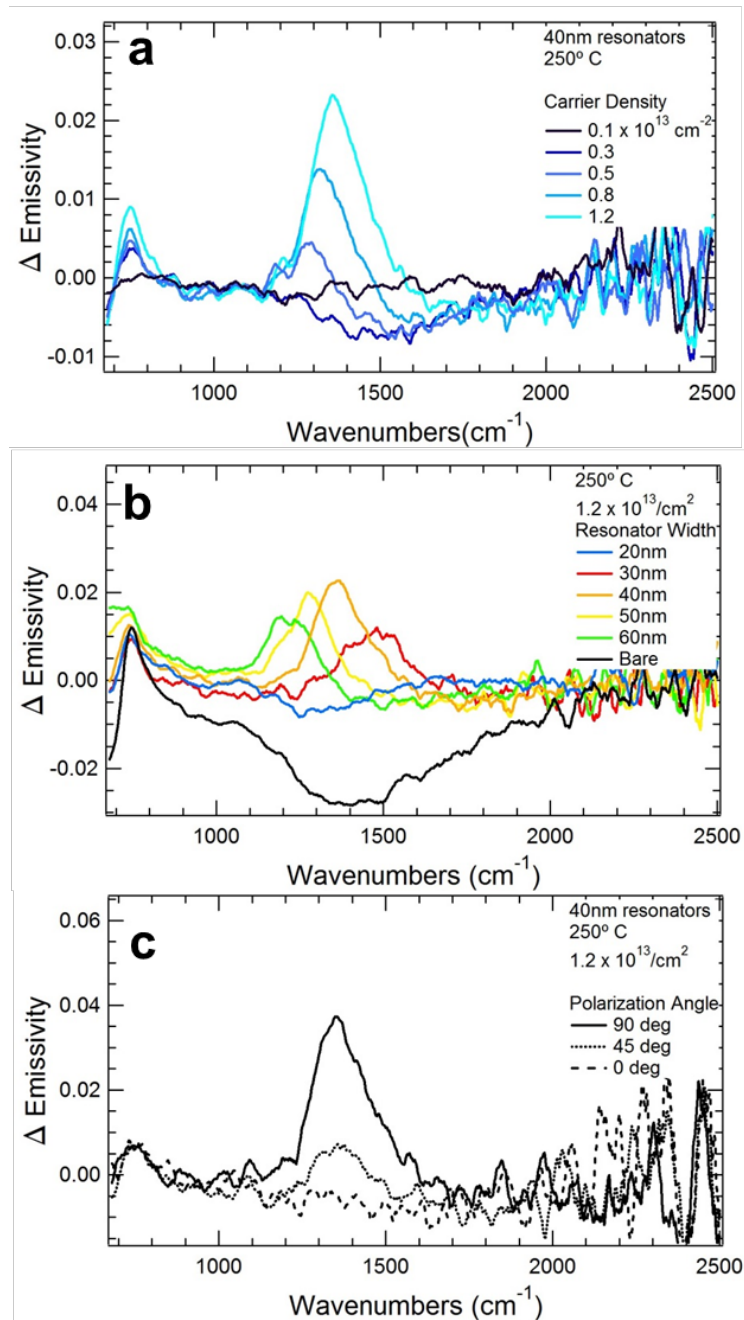


Figure 2.11: (a) Carrier density dependence of change in emissivity with respect to the CNP for 40-nm-wide graphene nanoresonators at 250°C. (b) Width dependence of change in emissivity for 20-, 30-, 40-, 50-, 60-nm-wide nanoresonators at 250°C and for a carrier density of  $1.2 \times 10^{13} \text{ cm}^{-2}$ . The black line indicates the emissivity changes of bare, unpatterned graphene at the same carrier density and temperature. (c) Polarization dependence of the emissivity change for 40 nm graphene nanoresonators at 250 °C for a carrier density of  $1.2 \times 10^{13} \text{ cm}^{-2}$ .

Here we test our structure as a mid-infrared spontaneous light source at higher speeds, and demonstrate a 2 kHz modulation of graphene-nanoresonator-coupled thermal emission. We performed time-resolved emission measurements on 50-nm-wide resonators at 250°C. A 2-kHz-modulated square wave signal was applied to the structure, with an “off” voltage of 0V, corresponding to the CNP of graphene and an “on” voltage of 60V, corresponding to a graphene carrier density of  $1.2 \times 10^{13} \text{ cm}^{-2}$ . The emission modulation was measured as a raw voltage signal from a FTIR MCTA detector using an infrared filter with transmission peaked at  $1,383 \text{ cm}^{-1}$  and central bandwidth of approximately  $30 \text{ cm}^{-1}$ . This filter was selected to match the resonance frequency of the 50nm resonators at a doping of  $1.2 \times 10^{13} \text{ cm}^{-2}$ , therefore isolating the plasmonic signal. The measurement results along with the applied voltage temporal waveform are shown in Fig. 2.12. A clearly modulated emission signal is seen in response to the input square wave. In these measurements, the maximum modulation frequency was 2 kHz due to limitations in the speed of the detector and the RC time constant of the combined graphene nanoresonator device, contact resistance, and electrical leads. This frequency is not indicative of the inherent upper limits of the structure itself. As shown in Fig. 2.12, the applied voltage signal exhibits a sharp rise time, indicating that the primary limitations here are from the detector response.

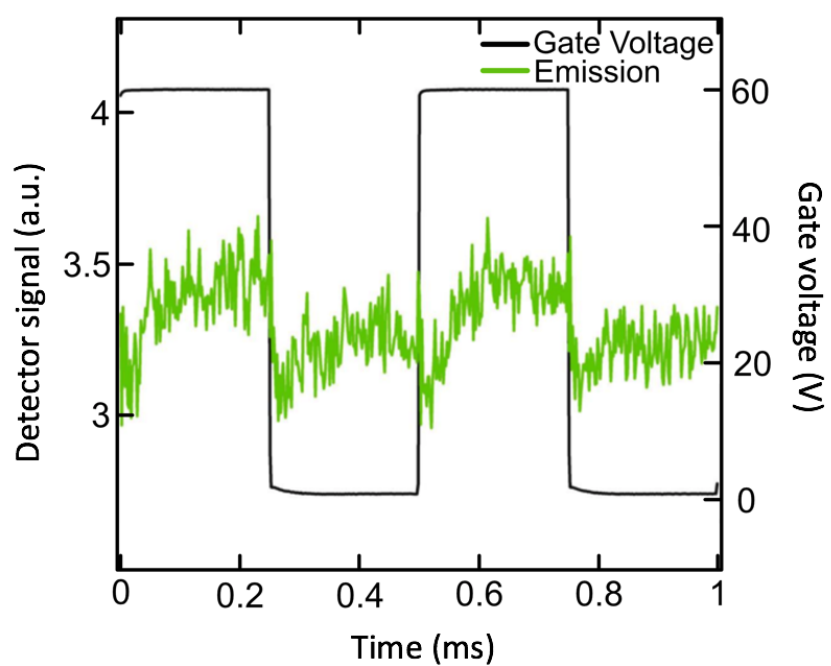


Figure 2.12: Temporal waveform of applied voltage signal (black line) and detector signal of emission from 50 nm ribbons at 250°C (green line).

## References

- [1] Ronen Adato et al. "Ultra-sensitive vibrational spectroscopy of protein monolayers with plasmonic nanoantenna arrays". In: *Proceedings of the National Academy of Sciences* 106.46 (2009), pp. 19227–19232. DOI: 10.1073/pnas.0907459106. eprint: <https://www.pnas.org/content/106/46/19227.full.pdf>.
- [2] Rasoul Alaee et al. "A perfect absorber made of a graphene micro-ribbon metamaterial". In: *Optics express* 20.27 (2012), pp. 28017–28024.
- [3] Victor W. Brar et al. "Highly Confined Tunable Mid-Infrared Plasmonics in Graphene Nanoresonators". In: *Nano Letters* 13.6 (2013). PMID: 23621616, pp. 2541–2547. DOI: 10.1021/nl400601c. eprint: <https://doi.org/10.1021/nl400601c>.
- [4] Victor W. Brar et al. "Hybrid surface-phonon-plasmon polariton modes in graphene/monolayer h-BN heterostructures". In: *Nano Lett.* 14.7 (2014), pp. 3876–3880. DOI: 10.1021/nl501096s.
- [5] Jack Chan et al. "Reducing extrinsic performance-limiting factors in graphene grown by chemical vapor deposition". In: *ACS nano* 6.4 (2012), pp. 3224–3229.
- [6] Thomas J Constant et al. "All-optical generation of surface plasmons in graphene". In: *Nature Physics* 12.2 (2016), p. 124.
- [7] J Dintinger et al. "Strong coupling between surface plasmon-polaritons and organic molecules in subwavelength hole arrays". In: *Physical Review B* 71.3 (2005), p. 035424.
- [8] Naresh K Emani et al. "Electrical modulation of fano resonance in plasmonic nanostructures using graphene". In: *Nano letters* 14.1 (2013), pp. 78–82.
- [9] L. A. Falkovsky and A. A. Varlamov. "Space-time dispersion of graphene conductivity". In: *Eur. Phys. J. B* 56.4 (2007), pp. 281–284. DOI: 10.1140/epjb/e2007-00142-3.
- [10] Tian Fang et al. "Mobility in semiconducting graphene nanoribbons: Phonon, impurity, and edge roughness scattering". In: *Physical Review B* 78.20 (2008), p. 205403.
- [11] Zheyu Fang et al. "Gated tunability and hybridization of localized plasmons in nanostructured graphene". In: *ACS nano* 7.3 (2013), pp. 2388–2395.
- [12] Ronald L Fante and Michael T McCormack. "Reflection properties of the Salisbury screen". In: *IEEE transactions on antennas and propagation* 36.10 (1988), pp. 1443–1454.

- [13] Zhe Fei et al. "Gate-tuning of graphene plasmons revealed by infrared nano-imaging". In: *Nature* 487.7405 (2012), p. 82.
- [14] Zhe Fei et al. "Infrared nanoscopy of Dirac plasmons at the graphene-SiO<sub>2</sub> interface". In: *Nano letters* 11.11 (2011), pp. 4701–4705.
- [15] Z Fei et al. "Edge and surface plasmons in graphene nanoribbons". In: *Nano letters* 15.12 (2015), pp. 8271–8276.
- [16] Marco Furchi et al. "Microcavity-integrated graphene photodetector". In: *Nano letters* 12.6 (2012), pp. 2773–2777.
- [17] Nathaniel M. Gabor et al. "Hot Carrier-Assisted Intrinsic Photoresponse in Graphene". In: *Science* 334.6056 (2011), pp. 648–652. DOI: 10.1126/science.1211384. eprint: <https://science.sciencemag.org/content/334/6056/648.full.pdf>.
- [18] Xuetao Gan et al. "Strong Enhancement of Light-Matter Interaction in Graphene Coupled to a Photonic Crystal Nanocavity". In: *Nano Letters* 12.11 (2012). PMID: 23043452, pp. 5626–5631. DOI: 10.1021/nl302746n. eprint: <https://doi.org/10.1021/nl302746n>.
- [19] F Javier Garcia de Abajo. "Graphene plasmonics: challenges and opportunities". In: *Acs Photonics* 1.3 (2014), pp. 135–152.
- [20] R Geick, CH Perry, and G Rupprecht. "Normal modes in hexagonal boron nitride". In: *Physical Review* 146.2 (1966), p. 543.
- [21] M Grande et al. "Fabrication of doubly resonant plasmonic nanopatch arrays on graphene". In: *Applied Physics Letters* 102.23 (2013), p. 231111.
- [22] T. K. Hakala et al. "Vacuum Rabi Splitting and Strong-Coupling Dynamics for Surface-Plasmon Polaritons and Rhodamine 6G Molecules". In: *Phys. Rev. Lett.* 103 (5 July 2009), p. 053602. DOI: 10.1103/PhysRevLett.103.053602.
- [23] Hayk Harutyunyan, Ryan Beams, and Lukas Novotny. "Controllable optical negative refraction and phase conjugation in graphite thin films". In: *Nature Physics* 9.7 (2013), p. 423.
- [24] Euan Hendry et al. "Coherent nonlinear optical response of graphene". In: *Physical review letters* 105.9 (2010), p. 097401.
- [25] R Hillenbrand, T Taubner, and F Keilmann. "Phonon-enhanced light-matter interaction at the nanometre scale". In: *Nature* 418.6894 (2002), p. 159.
- [26] Marinko Jablan, Hrvoje Buljan, and Marin Soljačić. "Plasmonics in graphene at infrared frequencies". In: *Phys. Rev. B - Condens. Matter Mater. Phys.* 80.24 (2009), pp. 1–7. DOI: 10.1103/PhysRevB.80.245435.

- [27] Min Seok Jang et al. "Tunable large resonant absorption in a midinfrared graphene Salisbury screen". In: *Phys. Rev. B - Condens. Matter Mater. Phys.* 90.16 (Oct. 2014), p. 165409. DOI: 10.1103/PhysRevB.90.165409.
- [28] Long Ju et al. "Graphene plasmonics for tunable terahertz metamaterials". In: *Nature nanotechnology* 6.10 (2011), p. 630.
- [29] Jonghwan Kim et al. "Electrical control of optical plasmon resonance with graphene". In: *Nano letters* 12.11 (2012), pp. 5598–5602.
- [30] Frank HL Koppens, Darrick E Chang, and F Javier Garcia de Abajo. "Graphene plasmonics: a platform for strong light-matter interactions". In: *Nano letters* 11.8 (2011), pp. 3370–3377.
- [31] Yilei Li et al. "Graphene plasmon enhanced vibrational sensing of surface-adsorbed layers". In: *Nano letters* 14.3 (2014), pp. 1573–1577.
- [32] ZQ Li et al. "Dirac charge dynamics in graphene by infrared spectroscopy". In: *Nature Physics* 4.7 (2008), p. 532.
- [33] Ming Liu et al. "A graphene-based broadband optical modulator". In: *Nature* 474.7349 (2011), p. 64.
- [34] Arka Majumdar et al. "Electrical control of silicon photonic crystal cavity by graphene". In: *Nano letters* 13.2 (2013), pp. 515–518.
- [35] Martin Moskovits. "Surface-enhanced spectroscopy". In: *Reviews of modern physics* 57.3 (1985), p. 783.
- [36] Dietmar Nau et al. "Hydrogen sensor based on metallic photonic crystal slabs". In: *Optics letters* 35.18 (2010), pp. 3150–3152.
- [37] Frank Neubrech et al. "Resonant Plasmonic and Vibrational Coupling in a Tailored Nanoantenna for Infrared Detection". In: *Phys. Rev. Lett.* 101 (15 Oct. 2008), p. 157403. DOI: 10.1103/PhysRevLett.101.157403.
- [38] Kostya S Novoselov et al. "Two-dimensional gas of massless Dirac fermions in graphene". In: *nature* 438.7065 (2005), p. 197.
- [39] A Pirkle et al. "The effect of chemical residues on the physical and electrical properties of chemical vapor deposited graphene transferred to SiO<sub>2</sub>". In: *Applied Physics Letters* 99.12 (2011), p. 122108.
- [40] Andreas Pospischil et al. "CMOS-compatible graphene photodetector covering all optical communication bands". In: *Nature Photonics* 7.11 (2013), p. 892.
- [41] Alessandro Principi et al. "Intrinsic lifetime of Dirac plasmons in graphene". In: *Physical Review B* 88.19 (2013), p. 195405.

- [42] Andrea E Schlather et al. "Near-field mediated plexcitonic coupling and giant Rabi splitting in individual metallic dimers". In: *Nano letters* 13.7 (2013), pp. 3281–3286.
- [43] Y Sugawara et al. "Strong coupling between localized plasmons and organic excitons in metal nanovoids". In: *Physical review letters* 97.26 (2006), p. 266808.
- [44] Sukosin Thongrattanasiri, Frank HL Koppens, and F Javier Garcia De Abajo. "Complete optical absorption in periodically patterned graphene". In: *Physical review letters* 108.4 (2012), p. 047401.
- [45] Hiroyoshi Tsuyuki, Shoichi Sakamoto, and Mitsuyoshi Tomiya. "Electron Transfer on Impurity doped Graphene Nanoribbon". In: *Journal of Physics: Conference Series*. Vol. 402. 1. IOP Publishing. 2012, p. 012016.
- [46] Archana Venugopal et al. "Effective mobility of single-layer graphene transistors as a function of channel dimensions". In: *Journal of Applied Physics* 109.10 (2011), p. 104511.
- [47] Feng Wang et al. "Gate-variable optical transitions in graphene". In: *science* 320.5873 (2008), pp. 206–209.
- [48] Feng Wang et al. "Gate-variable optical transitions in graphene". In: *science* 320.5873 (2008), pp. 206–209.
- [49] L Wang et al. "One-dimensional electrical contact to a two-dimensional material". In: *Science* 342.6158 (2013), pp. 614–617.
- [50] Fengnian Xia et al. "Ultrafast graphene photodetector". In: *Nature nanotechnology* 4.12 (2009), p. 839.
- [51] Xiaodong Xu et al. "Photo-Thermoelectric Effect at a Graphene Interface Junction". In: *Nano Letters* 10.2 (2010). PMID: 20038087, pp. 562–566. DOI: 10.1021/nl903451y. eprint: <https://doi.org/10.1021/nl903451y>.
- [52] Hugen Yan et al. "Damping pathways of mid-infrared plasmons in graphene nanostructures". In: *Nature Photonics* 7.5 (2013), p. 394.
- [53] Hugen Yan et al. "Tunable infrared plasmonic devices using graphene/insulator stacks". In: *Nature nanotechnology* 7.5 (2012), p. 330.
- [54] Yu Yao et al. "Broad electrical tuning of graphene-loaded plasmonic antennas". In: *Nano letters* 13.3 (2013), pp. 1257–1264.
- [55] Yu Yao et al. "Wide wavelength tuning of optical antennas on graphene with nanosecond response time". In: *Nano letters* 14.1 (2013), pp. 214–219.

- [56] Xiaolong Zhu et al. “Enhanced light-matter interactions in graphene-covered gold nanovoid arrays”. In: *Nano letters* 13.10 (2013), pp. 4690–4696.

## NON-EQUILIBRIUM GRAPHENE PLASMONS AND GAIN

In this chapter, we discuss non-equilibrium graphene plasmons excitations originating from a hot carrier distribution created by ultrafast optical pumping. Plasmon emission is a decay path of photoexcited carriers in graphene that has been theoretically proposed, but remained elusive experimentally. We present a theoretical model [17] and resulting predictions for plasmon emission as an ultrafast and ultrabright light emitting mechanism.

### **3.1 Carrier dynamics in graphene upon ultrafast optical excitation**

Carrier relaxation in graphene is now understood to occur via several stages and decay channels. The promptly excited carriers with a non-Fermi-like distribution undergo carrier-carrier and carrier-plasmon scatterings on a 10-fs time scale, followed by Auger recombination and optical phonon emission. Excited carriers eventually reach a complete equilibrium with the lattice and environment through direct or disorder-assisted acoustic phonon emission, which occur on a picosecond timescale. These carrier relaxation processes in graphene upon optical pumping are depicted in Fig. 3.1 [4, 6, 10, 13, 26]. Several theoretical studies have proposed that plasmon emission is another competing decay channel [7, 24]. Previous studies have predicted and revealed the strong interplay of plasmons and particle/hole excitations in graphene, which plays a significant role in reducing the lifetime of photoexcited charge carrier [3, 8, 9, 18]. Experimental evidence for optically generated non-equilibrium plasmons

was provided by near-field microscopy measurements, where an increase in the Drude weight and the form of the resultant dispersion relations were consistent with graphene plasmons at an elevated carrier temperature upon ultrafast optical excitation [15, 27]. Optical control of graphene plasmons allows excitation and modulation of graphene plasmons on ultrafast time scales.

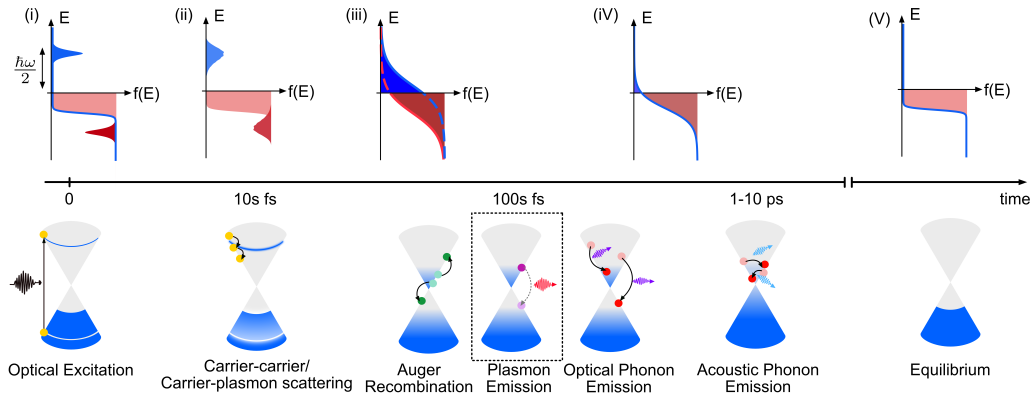


Figure 3.1: Carrier relaxation processes in graphene under ultrafast optical excitation: (i) Sharply peaked distribution of photoexcited carriers upon optical pumping. (ii) Carriers with a non-Fermi-like distribution undergoing carrier-carrier scattering on a 10-fs time scale. (iii) Carriers in a quasi-equilibrium state. (iv) Carriers that have been thermalized under interband processes, but are still hotter than the lattice. (v) Complete equilibrium between the carriers and the lattice.

The ability to achieve inversion and plasmon gain is of fundamental interest, and is also interesting owing to the potential for a coherent amplification or lasing medium from the infrared to THz spectral region [14, 19–21]. A coherent terahertz radiation was observed due to the parametric amplification of Josephson plasma waves in layered superconductors [22]. It has been theoretically predicted that graphene plasmons can experience gain via stimulated plasmon emission in photoinverted graphene at excitation levels achievable via optical, electrical, or diffusion pumping [5, 16, 17, 23]. The only experimental evidence for graphene plasmon gain, to best of our knowledge, was provided by

polarization-dependent THz radiation, whose value exceeding the spontaneous emission limit was qualitatively attributed to plasmon gain [28].

### 3.2 Non-equilibrium plasmon dispersion relation calculations

Previous theoretical work showed that photoexcited carriers can create conditions for gain in non-equilibrium plasmon population via stimulated and spontaneous plasmon emission processes [7, 16, 17]. The plasmon emission/absorption rates can be calculated using Fermi's golden rule (FGR). According to FGR, the plasmon emission rate takes the following semi-analytical equation under the first-order approximation (first-order approximation is accurate as long as the loss/gain rates are much lower than the plasmon frequency):

$$g \approx \alpha_f c k \frac{\theta(\omega - v_F k)}{\sqrt{\omega^2 - (v_F k)^2}} \frac{2K(\omega, k)}{\frac{\partial \text{Re}(\epsilon(\omega, k))}{\partial \omega}} \Big|_{\omega=\omega_p(k)} \quad (3.1)$$

$$K(\omega, k) = \int_{-1}^{+1} du \sqrt{1 - u^2} f \left( \frac{\hbar(\omega + v_F k u)}{2} \right) \Big|_{\mu_c}^T \times f \left( \frac{\hbar(\omega - v_F k u)}{2} \right) \Big|_{\mu_v}^T \quad (3.2)$$

where  $\alpha_f$  is the fine-structure constant,  $v_F$  is the graphene Fermi velocity, and  $K(\omega, k)$  is a measure for the phase space available for emission processes. As seen in Eq. (3.1), the emission/absorption rates critically depend on the exactness of the plasmon dispersion relations [17]. In order to accurately describe plasmons in photoinverted graphene, the complex plasmon frequency dispersion needs to be solved exactly in contrast to making the low loss approximation under which the plasmon frequency is considered as a real variable and the decay rate is solved perturbatively. We calculate the complex graphene plasmon dispersion relation,  $\omega(k) = \omega_p(k) + i\gamma_p(k)$ , by setting the dynamic dielectric

function of graphene,  $\epsilon(\omega, k)$ , to zero ( $\omega_p$  is the plasmon energy for a given  $k$ , and  $\gamma_p$  is the plasmon decay rate, where  $\gamma_p > 0$  means net plasmon generation and  $\gamma_p < 0$  means net plasmon loss) [16, 17].

The dielectric function,  $\epsilon(\omega, k)$ , can be expressed within the random phase approximation as Eq. (3.3).

$$\epsilon(\omega, k) = 1 - \frac{e^2}{2\epsilon_0\epsilon_{\text{eff}}k} \Pi_{\text{final}}(\omega_p + i\gamma_p, k) \quad (3.3)$$

where  $\epsilon_{\text{eff}}$  is the average dielectric function of the air-substrate interface defined as  $\epsilon_{\text{eff}} = \frac{\epsilon_{\text{air}} + \epsilon_{\text{substrate}}}{2}$ , and  $\Pi_{\text{final}}(\omega, k)$  is the graphene dynamical polarizability.

The graphene polarizability,  $\Pi$ , of an arbitrary non-equilibrium carrier distribution that is well-defined on the complex frequency plane is reported in Ref. [17].

The polarizability for the two-component plasma system with finite temperatures can be represented as the sum of the zero-temperature quasi-equilibrium polarizability and the correction terms that account for smearing of the Fermi edge due to finite temperatures as Eq. (3.4).

$$\Pi_{\text{final}} = \Pi(\omega, k) \Big|_{\text{quasi-eq}}^{T=0} + \int_0^\infty dE \left[ \frac{\partial \Pi|_{\mu=E}^{T=0}}{\partial E} (\delta f|_{\mu_c}^T) + \frac{\partial \Pi|_{\mu=E}^{T=0}}{\partial E} (\delta f|_{\mu_v}^T) \right] \quad (3.4)$$

where  $\Pi_{\text{quasi-eq}}^{T=0}$  is the zero-temperature quasi-equilibrium polarizability,  $\mu_c$  and  $\mu_v$  are the chemical potentials for conduction and valence bands, respectively,  $T$  is the shared temperature of the two-component plasma, and  $\delta f = f(E)_\mu^T - f(E)_\mu^{T=0}$ , where  $f(E) = \frac{1}{e^{(E-\mu)/k_B T} + 1}$ . In our case,  $\mu_c$  and  $\mu_v$  are not necessary equal because the equilibrium carrier density of the graphene sample

is externally controlled via electrostatic gating. The zero-temperature quasi-equilibrium polarizability is defined as Eq. (3.5).

$$\Pi(\omega, k)|_{\text{quasi-eq}}^{T=0} = \Pi(\omega, k)|_{\mu_c}^{T=0} + \Pi(\omega, k)|_{\mu_v}^{T=0} - \Pi(\omega, k)|_{\mu=0}^{T=0} \quad (3.5)$$

The finite-temperature correction terms in Eq. (S12) accounts for the Fermi edge smearing as quantified by  $\delta f(E)|_{\mu}^T$ , and the evaluation of the integrand of Eq. (S12) requires the derivative of  $\Pi_{\mu}^{T=0}$ , which can be written as Eq. (3.6).

$$\begin{aligned} \Pi'(\omega, k) &= \frac{\partial \Pi_+}{\partial \mu} + \frac{\partial \Pi_-}{\partial \mu} \\ &= \frac{g}{8\pi\hbar^2 v_F^2} \left[ \frac{-2\sqrt{\mu-u}\sqrt{\mu-v} + 2\mu}{\sqrt{u}\sqrt{v}} - 2 \right] + \frac{g}{8\pi\hbar^2 v_F^2} \left[ \frac{-2i\sqrt{i(\mu+u)}\sqrt{i(\mu+v)} - 2\mu}{\sqrt{u}\sqrt{v}} - 2 \right] \end{aligned} \quad (3.6)$$

where  $u = \frac{\omega+k}{2}$  and  $v = \frac{\omega-k}{2}$ . When solving for the complex-frequency dispersion, it needs to be ensured that the solved dispersion curve does not cross a branch cut and remains continuous and physically meaningful. The details about relevant branch points/cuts and integration path are further explained in Ref. [16].

Upon ultrafast optical excitation, carriers quickly thermalize among themselves via carrier-carrier scattering, and the system establishes a quasi-equilibrium state on a sub-100-fs timescale. Because the carrier-carrier scattering is typically one to two orders of magnitude faster than the interband recombination processes, in a quasi-equilibrium state, the carriers form the two-component plasma by having separate Fermi-Dirac distributions within their bands with their own chemical potential, but the shared temperature, as shown in stage

(iii) of Fig. 3.1. The theoretical formalism developed to calculate complex-frequency graphene non-equilibrium plasmon dispersion relations is applicable to any arbitrary, non-Fermi-like carrier distributions Eq. (3.4) [17]. Page et al. have shown that excited carriers need to relax within their band before they contribute to plasmon gain processes [17]. It was shown that the loss of the plasmon dispersion, in fact, increases with increasing excitation fluence immediately after photoexcitation as there are not enough emission channels at any particular energy to compete with absorption and have a net gain before these photoexcited carriers relax within the band.

Thus, we apply the studied formalism to the photoinverted graphene in a quasi-equilibrium state. As shown in Eq. (3.4), the non-equilibrium complex- $\omega$  graphene plasmon dispersions are defined with three parameters:  $T$ ,  $\mu_c$ , and  $\mu_v$ . As the photoexcited carriers relax towards equilibrium, these three parameters also evolve with time. we take phenomenological approaches to estimate these parameters. For a given excitation fluence of a sub-100fs laser pulse, the values of  $T$ ,  $\mu_c$ , and  $\mu_v$  at the time the system has just reached a quasi-equilibrium can be obtained by solving for the following two equation simultaneously:

$$N = N_p + N_0 = \int f(E, \mu, T_e) D(E) dE \quad (3.7)$$

$$U = U_p + U_0 = \int E f(E, \mu, T_e) D(E) dE \quad (3.8)$$

The quantities,  $N_0$  and  $N_p$ , are the initial gate-controlled and photoexcited carrier densities, respectively. The quantities,  $U_0$  and  $U_p$ , are the initial energy density and the energy density deposited by optical excitation, respectively.

The photoexcited carrier density,  $N_p$ , is approximated as  $N_p \approx \frac{U_p}{\hbar\omega_0}$ , where  $U_p$  corresponds to the pump fluence,  $\omega_0$  is the laser frequency,  $D(E)$  is the electron density of states in graphene, and  $f(E, \mu, T_e) = \frac{1}{e^{(E-\mu)/k_B T_e} + 1}$ .

The temporal evolution of the carrier temperature as the carriers relax from a quasi-equilibrium state to a complete equilibrium state is described with a phenomenological two-temperature (2T) model. The model solves for the temporal evolutions of electronic and phononic temperatures. A 2T model for graphene was adopted from that used in Ref.[12]. It is assumed the optical excitation energy goes to the electronic system, and the energy is transferred to the phononic system through a electron-phonon coupling rate. In this phenomenological approach, it is often assumed that photoexcited electrons equilibrate with a particular branch of optical phonons, referred as strongly coupled optical phonons (SCOPs), with an exceptionally higher electron-phonon coupling rate, essentially leaving electrons decoupled from other phonons [25]. The SCOP bath eventually achieve equilibrium with the rest of the phonons, whose temperature stays approximately at ambient temperature,  $T_0$ , on a picosecond timescale. The electron and SCOP temperatures of graphene,  $T_e$  and  $T_p$ , can then be obtained by solving the following coupled equations:

$$\frac{\partial T_e}{\partial t} = \frac{I(t)}{\beta} - \frac{\Gamma_{e-p}}{C_e} \quad (3.9)$$

$$\frac{\partial T_p}{\partial t} = \frac{\Gamma_{e-p}}{C_p} - \frac{T_p - T_0}{\tau_p} \quad (3.10)$$

where  $I(t)$  is the power density of the incident ultrafast pulse,  $\Gamma_{e-p}$  is the electron-phonon energy exchange rate [1, 11],  $C_e$  and  $C_p$  are the electronic

and phonon specific heats, and  $\tau_p$  is the lifetime of the SCOPs. The temporal profile of the excitation optical pulse is modeled as  $I(t) = \frac{A_{\text{gra}}F}{2\tau_{\text{pulse}}}\text{sech}^2\left(\frac{t}{\tau_{\text{pulse}}}\right)$ , where  $A_{\text{gra}}$  is the absorption in graphene at the wavelength of the incident laser light,  $\tau_{\text{pulse}}$  is the laser pulse duration, and  $F$  is the laser fluence. The electronic specific heat is analytically determined from the linear electronic band structure as  $C_e(T_e) = \frac{18\xi(3)k_B^3T_e^2}{\pi(\hbar v_F)^2}$ , where  $v_F$  is the Fermi velocity of graphene. The specific heat of the SCOPs,  $C_p$ , and the electron-SCOP exchange rate,  $\Gamma_{e-p}$ , are expressed in Ref. [12].  $\tau_p$  is approximated as 1.5 ps [12, 25]. When the system is far out of equilibrium, the temperature of the system, and thus the specific heat, are not well defined. Thus, the power density of the incident ultrafast pulse,  $I(t)$ , is scaled by a parameter,  $\beta$ , which has the same units as specific heat ( $\text{eVm}^{-2}\text{K}^{-1}$ ) [11]. The parameter  $\beta$  determines the initial maximum electronic temperature, which is determined by solving Eq. (3.7) and Eq. (3.8) simultaneously for a given laser fluence.

Figure 3.2 shows the temperature profiles of electrons and SCOPs of graphene for a given laser fluence of  $1.12 \text{ J m}^{-1}$  with varying initial gate-controlled graphene Fermi levels. The grey shaded region in Fig. 3.2 is when the system does not have a well-defined temperature as carriers have not yet reached a quasi-equilibrium state; this region is equivalent to stage (ii) in Fig. 3.1. We note that the temperature profiles in graphene are gate-dependent; as the initial Fermi level varied closer to the charge neutral point (CNP), the maximum electronic temperature increases.

The time evolution of the chemical potentials is described phenomenologically based on the rate equation studies, solving for the relaxation dynamics

of for an inverted massless Dirac fermion plasma in interaction with bosonic reservoirs via emission and absorption processes [7]. Specifically, the effects of plasmon and phonon emission processes on the rate of the inversion depletion were studied. The temporal evolution of chemical potential can be phenomenologically fitted with three exponential functions with characteristic times:  $\mu(t) = \mu_0 \sum_{i=1}^3 A_i e^{-t/\tau_i}$ . The initial chemical potential is determined from Eqs. 3.7 and 3.8, and  $\mu$  returns to the equilibrium gate-controlled chemical potential.

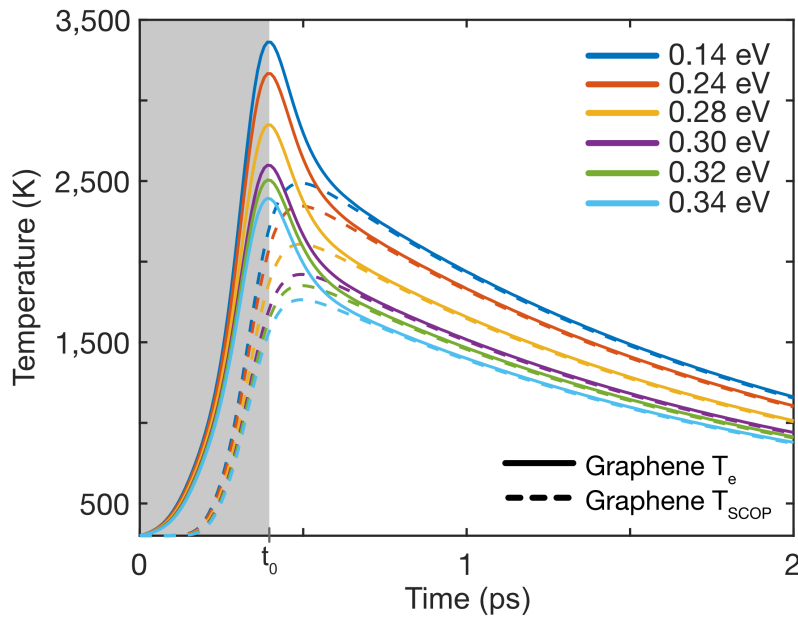


Figure 3.2: Gate-dependent temperature profiles of graphene for a given laser fluence of  $1.12 \text{ J m}^{-2}$ .

### 3.3 Graphene Fermi level and time dependence

We consider a planar graphene sample on an underlying substrate of a  $1\text{-}\mu\text{m}$ -thick  $\text{SiN}_x$  and a  $50\text{-nm}$ -thick ITO, which can serve as a backgate. The solved complex-frequency plasmon dispersion relations for varying gate-controlled graphene Fermi levels for a given laser fluence of  $1.12 \text{ J m}^{-2}$  are shown in Fig. 3.3. These

calculations are the snapshots of the graphene dispersion relations when the carriers have just established a quasi-equilibrium state (equivalent to the end of the grey shaded area in Fig. 3.2). When the imaginary part of the plasmon frequency,  $\gamma_p$ , is positive (negative), by definition, plasmons experience gain (loss) via net stimulated emission (absorption). As the emission rate scales with  $\gamma_p$ , the calculations suggest that plasmon emission is enhanced with increasing hole doping of graphene. The increase in emission with increased hole doping of graphene can be intuitively understood as a result of enlarging the phase space for the excited carriers to relax by emitting plasmons. For plasmon emission being an interband process, having control over graphene Fermi level via electrostatic gating can greatly enhance observation of plasmon emissions, as hole-doping of graphene not only enlarges phase space for plasmon emission but also raises the (Pauli-blocking) barrier for plasmon absorption. Figure 3.4 shows the time-dependent calculated plasmon dispersion relations for a given gate-controlled graphene Fermi level of 0.34 eV and a laser fluence of  $1.12 \text{ J m}^{-2}$ . The time-dependent calculations show that the spectral range that allows net plasmon emission diminishes as the population inversion in graphene depletes over time.

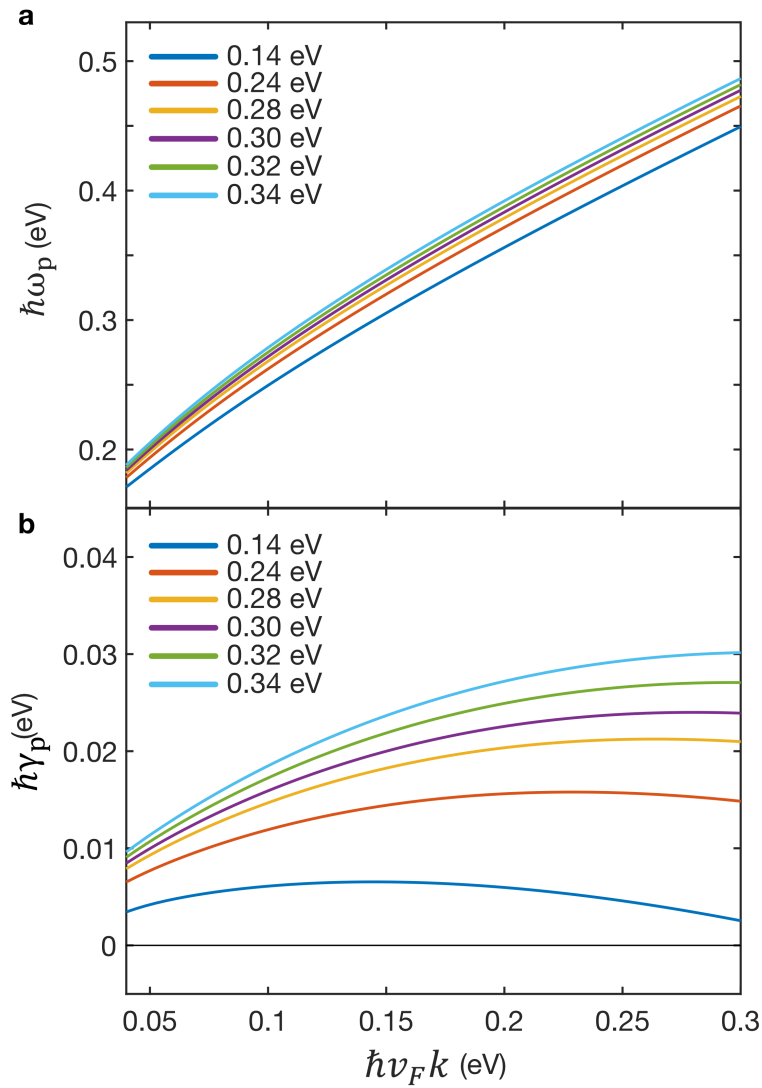


Figure 3.3: Non-equilibrium plasmon dispersions for graphene on top of  $\text{SiN}_x$  for a given laser fluence of  $1.12 \text{ J m}^{-2}$  (the pulse width was assumed to be 100 fs). (a) The real part and (b) imaginary part of plasmon complex frequency dispersion for different gate-controlled initial graphene Fermi levels at time when the quasi-equilibrium has just been established.

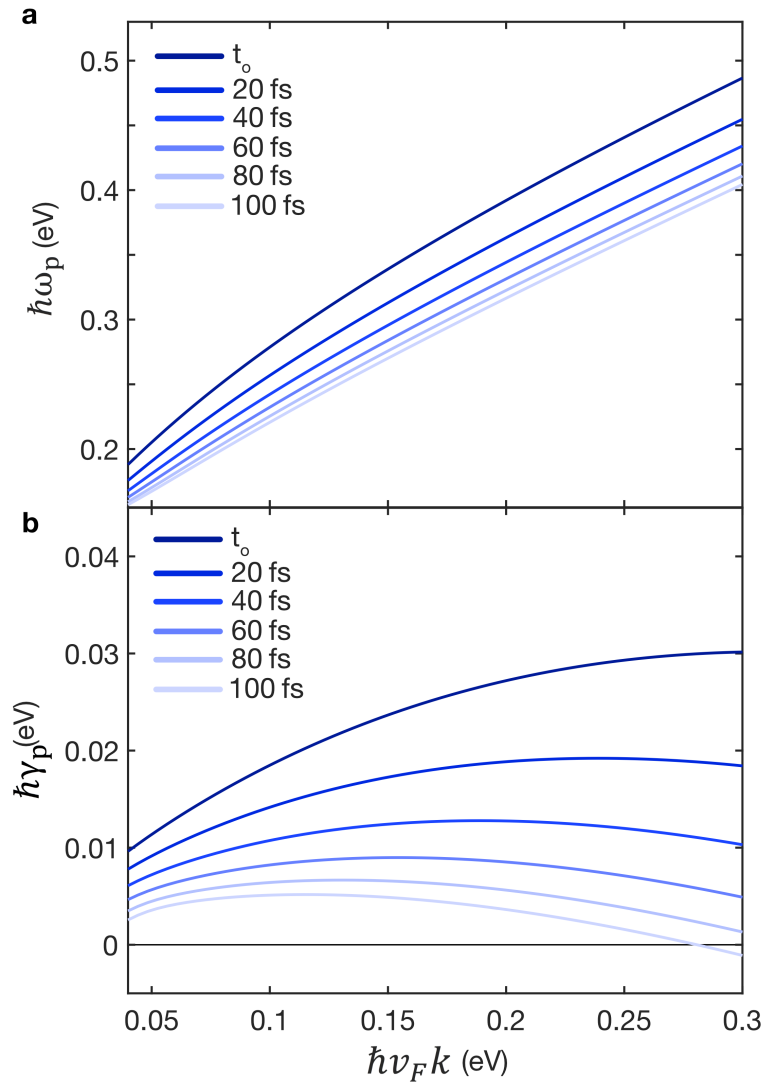


Figure 3.4: Non-equilibrium plasmon dispersions for graphene on top of  $\text{SiN}_x$ . (a) The real part and (b) imaginary part of plasmon complex frequency for a given initial graphene Fermi level of 0.34 eV as time progresses since the quasi-equilibrium has established. The laser fluence of  $1.12 \text{ J m}^{-2}$ , and the pulse width of 100 fs are assumed.

### 3.4 Collision loss dependence

We also study the effects of collision losses. A collision time,  $\tau$ , accounts for plasmon lifetime due to collisions with impurities, acoustic phonons and optical phonons. It varies from tens to hundreds of femtoseconds depending on the quality of graphene and the underlying substrate. To include  $\tau$ , the following transformation was performed on the graphene polarizability  $\Pi(\omega, k)$ :

$$\Pi_\tau = \frac{(\omega + i\tau^{-1})\Pi(\omega + i\tau^{-1}, k)}{\omega + \frac{i\tau^{-1}\Pi(\omega + i\tau^{-1}, k)}{\Pi_1(0, k)}} \quad (3.11)$$

Figure 3.5 shows the calculated  $\tau$ -dependent graphene plasmon dispersion relations for a given laser fluence of  $1.12 \text{ J m}^{-2}$  and a gate-controlled graphene Fermi level of  $0.34 \text{ eV}$  at time  $t_0$ , which denotes the time at which the system has reached a quasi-equilibrium state. The scattering time,  $\tau$ , has no significant impact on the real part of the plasmon frequency, while increasing the collision loss rate diminishes the imaginary part of the plasmon frequency,  $\gamma_p$ , suggesting decreasing net plasmon emission as additional absorption channels are introduced. The spontaneous emission spectra were calculated by scaling the plasmon emission rates by the plasmon density of states,  $G = gD_p$ , where  $D_p = \frac{k(\omega)}{2\pi} \frac{dk(\omega)}{d\omega}$ , assuming that the generated plasmons emit incoherently into all possible modes. As suggested by Eq. (3.1), the collision loss time,  $\tau$ , does not explicitly enter the emission rate equation, and also it affects only weakly the plasmon dispersion relations [17]. Thus, as shown in Fig. 3.6, the calculated plasmon emission spectra show weak dependence on the collision loss rate.

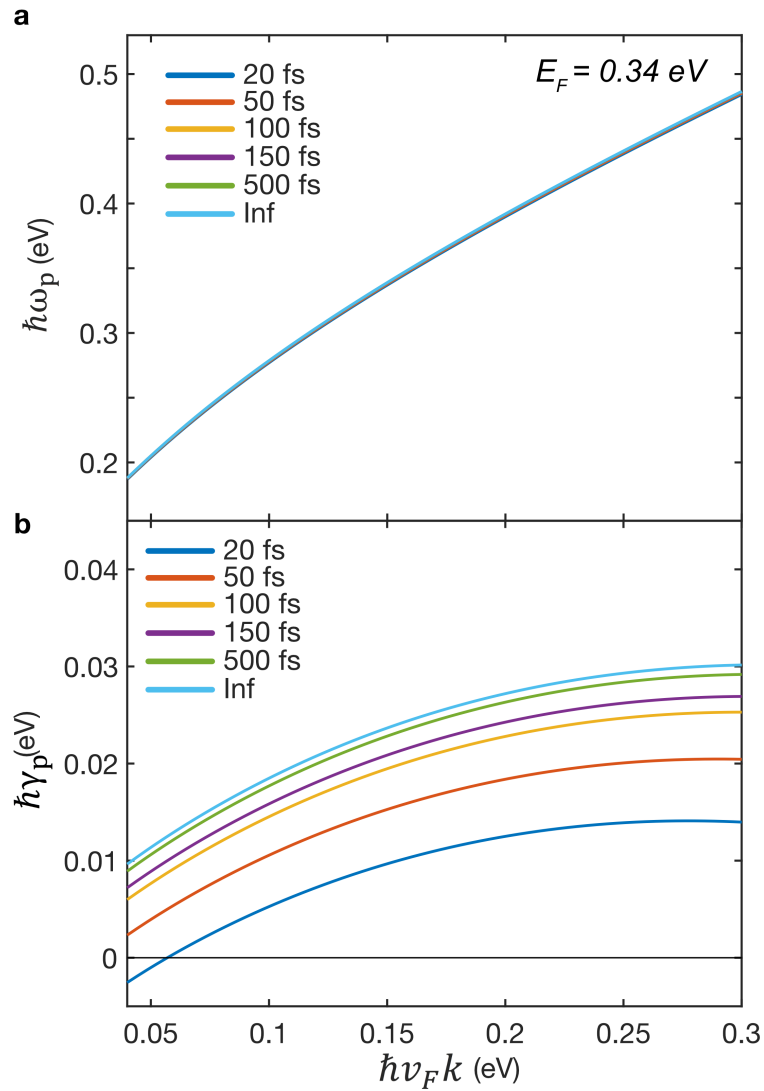


Figure 3.5: The effects of collision loss time,  $\tau$ . (a) The real and (b) imaginary part of plasmon dispersion relation at the time the system has reached a quasi-equilibrium for a given gate-controlled graphene Fermi level of 0.34 eV. The laser fluence of  $1.12 \text{ J m}^{-2}$  and the pulse width of 100 fs were assumed.

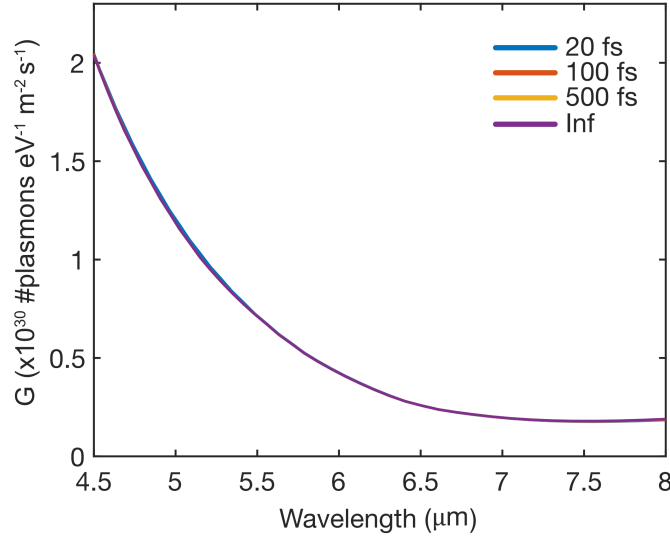


Figure 3.6: Plasmon emission spectra with varying collision time,  $\tau$ , calculated based on the solved graphene plasmon relations shown in Fig. 3.5. The gate-controlled graphene Fermi level was fixed at 0.34 eV.

### 3.5 Effects of underlying substrate

The dielectric function of graphene and thus the resulting plasmon behavior are highly dependent on and sensitive to its surrounding. We show that plasmon generation can be heavily damped due to the phonons of an underlying substrate. In this work, a  $\text{SiN}_x$  membrane was used as a substrate. As shown in Fig. 3.7, the imaginary part of the substrate permittivity starts to rise at wavelength  $>8 \mu\text{m}$  due to the substrate phonons. The complex- $k$  plasmon dispersion relations were calculated for a given carrier temperature of 2,000 K and collision loss time of 50 fs (Fig. 3.8(a)). In addition, the plasmon loss was quantified by calculating the ratio of the imaginary and real parts of the wavevector (Fig. 3.8(b)). As the substrate phonon starts to provide a damping channel for graphene plasmons, the real part of the graphene plasmon propagation wavevector asymptotes to zero. As a result, the plasmon loss overshoots

for wavelength  $>8 \mu\text{m}$ . For this reason, no plasmon emission is expected in the spectral region of wavelengths  $>8 \mu\text{m}$  when graphene is placed on a  $\text{SiN}_x$  substrate.

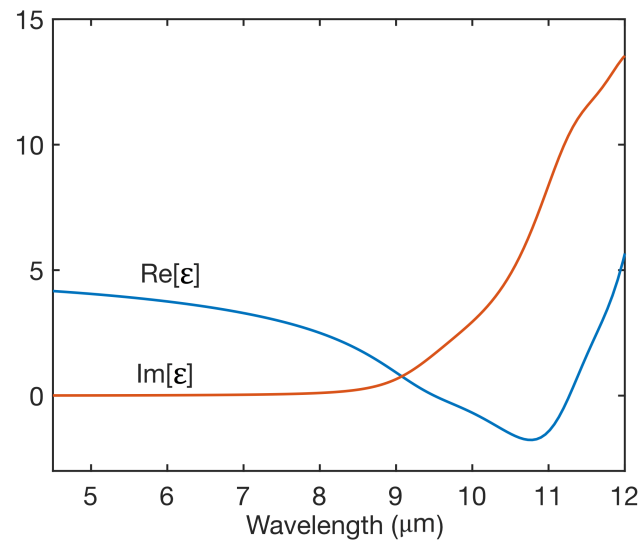


Figure 3.7: Real and imaginary parts of the relative permittivity of  $\text{SiN}_x$ .

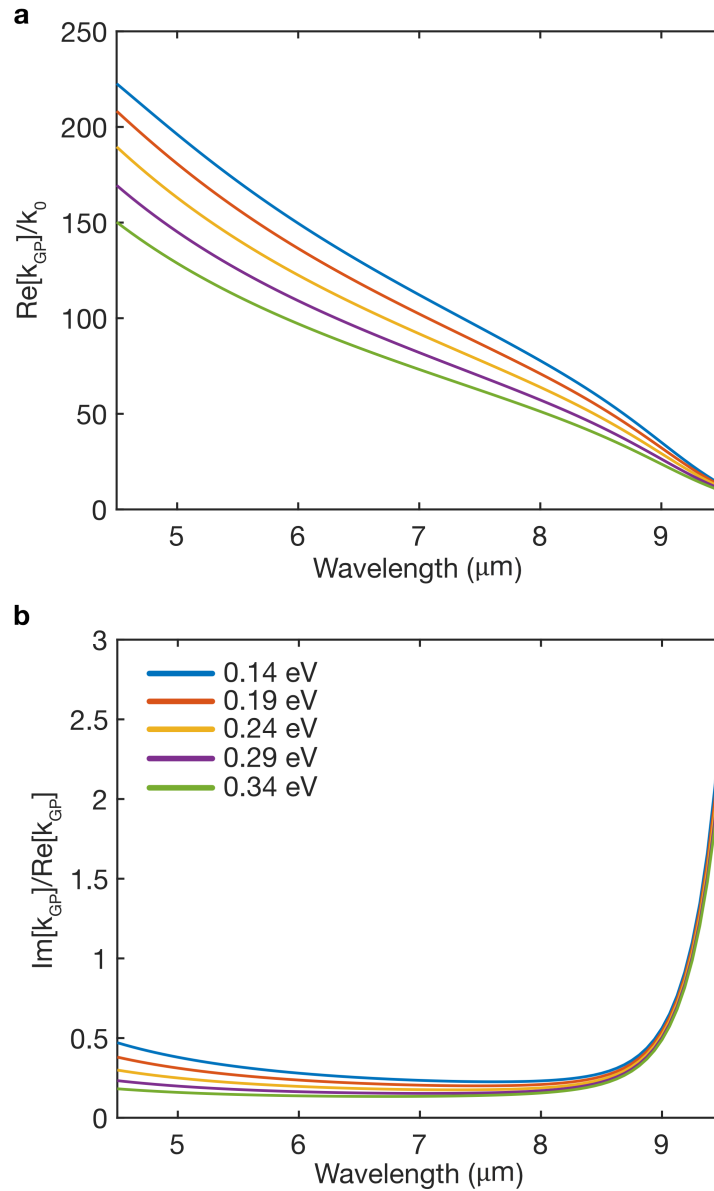


Figure 3.8: (a) Gate-dependent plasmon dispersion relation defined on a complex- $k$  plane for a given carrier temperature of 2,000 K and collision loss time of  $\tau = 50$  fs. (b) Plasmon loss quantified by the ratio of imaginary and real parts of graphene plasmon wavevector,  $k_{\text{GP}}$ .

### 3.6 The ratio of stimulated to spontaneous plasmon emission rates

There are three fundamental processes that contribute to the plasmon population in the system: stimulated emission, spontaneous emission and absorption (Fig. 3.9). The transition rate of an excited state of electron due to plasmon emission can be derived from Fermi's golden rule similarly to the photon emission rate assuming a two-level system in a vacuum. The plasmon emission rate is given by Eq. (3.12) [2, 24].

$$\gamma = \frac{2\pi}{\hbar} \sum_k \frac{\hbar\omega}{2\epsilon_0 S} |\mathbf{D}_{12} \cdot \mathbf{u}_{1,k}(z)|^2 (n_p + 1) \delta(E_2 - E_1 - \hbar\omega) \quad (3.12)$$

where  $\mathbf{D}_{12} = \langle 2 | \mathbf{D} | 1 \rangle$  is the matrix element of the dipole moment operator,  $\mathbf{D}$ ,  $|1\rangle$  and  $|2\rangle$  are the ground and excited states of the two-level system,  $\mathbf{u}_k(z)$  is the polarization vector of the quantum electric field operator, and  $n_p$  is the plasmon distribution function [2]. The  $n_p$  term in Eq. (3.12) accounts for the contribution from stimulated emission, and the constant term accounts for the contribution from spontaneous emission. The ratio of stimulated to spontaneous emission rates, therefore, is given by  $\gamma_{\text{stim}}/\gamma_{\text{spont}} = n_p$ . The time evolution of the plasmon distribution function,  $n_p$ , is obtained by solving the rate equation, given by Eq. (3.13), assuming that spontaneous emission, stimulated emission, absorption and collision loss are the processes changing the plasmon population [2].

$$\frac{dn_p}{dt} = \gamma_{\text{emiss}}(n_p + 1) - \gamma_{\text{abs}}n_p - \gamma_{\text{coll}}n_p \quad (3.13)$$

where  $\gamma_{\text{emiss}}$  and  $\gamma_{\text{abs}}$  are the plasmon emission and absorption rates, respectively, and  $\gamma_{\text{coll}}$  is the collision loss rate and assumed to be constant. The plasmon distribution function,  $n_p$ , was solved for various values of  $\gamma_{\text{coll}}^{-1}$  ranging from 10 fs to 100 fs. In first-order approximation, the plasmon interband

emission/absorption rate,  $\gamma_{\text{emiss/abs}}$ , can be approximated as Eq. (3.14) [7, 17].

$$\gamma_{\text{emiss/abs}} \approx \frac{\alpha_f c k \theta (\omega - v_F k)}{\sqrt{\omega^2 - (v_F k)^2}} \frac{2K_{\text{emiss/abs}}(\omega, k)}{\frac{\partial \text{Re}[\epsilon(\omega, k)]}{\partial \omega}} \Big|_{\omega=\omega_p} \quad (3.14)$$

$$K_{\text{emiss}}(\omega, k) = \int_{-1}^1 du \sqrt{1-u^2} f\left(\frac{\hbar\omega + \hbar v_F k u}{2}, \mu_c, T_e\right) f\left(\frac{\hbar\omega - \hbar v_F k u}{2}, \mu_v, T_e\right) \quad (3.15)$$

$$K_{\text{abs}}(\omega, k) = \int_{-1}^1 du \sqrt{1-u^2} \left(1 - f\left(\frac{\hbar\omega + \hbar v_F k u}{2}, \mu_c, T_e\right)\right) \left(1 - f\left(\frac{\hbar\omega - \hbar v_F k u}{2}, \mu_v, T_e\right)\right) \quad (3.16)$$

Figure 3.10 shows the calculated plasmonic distribution function as a function of time for a given initial graphene Fermi level of 0.34 eV at  $\lambda=6 \mu\text{m}$  for a given laser fluence of  $1.12 \text{ J m}^{-2}$ . When the plasmonic distribution function is greater than one (i.e., above the dotted line in Fig. 3.10), the stimulated emission dominates spontaneous emission. On a 100-fs timescale, stimulated emission dominates spontaneous emission when the collision time,  $\tau_{\text{coll}}$ , is sufficiently long. Once the inversion is depleted, absorption starts to deplete the plasmon population exponentially, and spontaneous emission starts to dominate stimulated emission. When the plasmon distribution function (i.e., ratio of the stimulated to spontaneous emission rates) is time-averaged up to  $t - t_0=250$  fs, stimulated emission is dominant over the frequency range between  $4.5 \mu\text{m}$  and  $6 \mu\text{m}$  as shown in Fig. 3.10(b). This opens path to coherent plasmon amplification on sub-100s fs time scale.

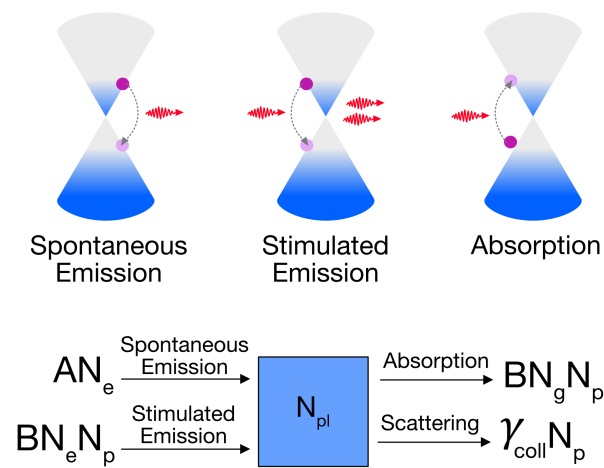


Figure 3.9: Three fundamental processes that contribute to the total number of plasmons in the system: spontaneous emission, stimulated emission, and absorption of plasmons.  $A$  and  $B$  are the spontaneous emission and stimulated emission/absorption Einstein coefficients, respectively.  $N_p$  is the plasmon density, and  $N_e$  and  $N_g$  are the carrier densities in the excited and ground states, respectively.  $\gamma_{coll}$  is the collision rate.

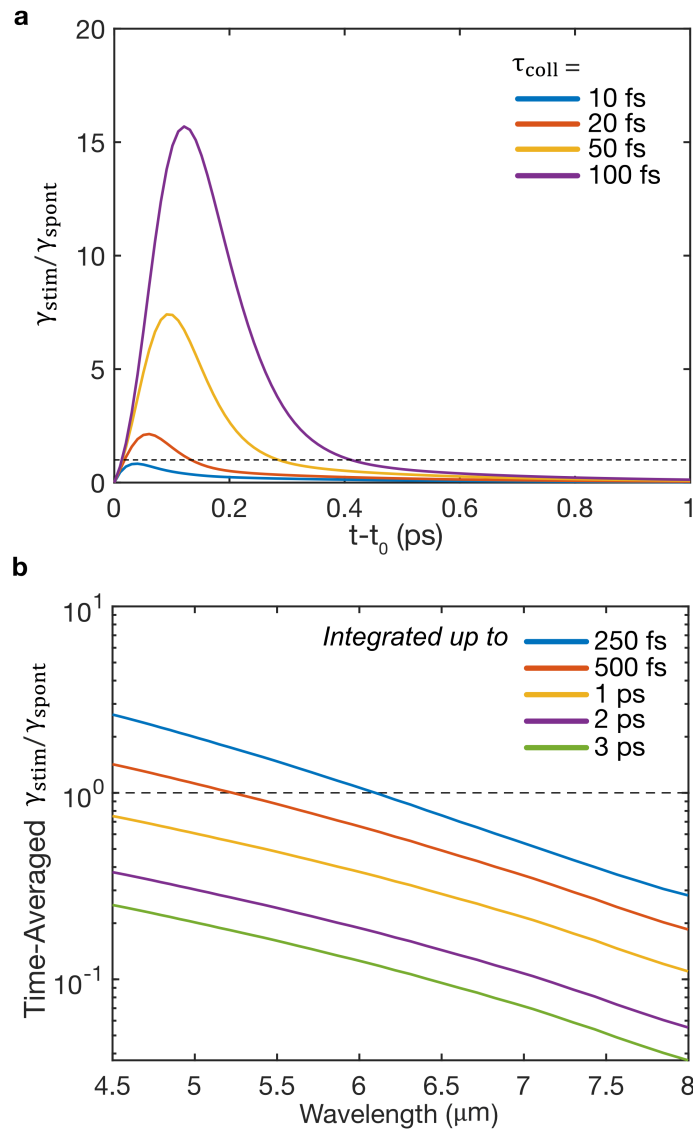


Figure 3.10: (a) The ratio of stimulated to spontaneous plasmon emission rates as a function of time at  $\lambda = 6 \mu\text{m}$  for a given initial graphene Fermi level of 0.34 eV. The laser fluence of  $1.12 \text{ J m}^{-2}$  and the pulse width of 100 fs are assumed.  $t_0$  represents the time at which the system has just reached quasi-equilibrium. (b) The time-averaged ratio for a given initial graphene Fermi level of 0.34 eV and  $\gamma_{\text{coll}}^{-1} = 20$  fs as a function of wavelength when the ratio is integrated up to  $t - t_0 = 250$  fs, 500 fs, 1 ps, 2 ps, and 3 ps.

## References

- [1] M Zahirul Alam, Israel De Leon, and Robert W Boyd. “Large optical nonlinearity of indium tin oxide in its epsilon-near-zero region”. In: *Science* 352.6287 (2016), pp. 795–797.
- [2] Alexandre Archambault et al. “Quantum theory of spontaneous and stimulated emission of surface plasmons”. In: *Physical Review B* 82.3 (2010), p. 035411.
- [3] Aaron Bostwick et al. “Quasiparticle dynamics in graphene”. In: *Nature physics* 3.1 (2007), p. 36.
- [4] M Breusing et al. “Ultrafast nonequilibrium carrier dynamics in a single graphene layer”. In: *Physical Review B* 83.15 (2011), p. 153410.
- [5] AA Dubinov et al. “Terahertz surface plasmons in optically pumped graphene structures”. In: *Journal of Physics: Condensed Matter* 23.14 (2011), p. 145302.
- [6] Isabella Gierz et al. “Snapshots of non-equilibrium Dirac carrier distributions in graphene”. In: *Nature materials* 12.12 (2013), p. 1119.
- [7] Joachim M Hamm et al. “Nonequilibrium plasmon emission drives ultrafast carrier relaxation dynamics in photoexcited graphene”. In: *Physical Review B* 93.4 (2016), p. 041408.
- [8] EH Hwang, Ben Yu-Kuang Hu, and S Das Sarma. “Inelastic carrier lifetime in graphene”. In: *Physical Review B* 76.11 (2007), p. 115434.
- [9] EH Hwang and S Das Sarma. “Quasiparticle spectral function in doped graphene: Electron-electron interaction effects in ARPES”. In: *Physical Review B* 77.8 (2008), p. 081412.
- [10] S. A. Jensen et al. “Competing Ultrafast Energy Relaxation Pathways in Photoexcited Graphene”. In: *Nano Letters* 14.10 (2014). PMID: 25247639, pp. 5839–5845. DOI: 10.1021/nl1502740g. eprint: <https://doi.org/10.1021/nl1502740g>.
- [11] Jens Christian Johannsen et al. “Direct view of hot carrier dynamics in graphene”. In: *Physical Review Letters* 111.2 (2013), p. 027403.
- [12] Chun Hung Lui et al. “Ultrafast photoluminescence from graphene”. In: *Physical review letters* 105.12 (2010), p. 127404.
- [13] Leandro M Malard et al. “Observation of intra- and inter-band transitions in the transient optical response of graphene”. In: *New Journal of Physics* 15.1 (2013), p. 015009.

- [14] M Yu Morozov, IM Moiseenko, and VV Popov. "Giant amplification of terahertz plasmons in a double-layer graphene". In: *Journal of Physics: Condensed Matter* 30.8 (2018), 08LT02.
- [15] G. X. Ni et al. "Ultrafast optical switching of infrared plasmon polaritons in high-mobility graphene". In: *Nat. Photonics* 10.4 (2016), pp. 244–247. DOI: 10.1038/nphoton.2016.45.
- [16] A Freddie Page, Joachim M Hamm, and Ortwin Hess. "Polarization and plasmons in hot photoexcited graphene". In: *Physical Review B* 97.4 (2018), p. 045428.
- [17] A Freddie Page et al. "Nonequilibrium plasmons with gain in graphene". In: *Physical Review B* 91.7 (2015), p. 075404.
- [18] Marco Polini et al. "Plasmons and the spectral function of graphene". In: *Physical Review B* 77.8 (2008), p. 081411.
- [19] Olga V Polischuk et al. "Plasmonic amplification of terahertz radiation in a periodic graphene structure with the carrier injection". In: *Applied Physics Letters* 111.8 (2017), p. 081110.
- [20] VV Popov et al. "Amplification and lasing of terahertz radiation by plasmons in graphene with a planar distributed Bragg resonator". In: *Journal of Optics* 15.11 (2013), p. 114009.
- [21] VV Popov et al. "Plasmonic terahertz lasing in an array of graphene nanocavities". In: *Physical review B* 86.19 (2012), p. 195437.
- [22] Srivats Rajasekaran et al. "Parametric amplification of a superconducting plasma wave". In: *Nature physics* 12.11 (2016), p. 1012.
- [23] Farhan Rana. "Graphene terahertz plasmon oscillators". In: *IEEE Transactions on Nanotechnology* 7.1 (2008), pp. 91–99.
- [24] Farhan Rana et al. "Ultrafast carrier recombination and generation rates for plasmon emission and absorption in graphene". In: *Physical Review B* 84.4 (2011), p. 045437.
- [25] Daohua Song et al. "Direct measurement of the lifetime of optical phonons in single-walled carbon nanotubes". In: *Physical review letters* 100.22 (2008), p. 225503.
- [26] BY Sun, Y Zhou, and MW Wu. "Dynamics of photoexcited carriers in graphene". In: *Physical Review B* 85.12 (2012), p. 125413.
- [27] Martin Wagner et al. "Ultrafast and nanoscale plasmonic phenomena in exfoliated graphene revealed by infrared pump-probe nanoscopy". In: *Nano Lett.* 14.2 (2014), pp. 894–900. DOI: 10.1021/nl4042577.

- [28] Takayuki Watanabe et al. "The gain enhancement effect of surface plasmon polaritons on terahertz stimulated emission in optically pumped monolayer graphene". In: *New Journal of Physics* 15.7 (2013), p. 075003.

*Chapter 4*OBSERVATION OF GRAPHENE PLASMON-COUPLED  
NON-PLANCKIAN RADIATION

In this chapter, we report experimental demonstration of laser-pumped mid-infrared radiative emission from graphene, originating from bright hot plasmons emitted via decay of excited carriers. The experimental observations are consistent with the previously discussed theoretical prediction for graphene plasmon emission.

**4.1 Experimental Setup**

Our experimental configuration is shown in Fig. 4.1. A planar graphene sample is illuminated with sub-100-fs pulses from a Ti:Sapphire laser operating at a wavelength of 850 nm while the Fermi level of graphene is externally controlled via electrostatic gating. The laser is focused onto the graphene surface from the backside. The resulting infrared emission is collected with a 15× Cassegrain objective and sent to a Fourier-transform infrared (FTIR) spectroscopy. The spot size of the laser was expanded to ensure uniform illumination over the collection area of  $50\ \mu\text{m} \times 50\ \mu\text{m}$  enclosed by an aperture. All of the emission measurements are done under dry air purge. Laser pulses arrive periodically at the sample approximately every 12 ns (i.e., laser repetition rate of 80 MHz), while the moving mirror of the FTIR moves on a millisecond time scale. Thus, the repetition rate of the laser is sufficiently high that a large number of pulse-induced radiation events are integrated in each acquired spectrum. A black soot sample is used as an emissivity reference, and the collected emission spec-

tra are calibrated assuming unity emissivity for the black soot reference at all wavelengths.

The sample consists of a CVD-grown monolayer graphene layer on a 1- $\mu\text{m}$ -thick  $\text{SiN}_x$  and a 50-nm-thick ITO, which serves as a backgate. A 50-nm-thick ITO film was deposited on the bottom side of a 1- $\mu\text{m}$ -thick  $\text{SiN}_x$  membrane (Norcada, NX10500F) by RF sputtering with the flow rate of  $\text{Ar}+\text{O}_2$  of 0.4 sccm at a pressure of 3 mTorr at a power of 48 W. A CVD-grown monolayer graphene was transferred onto the top side of the  $\text{SiN}_x$  membrane.

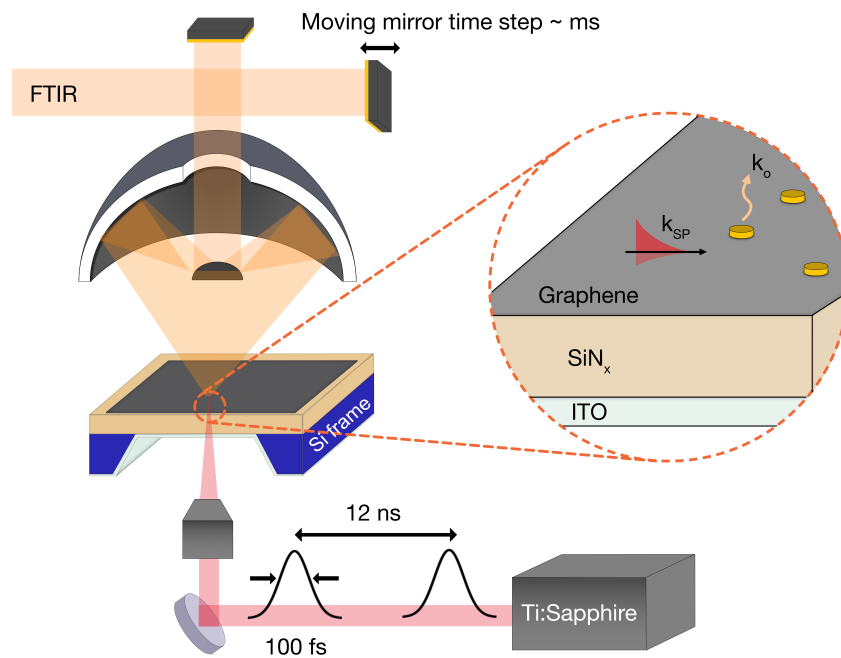


Figure 4.1: Far-field infrared emission measurement setup.

## Optical properties of the device

Understanding the optical properties of the device structure is important in analyzing the emission spectra. The optical properties for graphene are determined by the conductivity model within the random phase approximation [3]. The dynamic conductivity is defined as a function of frequency, carrier temperature and graphene chemical potential as follows:

$$\sigma(\omega) = \sigma_{\text{intra}}(\omega) + \sigma_{\text{inter}}(\omega) \quad (4.1)$$

$$\sigma_{\text{intra}}(\omega) = \frac{i2e^2k_{\text{B}}T}{\pi\hbar^2(\omega + i\tau^{-1})} \log\left(2\cosh\left(\frac{E_{\text{F}}}{2k_{\text{B}}T}\right)\right) \quad (4.2)$$

$$\sigma_{\text{inter}}(\omega) = \frac{e^2}{4\hbar} G\left(\frac{\hbar\omega}{2}\right) + \frac{ie^2\omega}{\pi} \int_0^{\infty} dE \frac{G(E) - G\left(\frac{\hbar\omega}{2}\right)}{(\hbar\omega)^2 - (2E)^2} \quad (4.3)$$

where  $G(E) = \frac{\sinh\left(\frac{E}{k_{\text{B}}T}\right)}{\cosh\left(\frac{E}{k_{\text{B}}T}\right) + \cosh\left(\frac{E_{\text{F}}}{k_{\text{B}}T}\right)}$ .

The optical properties of ITO are modeled with the Drude model:  $\epsilon(\omega, \omega_{\text{p}}(T)) = \epsilon_{\infty} - \frac{\omega_{\text{p}}^2}{\omega^2 + i\gamma\omega}$ . The following parameters are used for ITO films grown with the experimental conditions stated above: the high frequency permittivity  $\epsilon_{\infty} = 4$ , the effective electron mass  $m^* = 0.28 m_{\text{e}}$ , the scattering time  $\tau = 5$  fs, and the background carrier density  $n_{\text{e}} = 2.3 \times 10^{20} \text{ cm}^{-3}$ . The departure from the room temperature optical properties of ITO above sufficiently high electronic temperature (which is the case under the pulsed laser excitation) is calculated based on the previous study on the temperature-dependent plasma frequency of ITO,  $\omega_{\text{p}}$ , due to its non-parabolicity of the conduction band [5]. By modelling the non-parabolic band structure as  $\frac{\hbar^2 k^2}{2m} = E + \frac{E^2}{E_{\text{g}}}$ , where  $1/E_{\text{g}}$  represents the

degree of non-parabolicity, the temperature-dependent plasma frequency takes the following form:

$$\omega_p(\mu, T)^2 = \frac{e^2}{3m\pi^2} \int_0^\infty dE \left[ \frac{2m}{\hbar^2} \left( E + \frac{E^2}{E_g} \right) \right]^{3/2} \left( 1 + \frac{2E}{E_g} \right)^{-1} \left[ -\frac{\partial f(\mu, T)}{\partial E} \right] \quad (4.4)$$

The temperature-dependent chemical potential,  $\mu$ , was obtained for a given carrier density,  $n$ , and temperature,  $T$ , by solving the following equation:

$$n(\mu, T) = \frac{1}{\pi^2} \int_0^\infty dE \frac{m}{\hbar^2} \left( 1 + \frac{2E}{E_g} \right) \left[ \frac{2m}{\hbar^2} \left( E + \frac{E^2}{E_g} \right) \right]^{1/2} f(\mu, T) \quad (4.5)$$

The optical properties of  $\text{SiN}_x$  in the mid-infrared are modeled by a classical Maxwell-Helmholtz-Drude dispersion model presented [12]. For the simulations in the visible and near-infrared spectral ranges, the refractive index of  $\text{SiN}_x$  is assumed to be 2. We use a finite element method to calculate the temperature-dependent optical absorptivity (emissivity) of the device, consisting of a planar graphene layer on a 1- $\mu\text{m}$ -thick  $\text{SiN}_x$  and a 50-nm-thick ITO, under plane wave incident using the temperature-dependent optical properties described above. The calculated graphene-Fermi-level-dependent absorptivity (emissivity) of the device is in good agreement with the measured absorptivity at ambient temperature as shown in Fig. 4.2. The emissivity contribution from each layer can also be extracted from the calculated electromagnetic power density. The results are shown in Fig. 4.3. At the wavelength range longer than 8  $\mu\text{m}$ , the majority of the emissivity comes from the  $\text{SiN}_x$  layer. The majority of the gate dependence comes from the  $\text{SiN}_x$  layer due to the Fabry-Perot mode formed in the  $\text{SiN}_x$  layer sandwiched between the graphene and ITO layers.

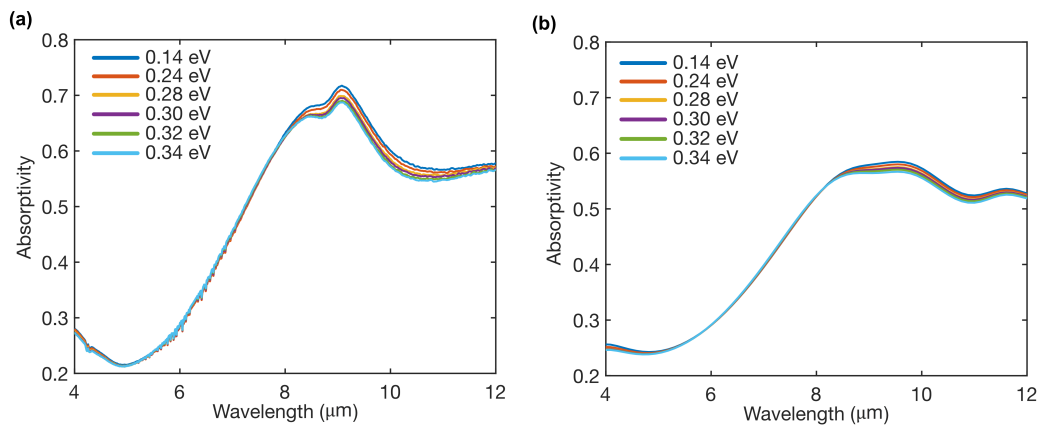


Figure 4.2: Graphene-Fermi-level-dependent absorptivity (emissivity) of the graphene/SiN<sub>x</sub>/ITO device. (a) measured and (b) calculated.

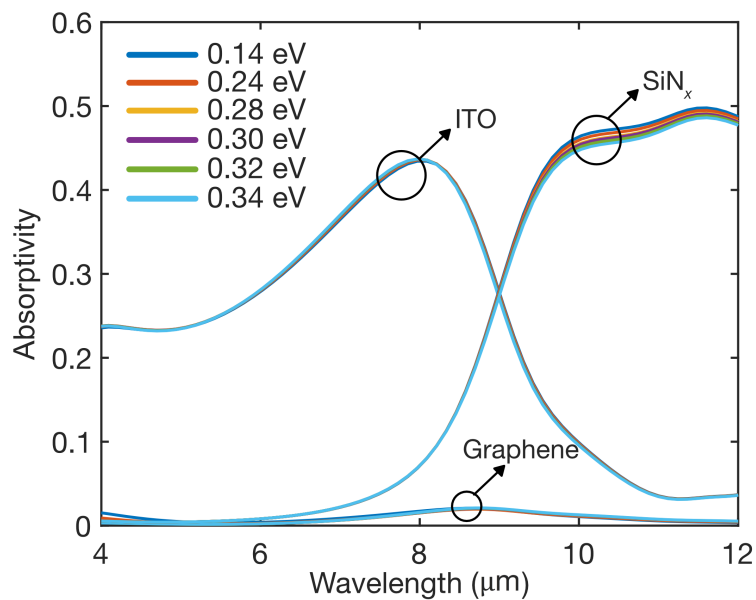


Figure 4.3: Graphene-Fermi-level-dependent absorptivity (emissivity) contribution from each layer at ambient temperature.

## 4.2 Mid-infrared emission phenomena under pulsed laser excitation

Emission spectra from the graphene device under pulsed laser excitation with a constant fluence of  $1.12 \text{ J m}^{-2}$  are shown in Fig. 4.4. Graphene Fermi levels are controlled via applying gate voltages across the  $1\text{-}\mu\text{m}$ -thick  $\text{SiN}_x$  layer. The graphene Fermi levels denoted in Fig. 4.4 are the gate-controlled Fermi levels determined under equilibrium conditions. The laser-pumped spectra are compared with the measured thermal emission spectrum from the device measured at  $95 \text{ }^\circ\text{C}$ . An increase in emission intensity with increasing graphene Fermi level was observed between  $4.5 \text{ }\mu\text{m}$  and  $8 \text{ }\mu\text{m}$  under pulsed laser excitation. The deviation from the measured thermal emission profile occurs in the equivalent spectral range.

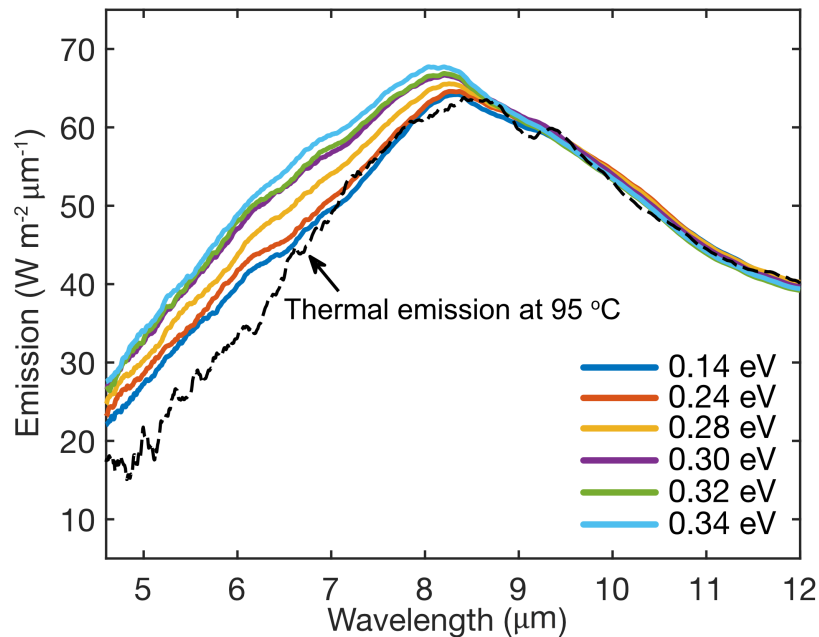


Figure 4.4: Graphene-Fermi-level-dependent emission in a planar graphene under pulsed laser excitation with a constant fluence of  $1.12 \text{ J m}^{-2}$  (solid color lines), compared with measured thermal emission spectrum at  $95 \text{ }^\circ\text{C}$  (dotted black line).

### Comparison with Planckian radiation spectra

Mid-infrared radiation falls in the spectral range in which heated objects typically emit blackbody radiation. To study contributions of plasmon emission, which is non-Planckian, we compare the emission collected under pulsed laser excitation with gate-dependent thermal emission. The solid lines in Fig. 4.5 are the graphene-Fermi-level-dependent thermal emission spectra of the graphene-SiN<sub>x</sub>-ITO device under isothermal conditions at 95 °C. They are obtained by multiplying the gate-dependent absorptivity of our device measured at room temperature by Planck's blackbody radiation spectrum at 95 °C. The absorptivity (or emissivity) of the device shows a gate dependence between 8 μm and 12 μm, which is due to Pauli-blocking as the graphene Fermi level is varied. Notably, the gate dependence due to this effect shows an opposite trend to that seen in emission under pulsed optical excitation, and occurs in a different spectral region (>8 μm for isothermal; <8 μm for pulsed).

Under pulsed optical excitation, the temperature of the device is time-dependent, and the temperature of each layer is expected to evolve differently as each layer absorbs different degrees of the incoming laser light. Thus, to understand how the time-dependent temperature evolution would manifest in a time-averaged emission spectrum, a phenomenological two-temperature (2T) model was adopted to calculate temporal evolutions of temperatures in graphene as discussed in Chapter 2. The coupled partial differential equations for electron and phonon temperatures of ITO take the same forms as those for graphene. The electron-phonon exchange rate of ITO is expressed in Ref. [1], and is a function of the Debye temperature, the Fermi velocity, the electron mean free path, and the Fermi energy. All of these parameters were deduced from the

parameters used in the Drude model, specifically  $n_e$ ,  $m^*$ , and  $\tau$ . The values of  $v_F = 7.84 \times 10^5 \text{ m s}^{-1}$ ,  $l = 3.92 \text{ nm}$ ,  $E_F = 0.49 \text{ eV}$ , and  $\theta_D \approx 1,000 \text{ K}$  were used.

A population of photo-excited electrons thermalizes via electron-electron scattering and creates a hot bath of electrons that can be significantly hotter than the lattice. It has been previously shown that these hot electrons can emit radiation with a spectral density consistent with Planck's law [9]. We used a finite element method to calculate temperature-dependent emissivity contributions from graphene and ITO layers. The  $\text{SiN}_x$  layer exhibits negligible absorption at the incoming laser wavelength. Thus, it is assumed that the  $\text{SiN}_x$  is heated via conduction only, and that its emissivity contribution does not deviate from its room temperature values. The emission contribution at longer wavelengths ( $> 8 \mu\text{m}$ ) mostly comes from the  $\text{SiN}_x$ , and an effective  $\text{SiN}_x$  was assumed to maintain the overall spectral.

Emissivity and temperature are the parameters that define a Planckian emission spectrum. Both parameters evolve with time and are different in each layer of the device. The temperature dependent emissivity was then multiplied by a blackbody thermal emission spectrum given by Planck's law at a given time. Emission contributions from all three layers of the device were calculated and were added according to  $\sum_{i=\text{graphene,ITO,SiN}_x} \xi_i(T_i(t)) \times S(\lambda, T_i(t))$ , where  $\xi$  is the temperature-dependent emissivity and  $S$  is the blackbody spectral radiance given by Planck's law. The time-dependent spectra were time-integrated according to  $I(\lambda) = \frac{\int \xi(T(t)) \times S_\lambda(\lambda, T(t)) dt}{\int dt}$ , where  $S_\lambda(\lambda, T) = \int \frac{2hc^2}{\lambda^2} \frac{1}{\exp\left(\frac{hc}{\lambda k_B T}\right) - 1} d\Omega$  is the blackbody spectral radiance given by Planck radiation integrated over the collection solid angle, and  $\xi(T)$  is the temperature-dependent emissivity [3, 5].

The laser illumination was expanded to ensure uniform illumination over the measurement area of  $50 \mu\text{m} \times 50 \mu\text{m}$ . Thus, it is assumed the temperature is spatially uniform. The results are time-averaged and are shown as dotted curves in Fig. 4.5. We note that the gate voltage dependence observed in the 2T model-governed emission between  $4.5 \mu\text{m}$  and  $8 \mu\text{m}$  is opposite to that seen in the measured spectra under pulsed optical excitation. The pulsed-laser-induced behavior of the emission phenomena between  $4.5 \mu\text{m}$  and  $8 \mu\text{m}$  cannot be explained with Planckian light emission mechanisms.

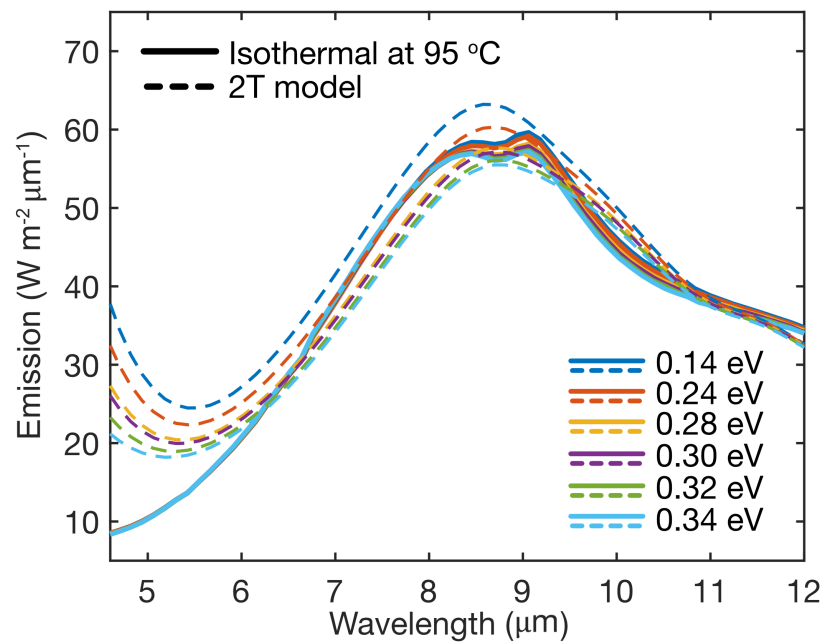


Figure 4.5: Planckian thermal emission under isothermal (solid color lines) and varying temperature (dotted color lines) conditions.

### **Gate dependence originating from graphene Fermi level modulation**

We note that the gate dependence in the observed emission between 4.5  $\mu\text{m}$  and 8  $\mu\text{m}$  under pulsed laser excitation arises only from graphene. For our experimental conditions, the optical properties and temperature profile of ITO do not change significantly upon applied gate voltages. It has been previously reported that applying a sufficiently high gate voltage of order 1 V per 1 nm to ITO can yield a charge accumulation layer in ITO [6]. However, the charge accumulation in the ITO layer is negligible in our experimental conditions. A gate voltage of approximately 0.1 V nm<sup>-1</sup> was applied across the SiN<sub>x</sub> layer, so the applied electric field in our experiment is an order of magnitude smaller than that required to induce an ITO accumulation layer. As an independent check to demonstrate that gate voltage-dependent modulation comes from the Fermi level modulation in graphene rather than ITO, a control experiment was performed. A graphene-less control sample was made, consisting of a 1- $\mu\text{m}$ -thick SiN<sub>x</sub> sandwiched between 50-nm-thick ITO layers, which served as top and bottom gates. When illuminated with pulsed laser excitation with a fluence of 1.12 J m<sup>-2</sup>, negligible gate dependence was observed as shown in Fig. 4.6.

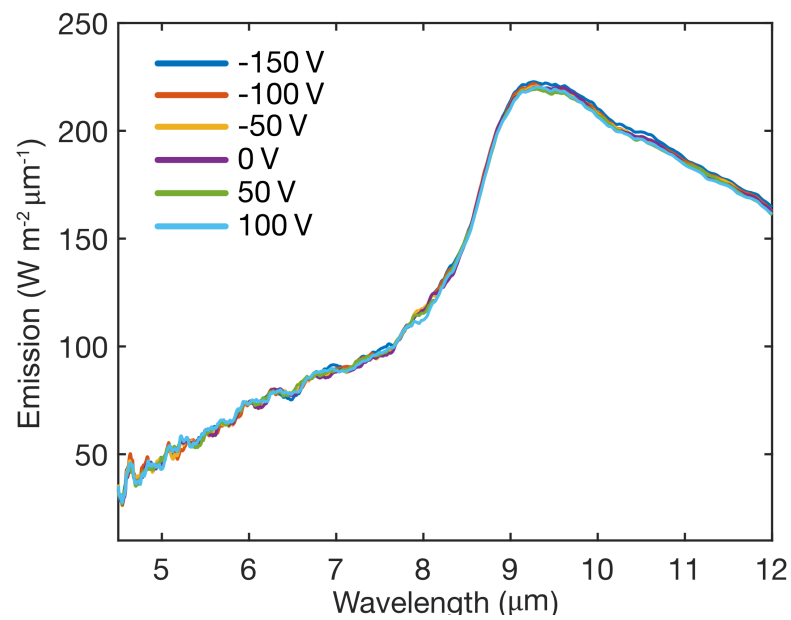


Figure 4.6: Measured emission spectra from ITO-SiN<sub>x</sub>-ITO for various gate voltages under pulsed laser excitation with a constant laser fluence of 1.12 J m<sup>-2</sup>.

**Comparison with emission under continuous wave (CW) laser excitation**

The gate-dependent emission spectra under CW laser excitation with an equivalent laser average power from the device are shown in Fig. 4.7, and are compared with the observed emission behavior under pulsed laser excitation (Fig. 4.7). Under CW laser excitation, the gate dependence occurs at longer wavelengths ( $>8 \mu\text{m}$ ) similar to that seen in thermal emission under isothermal conditions (Fig. 4.5). The spectral shape observed in the emission spectra under CW laser excitation is in good agreement with that of thermal emission measured at  $95^\circ\text{C}$ . Considering a peak power of a 100-fs laser pulse, which is approximately  $1.25 \times 10^5$  times higher than the average power, the carrier generation rate is approximately five orders of magnitude higher under pulsed laser excitation than that under CW laser excitation. Thus, in comparison to the emission behavior under CW laser excitation, the observed emission phenomena under pulsed laser excitation are due to carriers excited with a 100-fs laser pulse (i.e., enough carriers to achieve inversion).

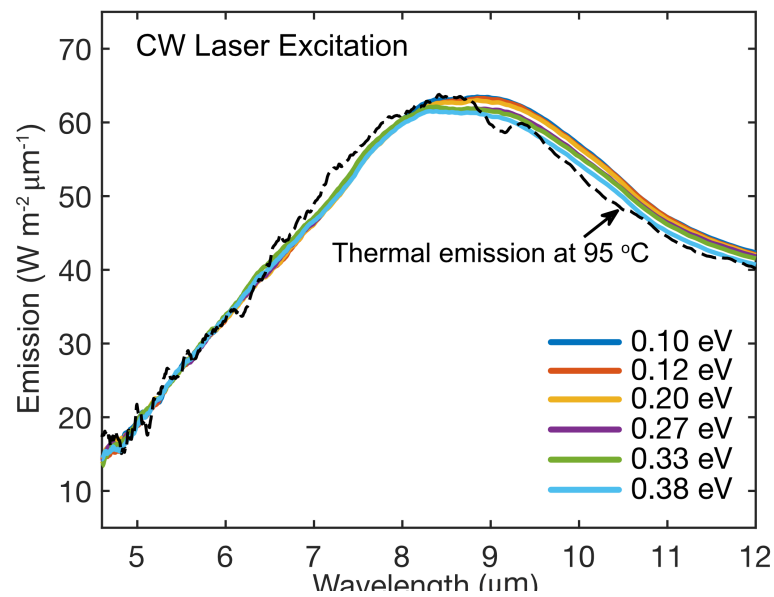


Figure 4.7: Measured gate voltage-dependent emission spectra under continuous wave (CW) laser excitation with a constant fluence of  $1.12 \text{ J m}^{-2}$  (solid color lines), compared with measured thermal emission spectrum at  $95 \text{ }^\circ\text{C}$  (dotted black line).

### 4.3 Non-Planckian radiation contribution: plasmon emission

The plasmon decay rates,  $\gamma_p$ , as a function of wavelength for various gate-controlled graphene Fermi levels for a given laser fluence of  $1.12 \text{ J m}^{-2}$  are shown in Fig. 4.8. The dispersion calculations are carried out for wavelengths  $< 8 \text{ }\mu\text{m}$ , as the phonons in  $\text{SiN}_x$  strongly suppress plasmon excitation and associated gain for wavelengths above  $8 \text{ }\mu\text{m}$ . The main source of the observed emission at wavelengths  $> 8 \text{ }\mu\text{m}$  is thermal emission due to substrate heating. The calculations suggest that there is net plasmon gain ( $\gamma_p > 0$ ) under the given experimental conditions for all gate-controlled graphene Fermi levels over the spectral range of interest. Furthermore, the gate dependence observed in the calculated plasmon decay rates suggests that plasmon emission rates increase with gate-controlled graphene Fermi levels. This trend is consistent with the gate dependence observed in emission under pulsed laser excitation (Fig. 4.4). The snapshots of the plasmon decay rates at a given time for a given gate-controlled graphene Fermi level of  $0.34 \text{ eV}$  in the spectral range of interest (i.e., where the pulsed-laser-induced increase in emission with graphene Fermi level is observed) are shown in Fig. 4.9. The spectral range that allows net plasmon emission diminishes as the population inversion in graphene depletes over time.

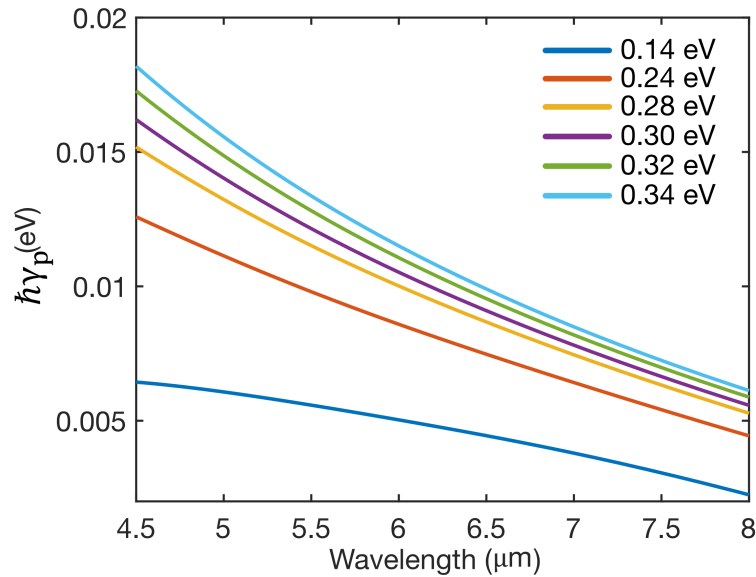


Figure 4.8: For a fixed laser fluence of  $1.12 \text{ J m}^{-2}$ , plasmon decay rates for different gate-controlled graphene Fermi levels at  $t_0$ , the time at which carriers have just thermalized and the carrier temperature is at its maximum.  $\gamma_p > 0$  denotes net plasmon generation, and  $\gamma_p < 0$  denotes net plasmon loss.

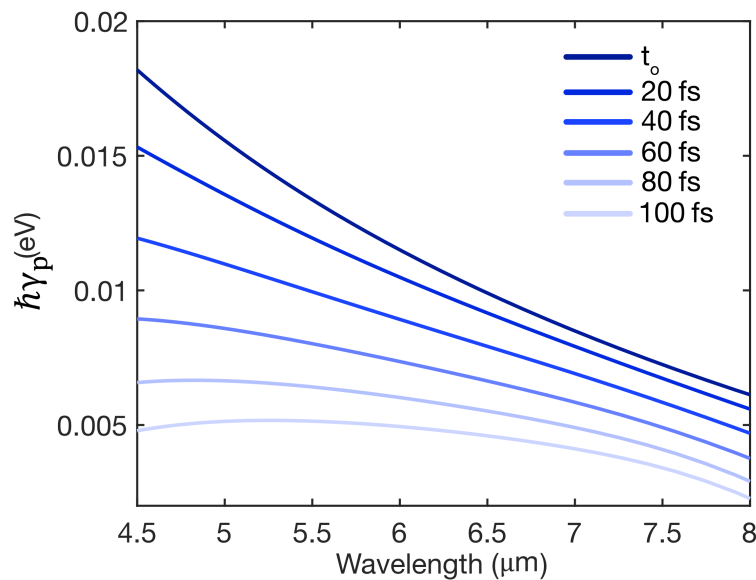


Figure 4.9: For a given gate-controlled graphene Fermi level of  $0.34 \text{ eV}$  and laser fluence of  $1.12 \text{ J m}^{-2}$ , the temporal evolution of the plasmon decay rates. Time denoted in the legend indicates the time that has passed since  $t_0$ .

The contributions of stimulated and spontaneous plasmon emission per excitation pulse are discussed in Chapter 3. It was found that on a 100-fs timescale, stimulated emission may dominate spontaneous emission depending on the scattering loss rates. Spontaneous emission dominates stimulated emission at longer times, and the time-integrated emission collected from each pulse is dominated by spontaneous plasmon emission (Fig. 3.10). Assuming that the generated plasmons emit incoherently into all possible modes, the spontaneous emission spectra can be estimated by weighting the plasmon free space emission rates (Eq. 3.1) by the plasmon density of states given by  $D_p(\omega) = \frac{k(\omega)}{2\pi} \frac{dk(\omega)}{d\omega}$  [10, 11]. The time-integrated spontaneous plasmon emission spectra for various gate-controlled graphene Fermi levels are shown in Fig. 4.10. The calculated spontaneous emission spectra predict the same gate-dependent trend in the spectral region of interest as seen in the experimentally measured emission under pulsed laser excitation. The increase in emission with increased hole doping of graphene can be intuitively understood as a result of enlarging the phase space for the excited carriers to relax by emitting plasmons. Moreover, as more carriers are added to the excited state population, more spontaneous plasmon emission is expected. The time-integrated spontaneous emission spectra for a given gate-controlled graphene Fermi level with increasing laser fluences are presented in Fig. 4.11. The calculations show that with increasing laser fluences, more plasmons are emitted per excitation pulse with other experimental conditions held constant.

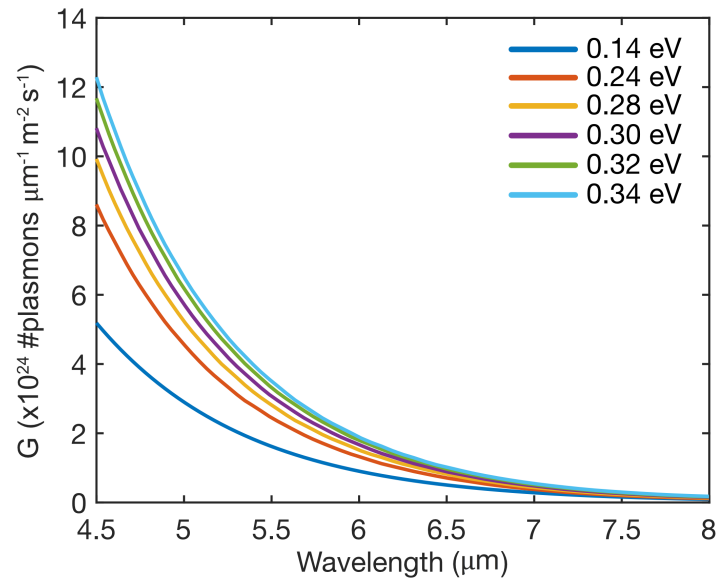


Figure 4.10: Time-integrated spontaneous plasmon emission spectra for different gate-controlled graphene Fermi levels under a laser fluence of  $1.12 \text{ J m}^{-2}$ .

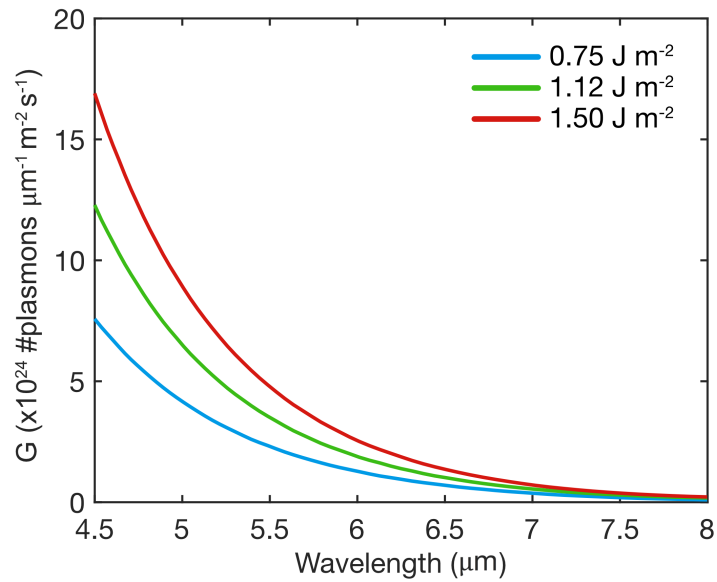


Figure 4.11: Time-integrated spontaneous plasmon emission spectra for a given gate-controlled graphene Fermi level of 0.34 eV under different laser fluences.

#### 4.4 Plasmon-coupled far-field radiation

We proceed to compare the calculated plasmon emission spectra with the measured emission spectra under pulsed laser excitation. The measured gate-dependent light emission is the result of emitted plasmons coupled out to the far field. We obtain the out-coupling efficiency based on the experimental emission data. First, a thermal background expected for a given laser fluence was subtracted from the observed emission to determine the deviation from the thermal background (i.e., excessive emission, which scales with plasmon emission contribution). The subtracted spectra were divided by the calculated plasmon emission spectra. The results represent out-coupling efficiencies of plasmons, which were found to be in the order of  $10^{-4}$ , as shown in dotted lines in Fig. 4.12(c). Two-dimensional full-wave simulations were used to verify the out-coupling efficiency. To confirm the spectral shape and the order of magnitude of the experimentally determined out-coupling efficiency, we performed two-dimensional full-wave simulations as depicted in Fig. 4.12(b). The AFM measurement of a  $\text{SiN}_x$  surface showed the root mean square roughness of 0.4 nm as shown in Fig. 4.12(a). The rough surface was modeled by  $\sqrt{2}R_{\text{RMS}}\cos(2\pi P_x x)$ , where  $R_{\text{RMS}}$  is the root mean square surface roughness and period of sinusoidal function  $P_x$  is chosen by 6 nm. Graphene is assumed to conform to the roughness of the substrate, and graphene plasmons are launched within one period of the rough surface enclosed by perfect electric conductors to model uniformly excited plasmons over a laser-illuminated area. In these simulations, the graphene carrier temperature of 2,000 K and the collision loss time of 50 fs were assumed. The radiation efficiency was calculated by the radiation power toward air divided by the launching power of graphene plasmons.

Here, a substrate consisting of a 1- $\mu\text{m}$ -thick  $\text{SiN}_x$  layer and a 50-nm-thick ITO layer was assumed. Figure 4.12(d) confirms that the surface roughness is sufficient to scatter graphene plasmons into free-space. In particular, the spectral shape and the order of magnitude of the calculated radiation efficiency are consistent with the experimentally determined out-coupling efficiency. The calculated value is slightly smaller than the experimentally determined out-coupling efficiency. We note that there exist other possible scattering centers that are difficult to simulate, such as residues (e.g., PMMA, metal nm-scale islands from fabrication processes), graphene sheet folding, and grain boundaries, that can further increase the out-coupling efficiencies of graphene plasmons.

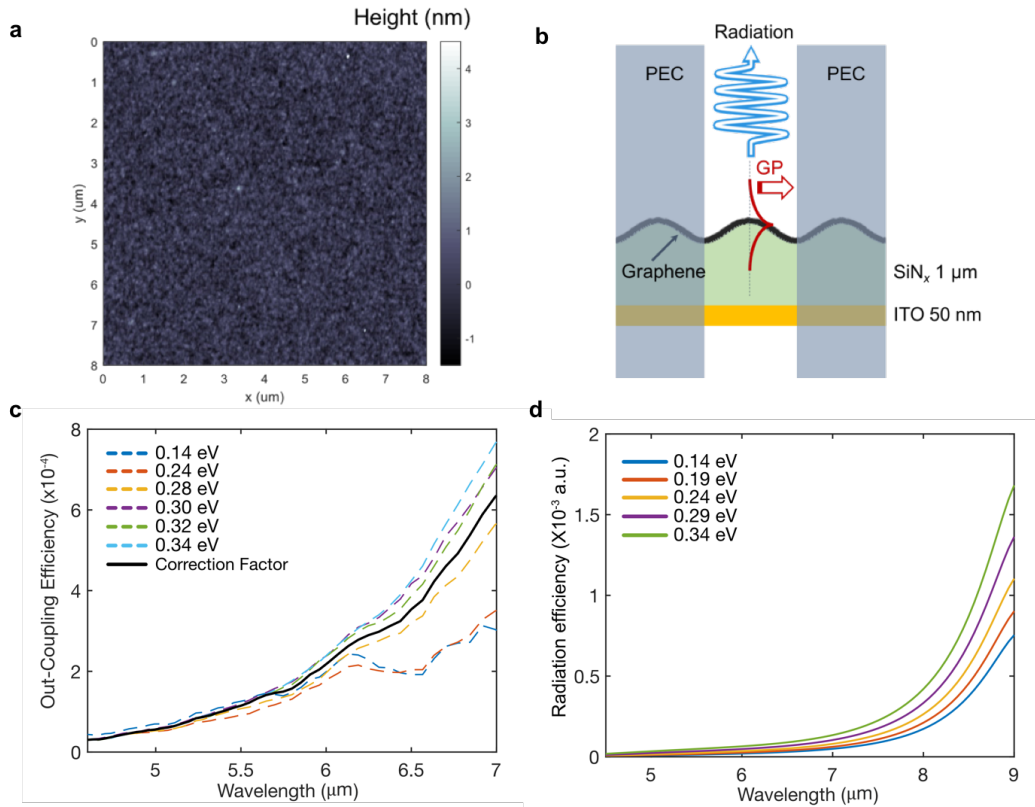


Figure 4.12: (a) AFM measurement of a  $\text{SiN}_x$  surface, showing root mean square roughness of 0.4 nm. (b) Schematic for calculating radiation efficiencies of graphene plasmons propagating on a planar graphene surface which conforms to the roughness of the underlying  $\text{SiN}_x$ . (c) Experimentally determined out-coupling efficiencies. (d) Calculated radiation efficiencies.

### **Direct comparison with experimental results**

For a direct comparison with the experimentally measured emission spectra, the calculated spontaneous emission spectra are then multiplied by the out-coupling efficiency of plasmons. The gate-dependent results are shown in dotted curves in Fig. 4.13, and are in good agreement with the measured emission under pulsed laser excitation. As the laser fluence increases, more plasmon-coupled radiation was observed experimentally in the spectral region where net plasmon gain is predicted ( $\gamma_p > 0$ ). The measured laser-fluence-dependent emission spectra agree well with the calculated, out-coupled spontaneous plasmon emission spectra as shown in Fig 4.14. In a planar graphene, the far-field observation of bright plasmon emission is limited by inefficient out-coupling mechanisms. As we demonstrate in the next section, such a limitation can be easily overcome with appropriate nanophotonic structures.

The deviation from the theoretical prediction can be attributed to inevitable uncertainty in determining gate-controlled graphene Fermi levels and charge density fluctuations, which led to non-uniform charge neutral point across the sample. The carrier densities of varying gate voltages were obtained from a simple parallel capacity model with a 1- $\mu\text{m}$ -thick  $\text{SiN}_x$  dielectric. In our previous studies [2, 7], we have identified that atmospheric impurities contribute to the discrepancy between the extracted charge densities and the real values. Our measurements were performed under FTIR purge gas (free of  $\text{H}_2\text{O}$  and  $\text{CO}_2$ ). Atmospheric impurities that are likely to present in the purge gas have previously been shown to induce hysteresis effects in the conductance curves of graphene FET devices [8, 15, 17, 18]. In addition, the concentration of such impurities can depend on the applied gate bias. Also, the  $\text{SiN}_x$  surface

itself can contain charge traps that get filled or empty with the applied gate bias. Such charge traps could induce anomalous behavior in the conductance curves of the graphene FET devices, similar to what has been observed in the presence of metallic impurities [13].

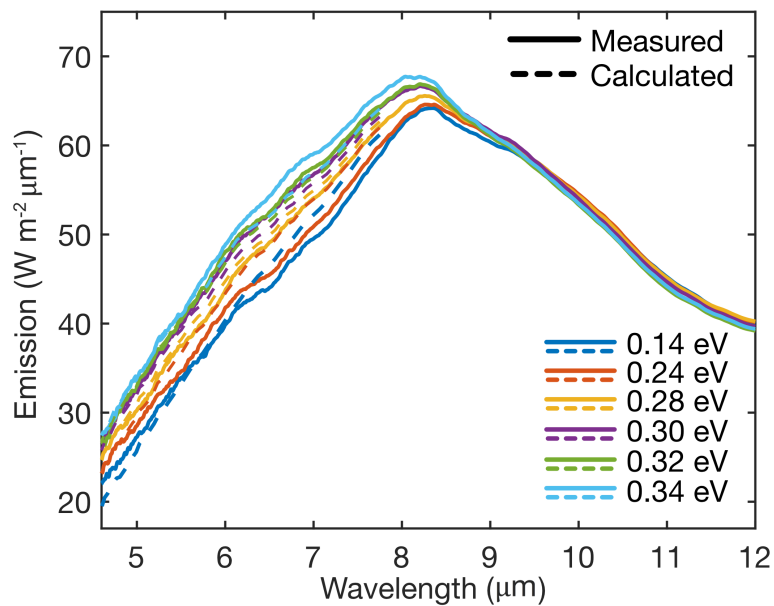


Figure 4.13: Gate-dependent measured emission spectra (solid color lines) under pulsed laser excitation compared with the out-coupled, calculated spontaneous plasmon emission spectra (dotted color lines). In both cases, the relevant laser fluence is  $1.12 \text{ J m}^{-2}$ .

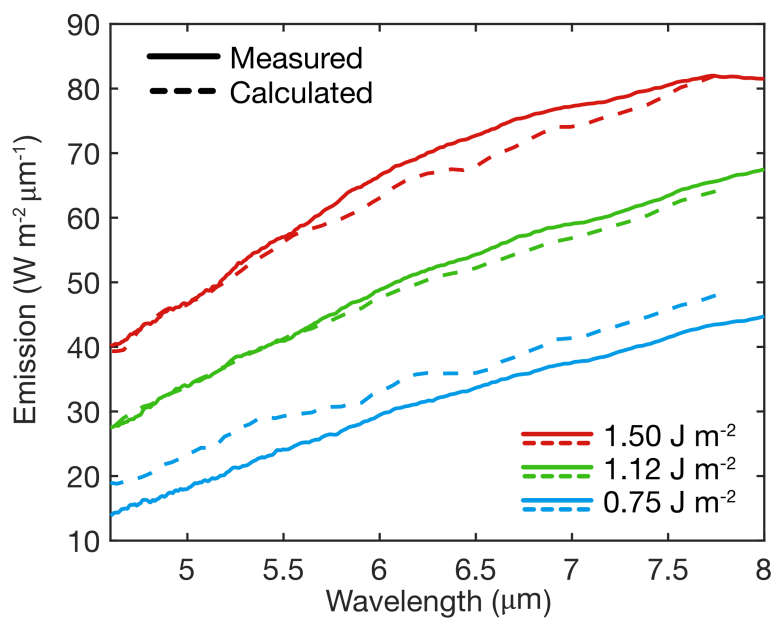


Figure 4.14: Laser-fluence-dependent measured emission spectra under pulsed laser excitation (solid color lines), compared with the calculated, out-coupled spontaneous plasmon emission spectra (dotted color lines). In both cases, the relevant gate-controlled graphene Fermi level is 0.34 eV.

#### 4.5 Roles of gold nanodisks

We demonstrate that the far-field intensity of the plasmon emission processes can be enhanced by placing engineered metastructures on graphene surface. Gold nanodisks (NDs) were fabricated by patterning onto a PMMA resist on top of the graphene layer by 100 keV electron beam lithography and evaporating a 2-nm-thick Ti followed by a 80-nm-thick Au. The gold NDs promote localized plasmon excitations due to the plasmonic-resonance-induced near-field enhancements, and also increase radiation efficiencies of plasmons by acting as out-coupling scatterers. The plasmonic resonance of the NDs depends on their diameter; the diameter was chosen to be 175 nm and 285 nm for the NDs that are resonant and non-resonant, respectively, with the incoming laser excitation light. The NDs are randomly distributed in order to prohibit in-plane resonances originating from perfect periodicity. Over a  $150\ \mu\text{m} \times 150\ \mu\text{m}$  area, 10,000 nanodisks were fabricated, covering approximately 1% and 2.8% of the graphene surface for the resonant and non-resonant nanodisks, respectively. In addition, the nanodisks are separated by at least 800 nm in center-to-center distance to suppress plasmonic interactions between the adjacent gold nanodisks. The electric field intensity profiles of the resonant and non-resonant NDs on a semi-infinite  $\text{SiN}_x$  substrate are presented in Fig. 4.15, and their optical cross-sections are shown in Fig. 4.16. The NDs are designed to have a negligible effect on the overall emissivity of the device. Figure 4.17 compares the measured emissivity of the samples with and without the NDs. Because the distribution of the NDs is sparse and the size of them is small in the perspective of mid-infrared light, the NDs have negligible effect on the overall emissivity of the sample in mid-infrared. In addition, full-wave simulation results suggest

that the overall absorption as well as the absorption in graphene at the laser wavelength of 850 nm are not significantly altered by the NDs, as shown in Fig. 4.18.

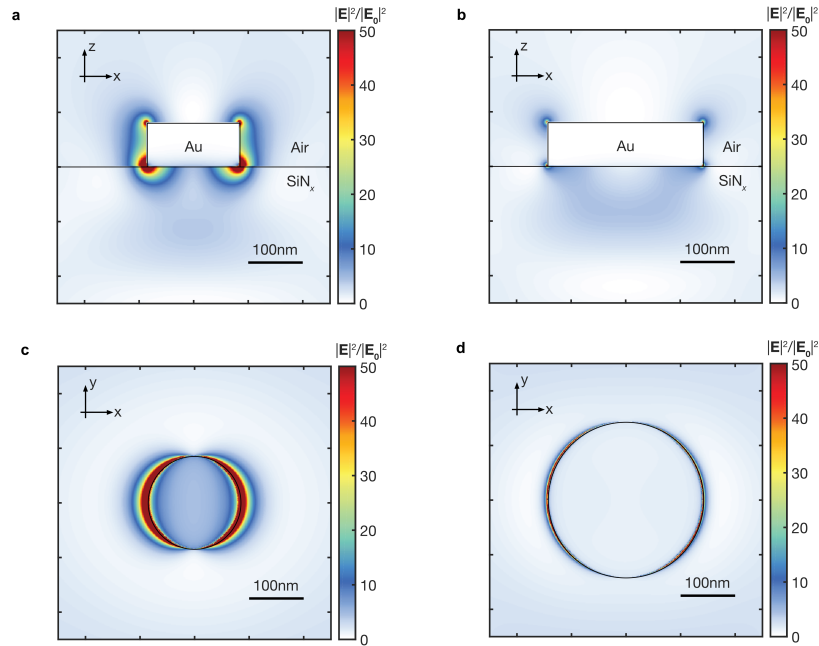


Figure 4.15: Electric intensity distribution under the planar wave excitation at the laser wavelength of 850 nm. Side view electric intensity distributions of Graphene/SiNx/ITO structure with the (a) resonant and (b) non-resonant NDs. Top view electric intensity distributions for the (c) resonant and (d) non-resonant NDs.

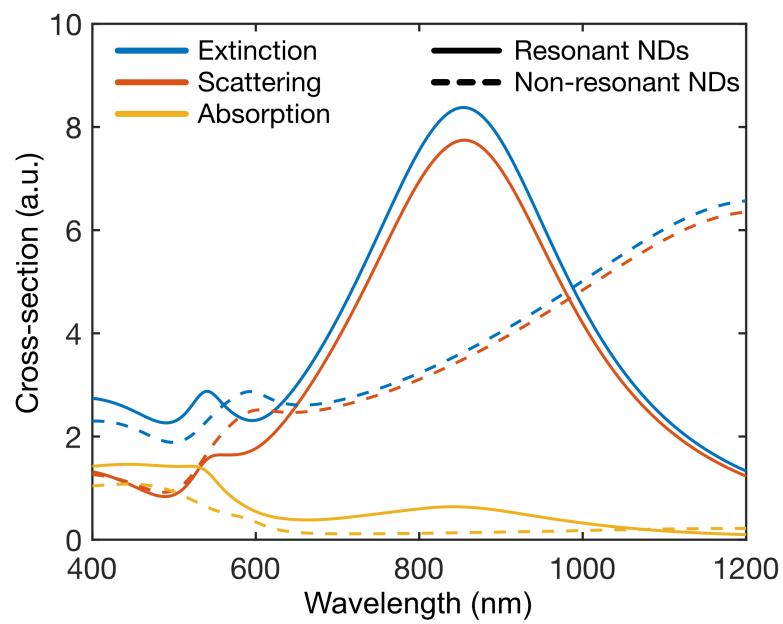


Figure 4.16: Optical cross-sections of the resonant and non-resonant NDs.

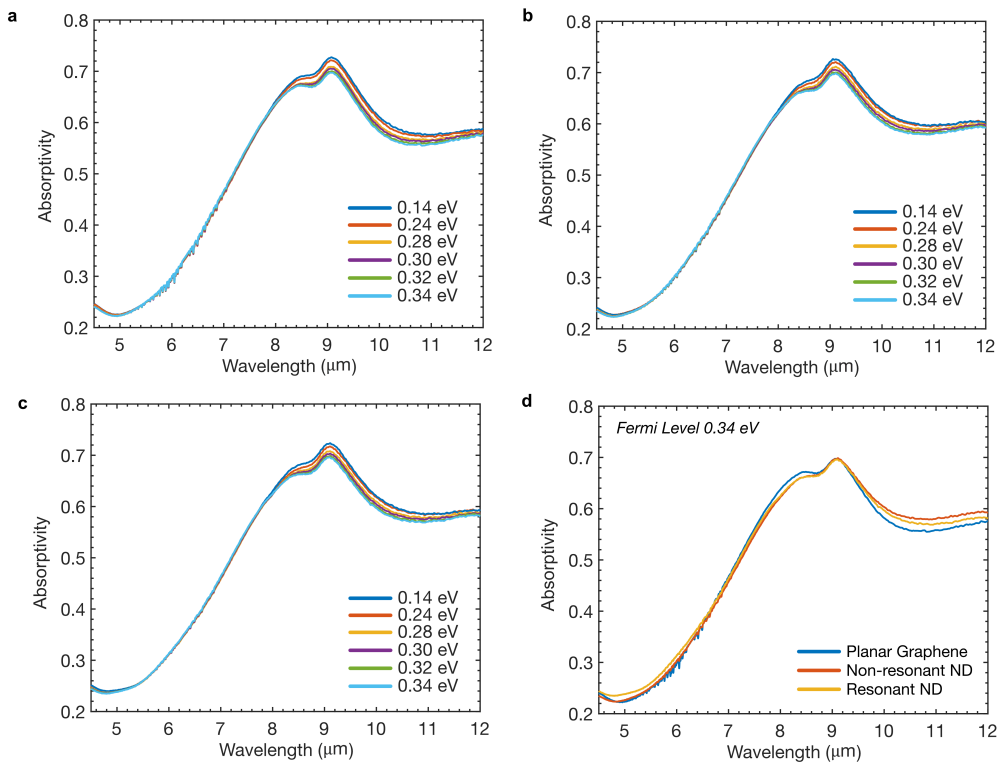


Figure 4.17: Gate-dependent measured absorptivity (or emissivity) of the graphene/ $\text{SiN}_x$ /ITO structure with and without NDs at ambient temperature. (a) Planar graphene. (b) Non-resonant NDs on graphene. (c) Resonant NDs on graphene. (d) For a fixed graphene Fermi level at 0.34 eV, the measured emissivities with and without the NDs.

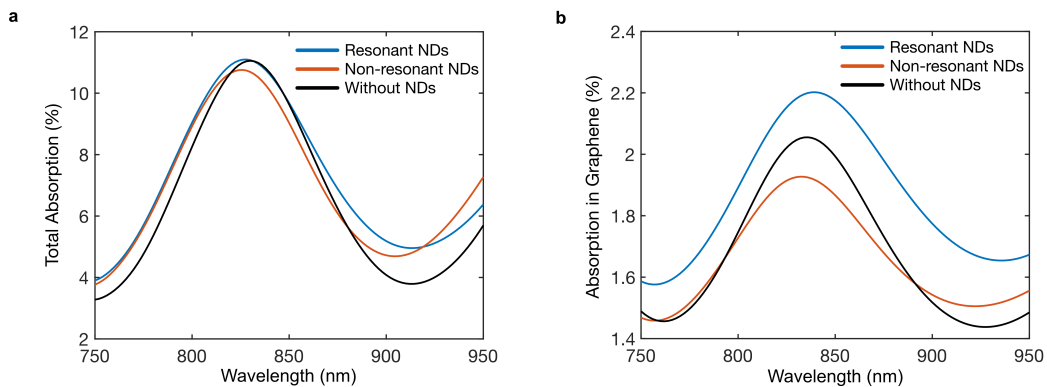


Figure 4.18: (a) Total absorptions of the graphene/ $\text{SiN}_x$ /ITO device with and without the NDs. (b) Absorptions in graphene with and without the NDs.

Figure 4.21 shows the measured emission spectra under pulsed laser excitation from planar and ND-decorated graphene samples. At long wavelengths ( $>8 \mu\text{m}$ ), the observed emission spectra match well with the measured thermal emission profiles, with the ND-decorated samples reaching apparent higher temperatures than the planar graphene sample. This suggests that the gold NDs act as local heating source due to their absorption at 850 nm. However, in addition to those heating effects, the resonant and non-resonant NDs cause a large gate-dependent deviation from the thermal emission profiles between  $4.5 \mu\text{m}$  and  $8 \mu\text{m}$ . At shorter wavelengths ( $<8 \mu\text{m}$ ), we start to see deviations from the measured thermal emission profiles and increasing gate dependence that are distinct from that seen in gate-dependent thermal emission as well as emission under CW laser excitation as shown in Figs. 4.19 and 4.20, respectively. Such deviation and its gate dependence are larger when graphene is decorated with the gold NDs for a given laser excitation fluence. In comparison to the observed emission spectra under CW laser excitation (Fig. 4.20), the large gate-dependent deviation from the measured thermal emission profiles between  $4.5 \mu\text{m}$  and  $8 \mu\text{m}$  seen in Fig. 4.21 is the result of the excited carriers generated with a 100-fs pulsed laser excitation. As the emission spectra measured under CW laser excitation resemble the measured thermal emission profiles as shown in Fig. 4.19; thus, under CW laser excitation, the emission contribution is mostly from thermal emission.

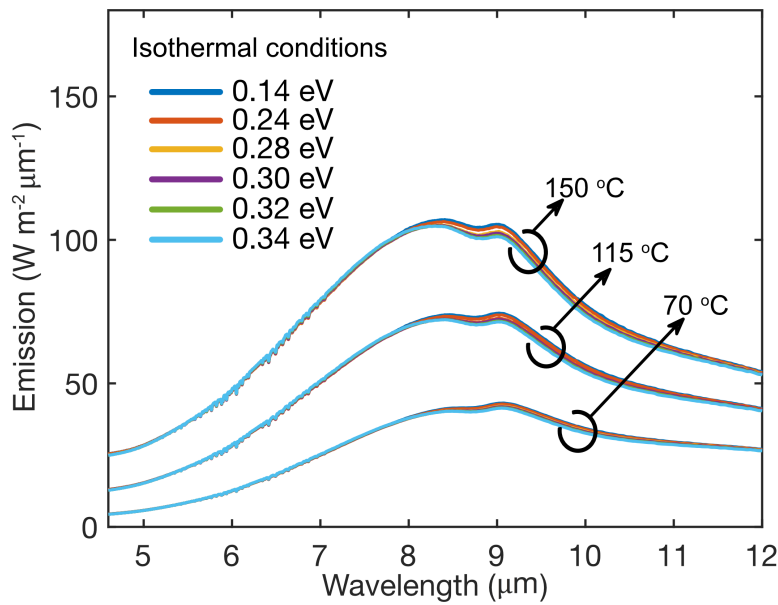


Figure 4.19: Expected gate-dependent thermal emission spectra under isothermal conditions of given temperatures of 70 °C, 115 °C, and 150 °C. The spectra were calculated by multiplying the measured gate-dependent absorptivity of the device by Planck's spectrum of a corresponding temperature.

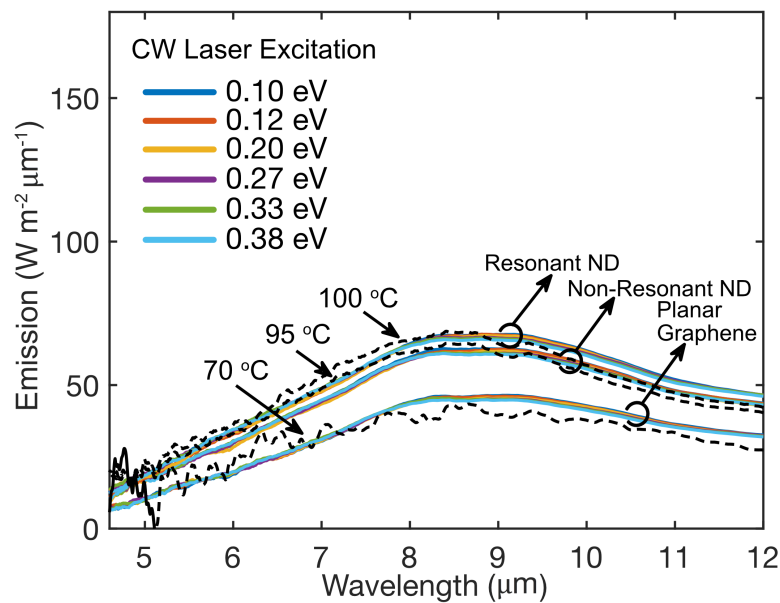


Figure 4.20: Gate-dependent emission spectra from planar and ND-decorated graphene samples under CW laser excitation with a laser fluence of  $0.75 \text{ J m}^{-2}$  (color solid lines). Measured thermal emission spectra from the device for given temperatures of 70 °C, 95 °C, and 100 °C (black dotted lines).

Figure 4.22 shows the spectra under pulsed laser excitation for a given gate-controlled graphene Fermi level of 0.34 eV after the corresponding thermal emission background is subtracted. The samples with resonant and non-resonant NDs display seven and three times larger deviation from the corresponding thermal backgrounds, respectively, in comparison to the planar sample. While localized heating near the NDs could lead to a non-uniform temperature across the sample, the large gate dependence at shorter wavelengths ( $<8 \mu\text{m}$ ) in the presence of NDs suggests that their dominant effect is to more efficiently generate and/or out-couple of hot-carrier generated graphene plasmons (i.e., a given change in plasmon emission with changing  $E_F$  higher out-coupling efficiency = larger out-coupled gate dependence). We note that the large gate-dependent emission seen between  $4.5 \mu\text{m}$  and  $8 \mu\text{m}$  is bigger with resonant NDs than with non-resonant NDs. This effect can be understood as arising from the large field enhancements near the NDs, which are 100 and 10 times larger for the resonant and non-resonant NDs, respectively, than the planar graphene as shown in Fig. 4.23. This field enhancement will impact both population inversion and plasmon emission rates, and it can also enhance absorption in graphene locally, creating more excited carriers in the vicinity of the NDs, where they are more efficiently out-coupled [14].

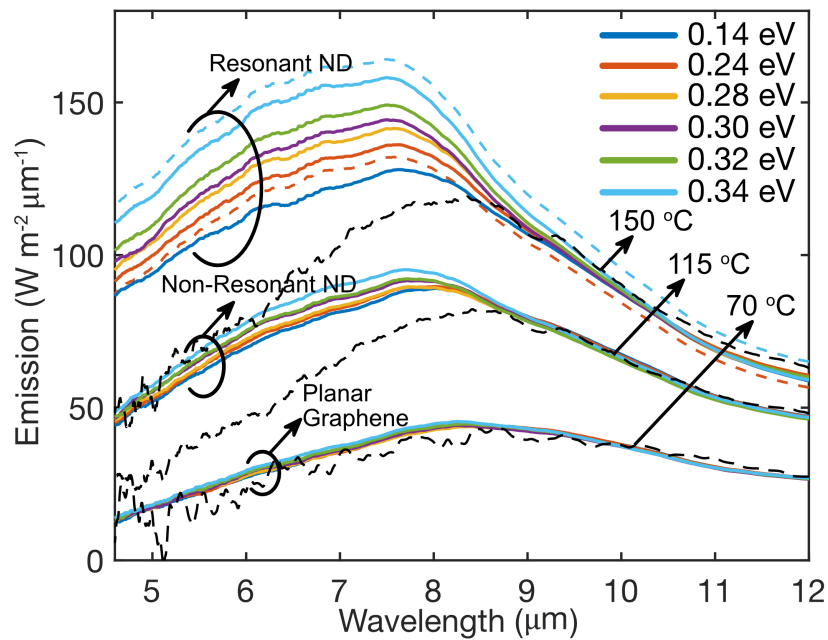


Figure 4.21: Gate-dependent emission spectra from planar and ND-decorated graphene samples under pulsed laser excitation with a constant laser fluence of  $0.75 \text{ J m}^{-2}$  (color solid lines). In the resonant ND data, the dotted lines for 0.24 eV and 0.34 eV correspond to the original measurements, and the solid lines are fitted to compensate the offset, which appeared due to experimental imperfections. Measured thermal emission spectra from the device for given temperatures of 70 °C, 115 °C, and 150 °C (black dotted lines).

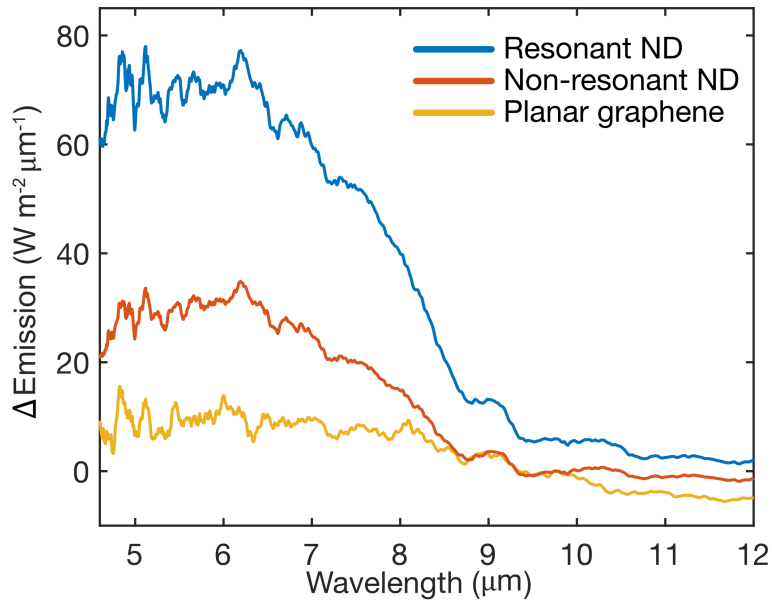


Figure 4.22: Emission contributions that deviate from the corresponding thermal emission background under pulsed laser excitation with a constant laser fluence of  $0.75 \text{ J m}^{-2}$  from planar graphene and ND-decorated graphene samples at a given gate-controlled graphene Fermi level of  $0.34 \text{ eV}$ .

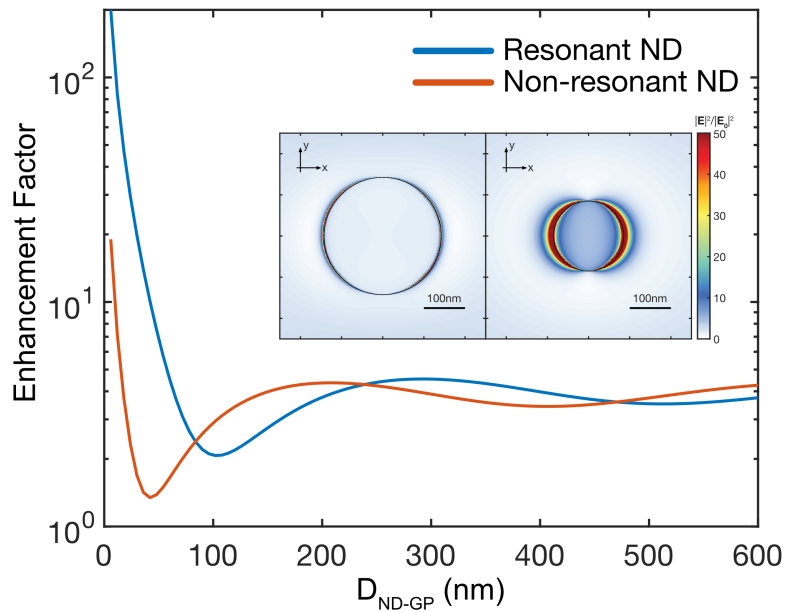


Figure 4.23: Field enhancement factor around the NDs due to the plasmonic resonance.

To study the electromagnetic effects on the radiation efficiency of graphene plasmons, two-dimensional full-wave simulations were performed. The dotted lines in Fig. 4.24 show radiation efficiencies of a single graphene plasmon launched on a rough graphene surface in the presence of NDs without taking the near-field enhancement into consideration (i.e., only considering geometric factors). The ripple patterns in the calculated radiation efficiencies are due to the interferences between the scattered graphene plasmons from the nanodisk and those from the rough surface. As expected, plasmons launched closer to a ND have a higher efficiency of out-coupling to free space. If we assume they act only as scatterers (considering only geometric factors), the radiation efficiency is slightly higher with the non-resonant NDs because its larger diameter makes the non-resonant ND a more efficient out-coupling scatterer. When the field enhancement factor is taken into consideration, the calculated radiation efficiency in the presence of resonant NDs is approximately  $10^5$  times higher near the NDs compared to that on a rough surface of planar graphene. This suggests that the near-field enhancement takes part in improving radiation efficiency of graphene plasmons. It also has been previously reported that resonantly excited nanodisks can inject carriers into graphene [4, 19], effectively changing the doping level of graphene. While this process is difficult to quantitatively assess under our conditions, any hot carrier doping process is likely to contribute to increased plasmon emission. Fermi level pinning for graphene in contact with a metal can locally change the effective chemical potential [16], which could result in more plasmons emitted near the nanodisks. The localized plasmon excitations scatter out more efficiently as they get created near a nanodisk, as shown in Fig. 4.24. These analyses suggest that there are no inherent

limitations of achieving a ultrabright, ultrafast plasmon-assisted light emission, and that engineering of more efficient plasmon out-coupling structures may enable significantly increased brightness. In terms of the near-field enhancement, there are better plasmonic structures than the nanodisks. For example, nanorod antennas with a subwavelength gap and plasmonic bowtie antennas exhibit much stronger plasmonic enhancement in the pumping wavelength than the nanodisk structures. Therefore, we expect that such plasmonic antenna structures could be helpful for enhancing the emission of graphene plasmons.

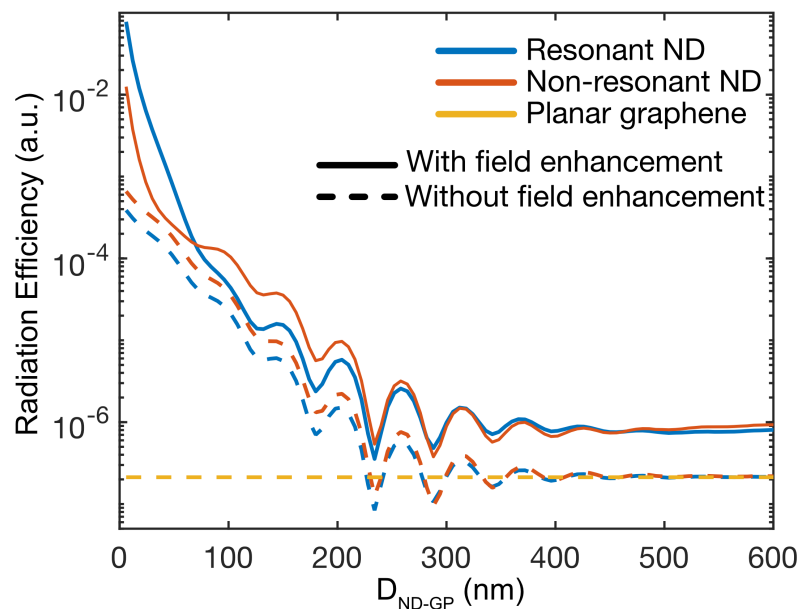


Figure 4.24: Calculated radiation efficiency of graphene plasmons with and without NDs with varying distance from the edge of a ND. The dotted lines represent the plasmon radiation efficiencies without considering the field. The solid lines represent the plasmon radiation efficiencies considering the effects of the near-field enhancement due to the plasmonic resonance of NDs. The yellow dotted line represents the radiation efficiency of a single graphene plasmon launched on a planar graphene surface. All calculations were performed at the wavelength of  $6 \mu\text{m}$ , and the graphene Fermi level was assumed to be  $0.34 \text{ eV}$ .

#### 4.6 Concluding Remark

The gate dependence of the observed radiation under pulsed laser excitation rules out Planckian light emission mechanisms, and is distinctly different from that observed under CW laser excitation. The major contribution of the emission observed under CW laser excitation is from thermal emission, as its gate dependence is consistent and occurs in the same spectral region as that seen in thermal emission. The gate dependence shown in emission under pulsed laser excitation is not only opposite, but also occurs in a different spectral range ( $>8 \mu\text{m}$  for CW and thermal emission;  $<8 \mu\text{m}$  for pulsed). The observation of such behavior relies on the fact that enough carriers have been excited with a 100-fs laser pulse to achieve inversion. For plasmon emission being an inter-band process, having control over graphene Fermi level via electrostatic gating can greatly enhance observation of plasmon-coupled radiation, as hole-doping of graphene enlarges phase space for plasmon emission and also raises the (Pauli-blocking) barrier for plasmon absorption.

## References

- [1] M Zahirul Alam, Israel De Leon, and Robert W Boyd. "Large optical nonlinearity of indium tin oxide in its epsilon-near-zero region". In: *Science* 352.6287 (2016), pp. 795–797.
- [2] Victor W. Brar et al. "Electronic modulation of infrared radiation in graphene plasmonic resonators". In: *Nat. Commun.* 6.1 (Dec. 2015), p. 7032. DOI: 10.1038/ncomms8032.
- [3] L A Falkovsky. "Optical properties of graphene". In: *J. Phys. Conf. Ser.* 129.3 (Oct. 2008), p. 012004. DOI: 10.1088/1742-6596/129/1/012004.
- [4] Zheyu Fang et al. "Plasmon-induced doping of graphene". In: *ACS nano* 6.11 (2012), pp. 10222–10228.
- [5] Peijun Guo et al. "Ultrafast switching of tunable infrared plasmons in indium tin oxide nanorod arrays with large absolute amplitude". In: *Nature Photonics* 10.4 (2016), p. 267.
- [6] Yao-Wei Huang et al. "Gate-tunable conducting oxide metasurfaces". In: *Nano letters* 16.9 (2016), pp. 5319–5325.
- [7] Min Seok Jang et al. "Tunable large resonant absorption in a midinfrared graphene Salisbury screen". In: *Phys. Rev. B - Condens. Matter Mater. Phys.* 90.16 (Oct. 2014), p. 165409. DOI: 10.1103/PhysRevB.90.165409.
- [8] Pierre L Levesque et al. "Probing charge transfer at surfaces using graphene transistors". In: *Nano letters* 11.1 (2010), pp. 132–137.
- [9] Chun Hung Lui et al. "Ultrafast photoluminescence from graphene". In: *Physical review letters* 105.12 (2010), p. 127404.
- [10] A Freddie Page, Joachim M Hamm, and Ortwin Hess. "Polarization and plasmons in hot photoexcited graphene". In: *Physical Review B* 97.4 (2018), p. 045428.
- [11] A Freddie Page et al. "Nonequilibrium plasmons with gain in graphene". In: *Physical Review B* 91.7 (2015), p. 075404.
- [12] Herbert R Philipp. "Optical properties of silicon nitride". In: *Journal of the Electrochemical Society* 120.2 (1973), pp. 295–300.
- [13] K Pi et al. "Electronic doping and scattering by transition metals on graphene". In: *Physical Review B* 80.7 (2009), p. 075406.
- [14] Farhan Rana. "Graphene terahertz plasmon oscillators". In: *IEEE Transactions on Nanotechnology* 7.1 (2008), pp. 91–99.

- [15] Sunmin Ryu et al. "Atmospheric oxygen binding and hole doping in deformed graphene on a SiO<sub>2</sub> substrate". In: *Nano letters* 10.12 (2010), pp. 4944–4951.
- [16] Seung Min Song et al. "Determination of work function of graphene under a metal electrode and its role in contact resistance". In: *Nano letters* 12.8 (2012), pp. 3887–3892.
- [17] Haomin Wang et al. "Hysteresis of electronic transport in graphene transistors". In: *ACS nano* 4.12 (2010), pp. 7221–7228.
- [18] Hua Xu et al. "Investigating the mechanism of hysteresis effect in graphene electrical field device fabricated on SiO<sub>2</sub> substrates using Raman spectroscopy". In: *small* 8.18 (2012), pp. 2833–2840.
- [19] Bob Y Zheng et al. "Distinguishing between plasmon-induced and photoexcited carriers in a device geometry". In: *Nature communications* 6 (2015), p. 7797.

*Chapter 5*

## CONCLUSION

In this thesis, the studied phenomena benefit from the large wave confinement and tunability of graphene plasmons. I have demonstrated that graphene plasmons allow tunable interactions with their local environment, such as thermally induced various motions of quasiparticles. Such interactions enable dynamic control of thermal radiation, and open up new design avenues to novel infrared sources. Furthermore, I have experimentally shown that quasi-equilibrium 'hot' carrier distributions in graphene upon ultrafast optical excitation support bright mid-infrared plasmonic excitation. This study reveals an unconventional way of generating ultrafast and ultrabright mid-infrared light. The ability of graphene plasmons to strongly interact with light makes graphene a great platform for novel mid-infrared light sources. In this chapter, I extend this present work and propose some future directions.

**5.1 Super-Planckian radiation**

The Purcell factor associated with graphene nanoresonators is found to be  $10^6$ - $10^7$  [3]. Thermal emission is a form of spontaneous emission, and thus the rate of thermal emission via graphene nanoresonators can be enhanced by a factor of  $10^6$  to  $10^7$ . In Chapter 2, the modulation speed of thermal emission on the order of kHz from the original Salisbury screen device was demonstrated by electronically switching on and off the plasmonic modes of

graphene nanoresonators [2]. The modulation speed can further be improved by engineering the device structure to reduce the RC constant of the device. Even faster excitations of plasmons can be achieved on a femtosecond time scale via optical excitation [4, 6]. This suggests that thermal emission can be modulated on ultrafast timescales. A fundamentally interesting question to ask is whether having ultrafast optical control of switching graphene plasmons will enable Super-Planckian radiation.

## 5.2 Bright spontaneous emission sources

The spectral flux of spontaneous emitted plasmons per pulse can be several orders of magnitude higher than that of photons emitted by a blackbody at several representative temperatures of 500 K, 1,000 K, and 2,000 K as shown in Fig. 5.1. In our present work, the observed spectral flux of plasmon emission is limited by the time-integrated measurement method. Our current experimental setup time-integrates plasmon flux emitted per pulse, and each laser pulse arrives at the sample approximately every 12 ns. The collected spectral flux can be greatly enhanced by increasing the repetition of pulses or performing time-resolved measurements. Figure 5.1 reports the cumulative plasmon emission flux (i.e., spectral flux time-integrated up to  $t-t_0 \sim 100$  fs, where  $t_0$  denotes the time at which the system has reached a quasi-equilibrium state). The calculations suggest that the plasmon emission process can provide a platform for achieving ultrabright mid-infrared spontaneous light sources.

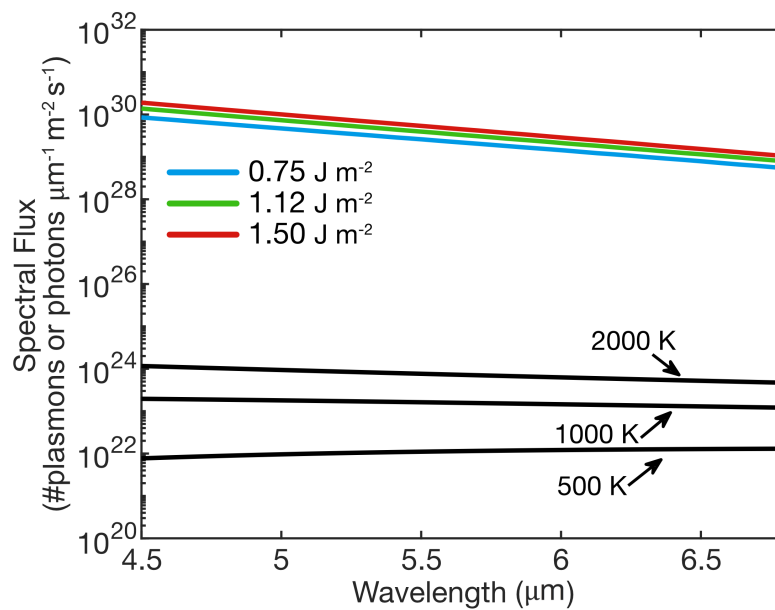


Figure 5.1: Spectral flux of cumulative spontaneous plasmon emission from planar graphene at various laser fluences for a given graphene Fermi level of 0.34 eV compared with the spectral flux of blackbody radiation at 500 K, 1,000 K, and 2,000 K, assuming unity out-coupling efficiency of plasmons.

### 5.3 Coherent graphene plasmon amplification

Our analyses on the ratio of stimulated to spontaneous emission rates (Figure 3.10) showed that conditions of plasmon gain exist on a sub-100fs timescale, and stimulated plasmon emission dominates over spontaneous plasmon in this time interval. This suggests the intriguing future possibility of achieving coherent graphene plasmon amplification on this timescale. Time-resolved pump-probe techniques can directly probe such ultrafast phenomenon. Upon pump excitation, an amplification in the mid-infrared probe beam can serve as evidence for graphene plasmon amplification (Fig. ??). To facilitate coupling of graphene plasmons with the probe pulse, various mid-infrared resonant nanophotonic structures can be explored. Furthermore, by introducing an external plasmonic cavity on graphene, selection of a particular plasmonic mode of interest can be achieved, thus promoting spasing in graphene [1, 5].

## References

- [1] David J. Bergman and Mark I. Stockman. “Surface Plasmon Amplification by Stimulated Emission of Radiation: Quantum Generation of Coherent Surface Plasmons in Nanosystems”. In: *Phys. Rev. Lett.* 90.2 (Jan. 2003), p. 4. DOI: 10.1103/PhysRevLett.90.027402.
- [2] Victor W. Brar et al. “Electronic modulation of infrared radiation in graphene plasmonic resonators”. In: *Nat. Commun.* 6.1 (Dec. 2015), p. 7032. DOI: 10.1038/ncomms8032.
- [3] Min Seok Jang et al. “Tunable large resonant absorption in a midinfrared graphene Salisbury screen”. In: *Phys. Rev. B - Condens. Matter Mater. Phys.* 90.16 (Oct. 2014), p. 165409. DOI: 10.1103/PhysRevB.90.165409.
- [4] G. X. Ni et al. “Ultrafast optical switching of infrared plasmon polaritons in high-mobility graphene”. In: *Nat. Photonics* 10.4 (2016), pp. 244–247. DOI: 10.1038/nphoton.2016.45.
- [5] Mark I. Stockman. “The spaser as a nanoscale quantum generator and ultrafast amplifier”. In: *J. Opt. A Pure Appl. Opt.* 12.2 (Feb. 2010), p. 024004. DOI: 10.1088/2040-8978/12/2/024004.
- [6] Martin Wagner et al. “Ultrafast and nanoscale plasmonic phenomena in exfoliated graphene revealed by infrared pump-probe nanoscopy”. In: *Nano Lett.* 14.2 (2014), pp. 894–900. DOI: 10.1021/nl4042577.